ACKNOWLEDGEMENT

This material is based upon work supported by the Department of Energy under Award Number DE-FE00004566.

DISCLAIMER

Prototyping and Testing a New Volumetric Curvature Tool for Modeling Reservoir Compartments and Leakage Pathways in the Arbuckle Saline Aquifer: Reducing Uncertainty in CO_2 Storage and Permanence

Final Report

Prepared by

Jason Rush

Yevhen (Eugene) Holubnyak

W. Lynn Watney

December 9, 2016

Work Performed Under Contract No. DE-FE0004566

Prepared for

U. S. Department of Energy

Brian Dressel, Project Manager

National Petroleum Technology Office

P. O Box 10940

Pittsburgh, PA 15236

Prepared by

The University of Kansas

Kansas Geological Survey

Lawrence, Kansas

Table of Contents

EXECUTIVE SUMMARY (ABSTRACT)

This DOE-funded project evaluates the utility of seismic volumetric curvature (VC) for predicting stratal and structural architecture diagnostic of paleokarst reservoirs. Of special interest are applications geared toward carbon capture, utilization, and storage (CCUS). VC has been championed for identifying faults (offset <¼ λ) that cannot be imaged by conventional 3-D seismic attributes such as coherence. The objective of this research was to evaluate VC-techniques for reducing uncertainties in reservoir compartmentalization studies and seal risk assessments especially for saline aquifers. A 2000-ft horizontal lateral was purposefully drilled across VC-imaged lineaments—interpreted to record a fractured and a fault-bounded doline—to physically confirm their presence.

The 15-mi² study area is located in southeastern Bemis-Shutts Field, which is situated along the crest of the Central Kansas Uplift (CKU) in Ellis County, Kansas. The uppermost Arbuckle (200+ ft) has extensive paleokarst including collapsed paleocaverns and dolines related to exceedingly prolonged pre-Simpson (Sauk–Tippecanoe) and/or pre-Pennsylvanian subaerial exposure. A lateral borehole was successfully drilled across the full extent (~1100 ft) of a VC-inferred paleokarst doline. Triple combo (GR-neutron/density-resistivity), full-wave sonic, and borehole micro-imager logs were successfully run to TD on drill-pipe. Results from the formation evaluation reveal breccias (e.g., crackle, mosaic, chaotic), fractures, faults, vugs (1-6″), and unaffected host strata consistent with the pre-spud interpretation. Well-rounded pebbles were also observed on the image log. VC-inferred lineaments coincide with 20–80-ft wide intervals of high GR values (100+ API), matrix-rich breccias, and faults. To further demonstrate their utility, VC attributes are integrated into a geocellular modeling workflow: 1) to constrain the structural model; 2) to generate facies probability grids, and; 3) to collocate petrophysical models to separate-vug rock fabrics along solution-enlarged fault and fracture systems.

Simulation-based studies demonstrate a potential alternative field development model for developing CO_2 storage sites that target carbonate reservoirs overprinted by paleokarst. Simulation results for this complex reservoir indicate that individual fault blocks could function as discrete containers for CO_2 storage thereby reducing the risk of plume migration outside the legally defined extent of the permitted storage site. Vertically extensive, anastomosing, solution-enlarged fault/fracture systems — infilled by clay-rich sediments — would operate as non-to-low permeability vertical "curtains" that restrict CO_2 movement beyond the confines of the CO_2 storage site. Such a location could be developed in a checker-board fashion with CO_2 injection operations occurring in one block and surveillance operations occurring in the adjacent block. Such naturally partitioned reservoirs may be ideal candidates for reducing risks associated with CO_2 plume breakthrough.

INTRODUCTION

Volumetric curvature is a promising seismic attribute for characterization studies of complex paleokarst reservoirs. Volumetric curvature is derived from three-dimensional (3-D) seismic reflection data. Seismic attributes provide for both quantitative and qualitative interpretation of common geological features (e.g., faults, porosity, and channels). Seismic volumetric curvature attributes, which are the focus of this study, provide estimates of average reflector shape across sub-volumes nested within the larger 3-D seismic cube (Al-Dossary and Marfurt, 2006). Earlier applications demonstrate the potential of volumetric curvature for illuminating fractures developed in the Devonian Thirty-one Formation, west Texas (Blumentritt et al., 2006) and fractures and sags associated with Ellenburger paleokarst in the Fort Worth Basin, Texas (Sullivan et al., 2006). Al-Dossary and Marfurt (2006) note that volumetric curvature "is in its infancy" and therefore requires calibration to "direct measures of fractures through horizontal image logs." Here, we demonstrate the utility of seismic volumetric curvature (VC) for characterization of karst-modified reservoirs by examining logging results — including "direct measures of fractures through horizontal image logs" — from a 2000-ft horizontal lateral drilled through a VC-imaged fault-bound, collapse structure in Arbuckle Group strata. Such technology

Karst-modified, Arbuckle carbonates comprise the major oil producing reservoir in Kansas with allocated cumulative production reaching 2,350 MMBO in 2014. Bemis-Shutts Field has produced over 260 MMBO since its discovery in 1938. The 12-mi² study area is located in southeastern Bemis-Shutts Field, which is situated within a structural reentrant along the east side of the Central Kansas Uplift (CKU) in Ellis County, Kansas (Figure 1A). Arbuckle carbonates unconformably overlie the Upper Cambrian Reagan sandstones and are unconformably overlain by Middle–Upper Ordovician, Simpson shales and sandstones (Figure

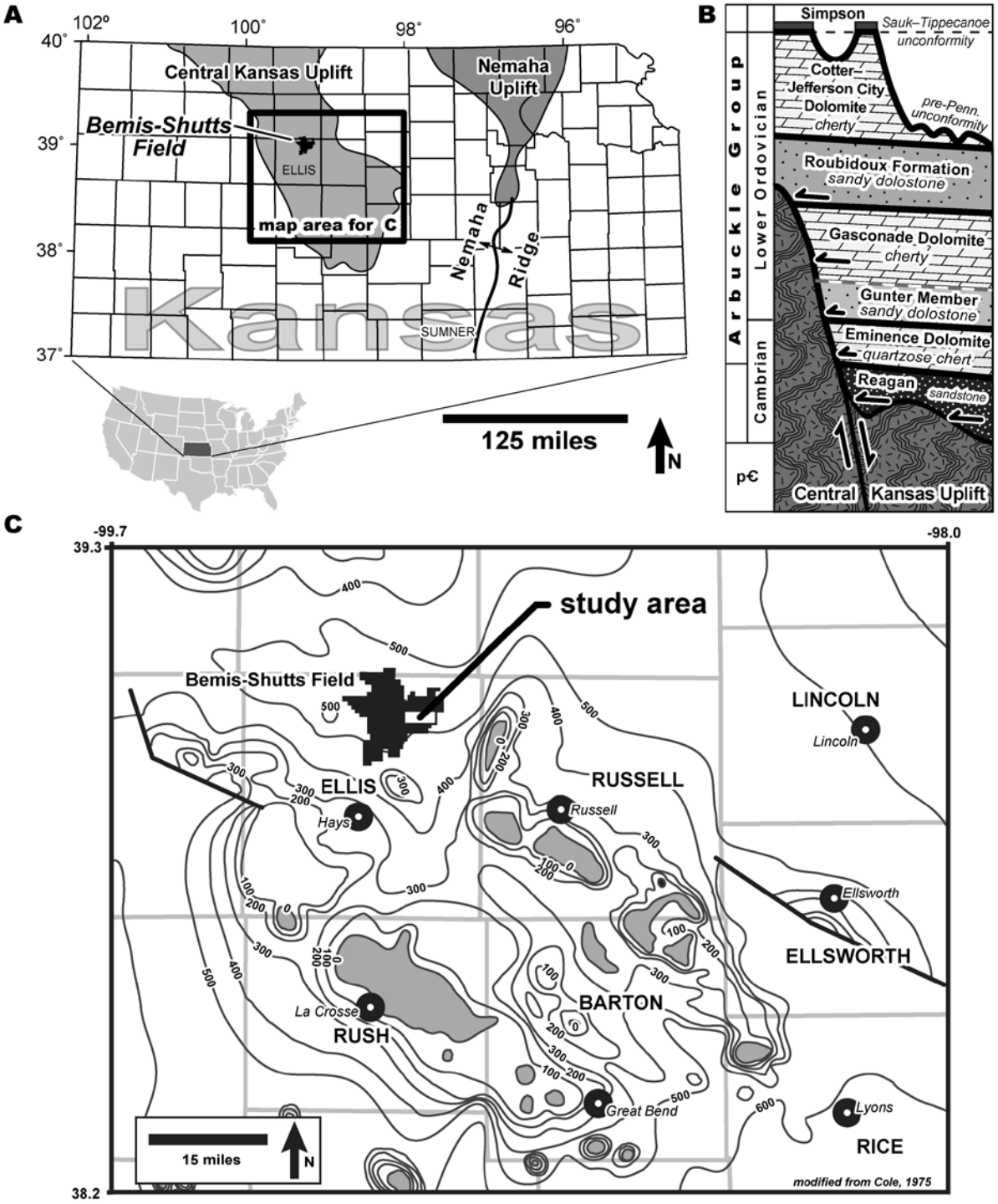

Figure 1. A) Map of Kansas showing major Paleozoic structural features and location of the Bemis-Shutts Field. B) Lower Ordovician stratigraphic framework for the Central Kansas Uplift. Note that the pre-Pennsylvanian unconformity locallly cuts across the Sauk-Tippecanoe unconformity. C) Isopach map of Lower Ordovician illustrating presence of Precambrian basement highs that formed islands during the Early Ordovician transgression. The Roubidoux, Cotter, and Jefferson City formations were likely deposited across most of these positive structures, but were eroded during the Sauk-Tippecanoe and pre-Pennsylvanian lowstands.

1B). Dense well spacing (660-ft offset), seismically resolvable circular depressions, and thick (5+ ft) intervals of polymict breccias within the uppermost (~200 ft) Arbuckle are suggestive of karst modification during pre-Simpson (Sauk–Tippecanoe) subaerial exposure (Walters, 1946, 1991; Cole, 1965) (Figure 1B and C).

Bemis-Shutts Field provides an ideal setting for evaluating seismic volumetric curvature as the presence of bowl-shaped features — indicative of karst — are independently constrained by well control. Project objectives were to drill a lateral borehole across the full extent (~1100 ft) of a VC-inferred paleokarst doline, run wireline logging tools on drill pipe, and then evaluate logs for indications of karst fabrics including large solution-enlarged fractures. Triple combo (spectral GR–neutron/density–resistivity), full-wave sonic, and borehole micro-imager logs were successfully run from TD on drill-pipe. VC-imaged lineaments coincide with 20–80-ft wide intervals of high GR values (100+ API). Image logs reveal breccias, fractures, faults, vugs, well rounded pebbles, and unaffected host strata consistent with the pre-spud interpretation of a local collapse structure and solution-enlarged joints. These data were used to construct complex 3-D structural, facies, and petrophysical models for visualization and simulation-based studies of CO_2 plume behavior, storage capacity, and permanence.

GEOLOGIC BACKGROUND

The Arbuckle Group consists of shallow water facies that were deposited across the broad epeiric carbonate platform that existed across much of North America during the Early Ordovician (Ross, 1976; Fritz et al. 2012). In Kansas, Ordovician rocks occur only in the subsurface. There are more than 50,000 Arbuckle wells in Kansas; however, the stratigraphy is poorly constrained when compared to other producing reservoirs in the state for a number of reasons. Through-going, exploration wells were drilled during the first-half of the 20th-century before the advent of

modern wireline logging tools (e.g., triple combo, borehole micro-imagers) and rotary coring. By the time more-sophisticated wireline logging tools became available, development wells were being drilled by and large only in the uppermost 100 ft of the Arbuckle due to a relatively shallow free-water level. This lack of logs and core from deep-penetrating wells combined with the paucity of biostratigraphic or geochronologic indicators complicates stratigraphic correlation into more-rigorously constrained sections in Missouri and Oklahoma (e.g., Overstreet et al., 2003). The current Lower–Middle Ordovician stratigraphic framework for Kansas is a product of regional correlations using a combination of insoluble residue zonation (Walters, 1946; Keroher and Kirby, 1948; Merriam, 1963; Zeller, 1968) and wireline logs acquired from relatively few basement-penetrating, exploratory wells.

Across Kansas, Arbuckle strata dominantly consist of cyclic shallow subtidal to supratidal carbonates and minor quartz sandstones and evaporites that were deposited across part of a broad epeiric carbonate bank that covered Laurentia during the Early Ordovician (Kay, 1951; Franseen and Byrnes, 2012; Fritz et al., 2012; Warusavitharana and Parcell, 2013) (Figure 2). In Kansas, Arbuckle Group strata are absent across two persistently positive Precambrian structures, the CKU and the Nemaha Uplift (Keroher and Kirby, 1948; Cole, 1962; Chenoweth, 1968). Early stratigraphic studies (Koester, 1935; Walters, 1946) recognized the presence of Precambrian quartzite highlands across the CKU that were not buried until the Middle Ordovician (Figure 3A and B). More than 220 ft of Cambro-Ordovician section onlap the gently dipping (up to 10˚) flanks of flat-topped quartzite monadnocks across the CKU (Walters, 1946). The regional paleoslope during Arbuckle deposition was down toward the southern Oklahoma aulocogen (Figure 2). Arbuckle strata thicken from 0 to 500 ft off the central Kansas and Nemaha uplifts to 1200 ft along the Kansas–Oklahoma border to more than 8000 ft within the

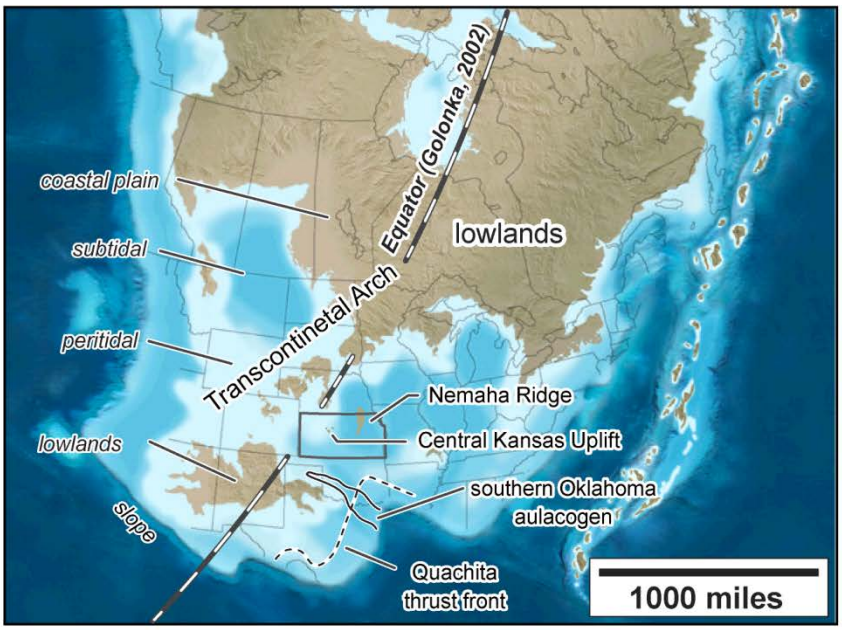

Figure 2. Middle Ordovician (~485Ma) paleogeography map of Laurentia. Sediments deposited across Kansas dominantly consists of shallow subtidal to peritidal sediments. Note that present day Kansas was situated near the equatorial belts, where solar irradiation is most intense and would favor preciptation of evaporites. See text for further discussion. Map modified from Blakely, 2016.

axis of the southern Oklahoma aulocogen (Lindsey and Koskelin, 1991). Peritidal conditions persisted even across the aulocogen where individual cycles record only minor expansion of very shallow subtidal facies (Ham and Wilson, 1967; Fritz et al., 2012). Arbuckle-equivalent slope and basinal sediments are found outboard of the Quachita thrust front (Young, 1970; Thomas, 1977; Fritz et al., 2012), but an intervening open shelf or outer ramp and shelf margin has not yet been recognized (Figure 2).

Karst and collapse breccias within the upper Arbuckle of Kansas have been attributed to Middle Ordovician, pre-Simpson subaerial exposure in eastern Kansas (e.g., Merriam and Adkinson, 1956). This unconformity, which is overlain by Upper Ordovician Simpson strata, coincides with the Sauk–Tippecanoe lowstand (Sloss, 1963; Mussman and Read, 1986; Kerans, 1988; Franseen and Byrnes, 2012). The Middle Ordovician, Sauk–Tippecanoe is associated with paleokarst breccias and has been described from outcrops across North America (e.g., Mussman

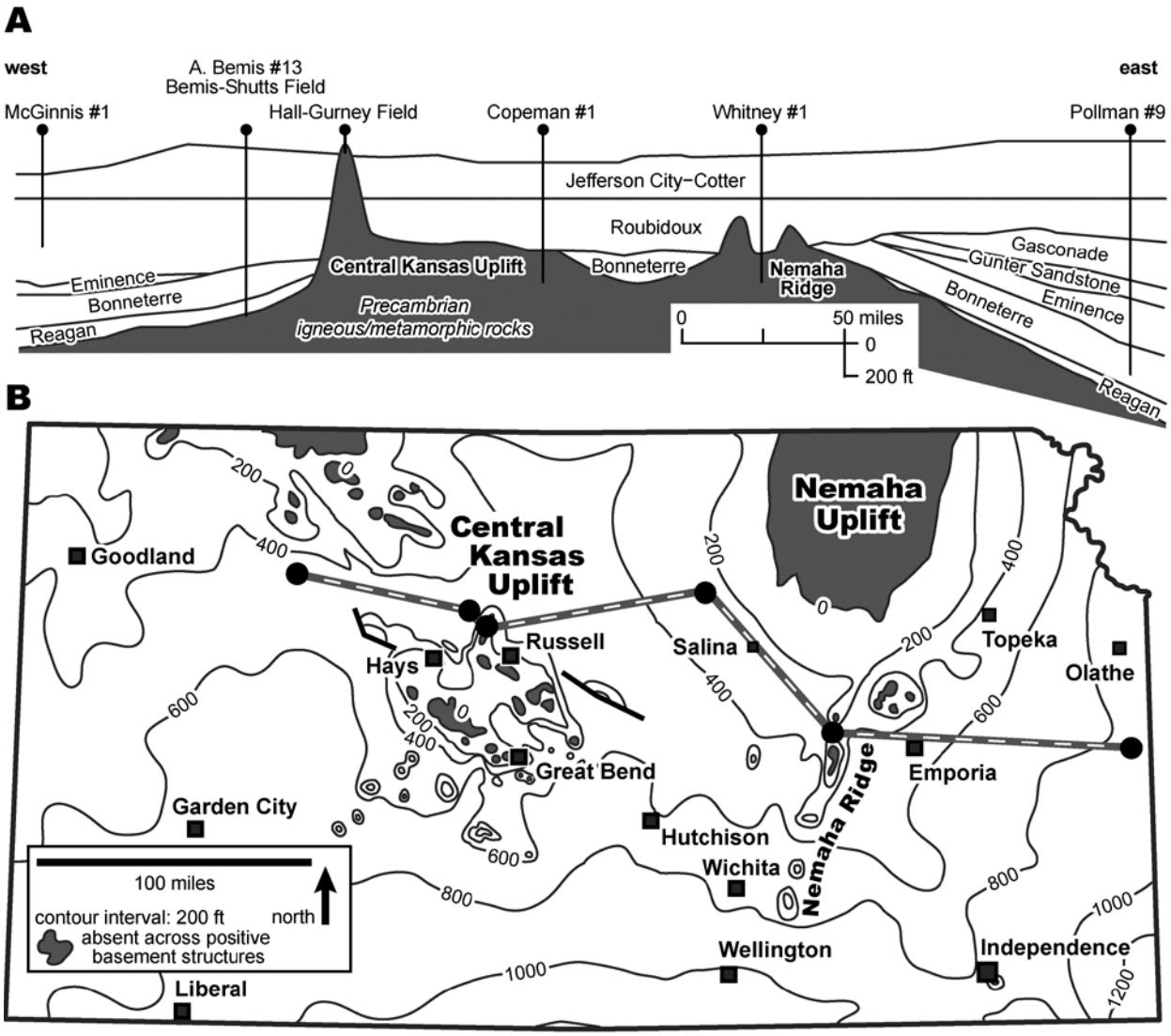

Figure 3. A) Diagramatic west-to-east cross-section across the Central Kansas Uplift and Nemaha Ridge illustrating Lower Ordovician stratigraphic relationships. The Lower Ordovician section is absent at Hall-Gurney Field but thickens toward Bemis-Shutts Field which was located within a structural reentrant. B) Map showing line-of-section for cross-section. Illustrations modified from Keroher and Kirby, 1948.

and Read, 1986; Knight et al., 1991; Lucia, 1995; Dix et al., 1998; Loucks et al., 2004; Cooper and Keller, 2001). Across parts of the CKU, Pennsylvanian strata were deposited across the Arbuckle unconformity or rest directly on the Precambrian (Walters, 1946; Cansler and Carr, 2001). In such cases, the origin of the paleokarst is less certain as it can be attributed to the Sauk–Tippecanoe lowstand, the pre-Pennsylvanian exposure (late Visean–early Muscovian), or a combination of the two.

PALEOKARST BACKGROUND

Some of the earliest subsurface descriptions of Ordovician paleokarst are for Kansas reservoirs (Walthers, 1946; Keroher and Kirby, 1948; Merriam and Atkinson, 1956). Lucia (1969) provides some of the earliest outcrop descriptions of paleokarst collapse breccias from the Lower Ordovician section in the Franklin Mountains near El Paso, Texas. He describes strataform dolomites cross-cut by 1000 ft-thick, 1500-ft wide collapse breccias that occur across several kilometers. Structural sags with more than 200-ft of relief are common across the Lower Ordovician and are associated with upward-penetrating fractures and faults that tip-out in the Upper Ordovician Montoya Group (Lucia, 1995). Kerans (1988) and Lucia (1995) maintain that these caverns are a product of the Sauk-Tippecanoe sea-level lowstand and that subsequent roof collapse and cavern filling occurred about 50 m.y. later after burial under 1000–2000 ft of overburden. Loucks (1999) synthesizes results from earlier publications on modern karst (e.g., Ford, 1988; Palmer, 1991) and paleokarst (e.g., Lucia, 1969, 1995; Loucks and Anderson, 1980; Kerans, 1999; Loucks and Handford, 1992; Lomando, 1993) to generate a process-based, classification systems for cave deposits.

Seismic interpretations of Ellenburger (Lower Ordovician) paleokarst are presented by Hardage et al. (1996) and Zeng et al. (2011). Russel-Houston and Gray (2014) describe paleokarst from the Grosmont Formation using interpretations made from core and 3-D seismic. Hammes (1997) describes fractures, karsted, and brecciated carbonate rocks identified from microresistivity images and core. Our study applies such process-based classification systems (e.g., Kerans, 1999; Loucks, 1999) and builds upon observations made of reservoirs overprinted by paleokarst (e.g., Hardage et al., 1996; Hammes, 1997; Russel-Houston and Gray, 2014) to

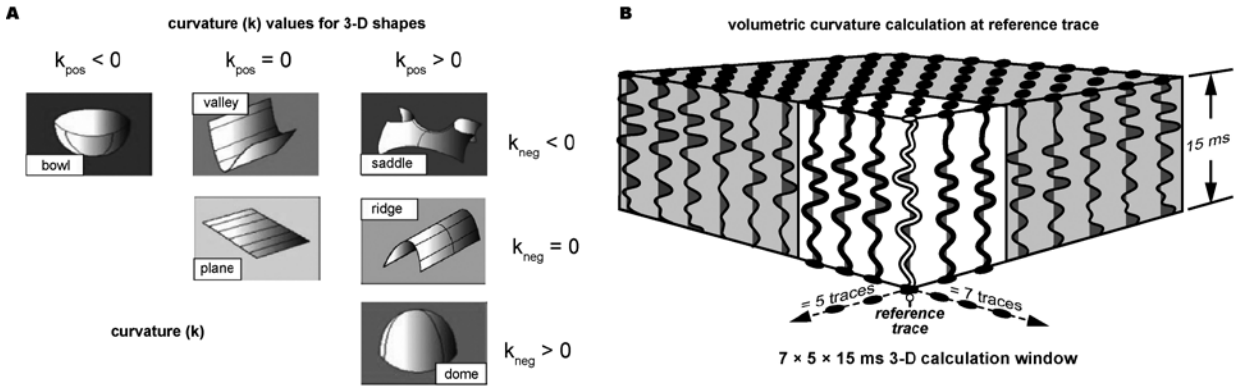

Figure 4. A) Bergbauer et al. (2003) classification of shapes based on curvature values (modified from Al-Dossary and Marfurt, 2006). B) Diagram illustrating how volumetric curvature is calculated relative to an individual seismic trace. See text for further discussion.

constrain interpretations of 3-D seismic, core, wireline logs, and seismic volumetric curvature from Bemis-Shutts Field.

VOLUMETRIC CURVATURE BACKGROUND

Seismic volumetric curvature attributes quantify how reflectors within a seismic volume are bent or flexed in three dimensions (Al-Dossary and Marfurt, 2006). The curvature values for a surface deviate from zero as it is progressively deformed. Positive curvature indicates antiformal features, negative curvature indicates synformal features, and zero curvature indicates planar features (Figure 4A and B). Three-dimensional curvature was originally calculated using structure maps (e.g., Murray, 1968) and later using seismic horizons (e.g., Stewart and Wynn, 2000; Roberts, 2001) to provide information about surface morphology (e.g., saddles, ridges, domes). Volumetric curvature as proposed by Al-Dossary and Marfurt (2006) is not horizon based, but instead estimates reflector curvature across multiple sub-volumes (e.g., 7 by 5 traces by 15 ms) within the 3-D seismic cube relative to a single inline and crossline sample point.

Al-Dossary and Marfurt (2006) demonstrate that calculations of volumetric curvature at various wavelengths (e.g., 11 vs 101 traces) illuminate geologic trends that frequently occur at discrete scales (e.g., meter-scale solution-enlarged fractures vs km-scale paleocavern roof sags). Nissen et al. (2009) notes that volumetric curvature reveals subtle flexures associated with fractures and small-offset (< ¼ wavelength) faults that cannot be detected by conventional 3-D attributes, such as coherence, because their offset is insufficient for generating a break in the seismic reflector. For carbonate reservoirs overprinted by paleokarst, the most-negative curvature attribute has proven valuable for identifying collapse, dolines, and solution-enlarged fractures (Al-Dossary and Marfurt, 2006, Blumentritt et al., 2006; Sullivan et al., 2006). Dolines and sags associated with paleocavern roof collapse are anticipated to appear as high-negative curvature values, whereas the surrounding host strata would have near-zero curvature (Nissen et al., 2009). Karst-modified fissures are frequently filled by clays and siliciclastics (Palmer, 1995) which can generate local velocity pushdowns and negative curvature.

DATA AND METHODS

Approximately 300 vertical wells exist in the study area (Figure 5). Formation tops from early wells (e.g., pre-1960s) are interpreted from drilling breaks and/or analysis of cuttings. Wireline-log interpreted formation picks are from 71 wells. Forty-two wells have porosity logs and of these fifteen have sonic logs. The nearest core is from the Hadley L 4 well, which is approximately 4 miles due west of the McCord A 20H. The top of the Hadley L 4 core (3593-3645 ft MD) is 19 ft below the top of the Arbuckle. The Hadley L 4 core was included in an earlier DOE-sponsored research project evaluating the influence of pore architecture on permeability and initial water saturation. Triple combo (GR-Neu/Den-Res) and sonic logging tools were run from 3673 to 3000 ft MD which coincides with the uppermost 98-ft of the

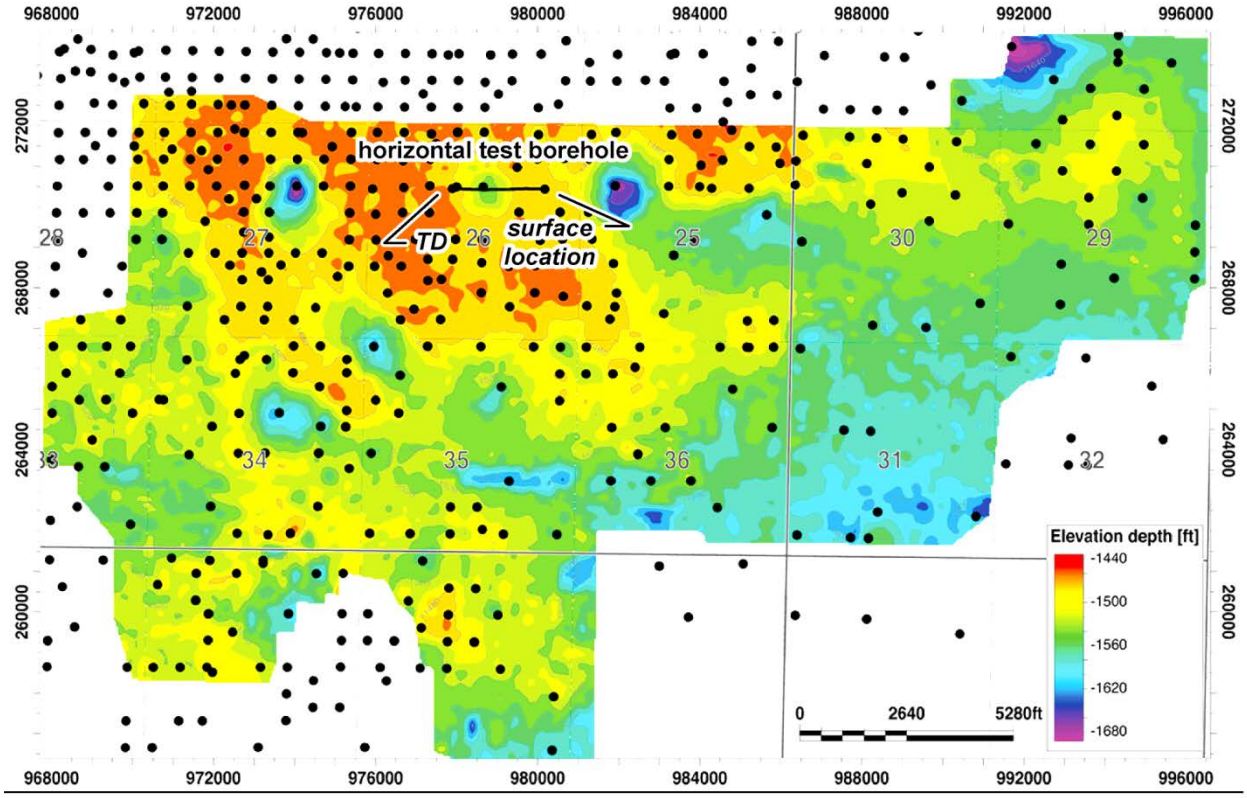

Figure 5. Structure map (PSDM) of the Bemis-Shutts study area. Note circular depressions and irregular well distribution. Most of the wells are concentrated along the top of the structure due to a relatively shallow free-water level (-1580 ft TVDSS).

Arbuckle. Routine core analysis was performed on plugs (56) and whole (21) core. Measurements include porosity, permeability (horizontal and vertical), oil and water saturations, grain density, and Archie (1950) cementation exponents. Porosity values were used to depth-shift the core data. Facies-specific permeability distributions from the Hadley L #4 core were used during petrophysical modeling. Thin sections (27) were made from the plugs of representative lithofacies. Core descriptions from the Hadley L #4 well serve both as a calibration point for interpretation of the microresistivity imaging log and as a constraint on facies-based petrophysical properties. Additionally, a core acquired as part of another DOE project (DE-FE0002056) in Sumner County, Kansas contains a near-complete section (~80%) of

the Arbuckle and was used to describe primary depositional facies that have not been overprinted by large-scale, cross-cutting karst morphologies such as dolines and caverns.

Two seismic surveys that were acquired in 2003 and 2006 from adjacent leases within Bemis-Shutts field were provided to the Kansas Geological Survey in 2011 for seismic reprocessing. A service company merged and reprocessed the seismic data. Their workflow is as follows: application of refraction statics, deconvolution, phase matching, residual statics, prestack Kirchoff depth migration, residual velocity analysis, stacking, spectral whitening, bandpass filtering, and time-depth conversion calibrated to four horizons tied to 100+ wells. The final merged surveys (PSTM and PSDM) encompass approximately 12 sq. miles. Most-negative PSTM and PSDM volumetric curvature attributes were computed by a service company that specializes in attribute generation. Twelve VC attributes were provided for each migrated volume (PSTM & PSDM). Marfurt (2006) provides a detailed description of the different methodologies of principal component-based smoothing whereby estimates of reflector dip and azimuth are calculated at the analysis point. For our purposes, we simply classify principal-component filtering as follows: raw (i.e., no filtering), basic, enhanced, and heavy. Most-negative VC was calculated for each of these principal-component filtered volumes at 50-, 150-, and 500-ft lateral resolutions. The different attribute cubes were loaded into 3-D interpretation and geocellular modeling software and interpreted together with well and seismic data.

To assess the accuracy of VC, a 2000-ft horizontal lateral was drilled through a VC-inferred collapsed paleocavern and drill pipe-conveyed logging tools were run from TD to surface. Because severe hole conditions were anticipated, hostile logging tools equipped with battery memory were conveyed inside drill pipe to TD and then deployed into open hole. Triple combo, sonic tools, and micro-imaging tools were run across the full extent of the collapse

feature (Figure 5). The total porosity of the Arbuckle was estimated using a multi-mineral model of dolomite, quartz, calcite, and shale applied to photoelectric factor, gamma-ray, density and neutron porosity curves (Doveton, 2014). Porosity was then partitioned between interparticle and separate vug by comparing sonic porosity (calibrated to the multi-mineral matrix transit time) to the total volumetric porosity. We also contrasted results from the sonic-derived porosity to an alternative method for partitioning the pore space originally proposed by Watfa and Nurmi (1987). This resistivity-based method uses simple modifications to the Archie equation that incorporates fracture porosity and vug porosity. Core and image log descriptions follow the post-depositional, karst-related facies classification of Loucks (1999) (Figure 6). Measurements of bed, fault, and, fracture orientation were also made using the image logs.

HADLEY L #4 CORE

Core description

The core consists of 1–5-ft thick beds of peritidal sediments and 1–15-ft thick intervals consisting largely of monomict or polymict breccias (Figure 7). A number of rubble zones complicate core depth shifting, but a shift of approximately 10 ft down provides the best match with the wireline logs. Individual clast sizes within breccias are generally less than 5 in. Algal laminites, mudstones with shrinkage cracks, and argillaceous wackestones are the most common depositional facies. Petrographic analysis of thin sections reveals that the primary depositional texture is poorly preserved due to pervasive dolomitization (Figure 8). Dolomite crystal size and their respective intercrystalline pores range from 20 to 250 microns in size. Primary sedimentary structures (e.g., parallel laminations) in siliciclastic sands and clays and carbonate mudstone record soft-sediment folds and flame structures (Figure 7). Small scale (<6 in.) vertical to sub-vertical fractures and rubble zones are present throughout the cored interval. Open fractures

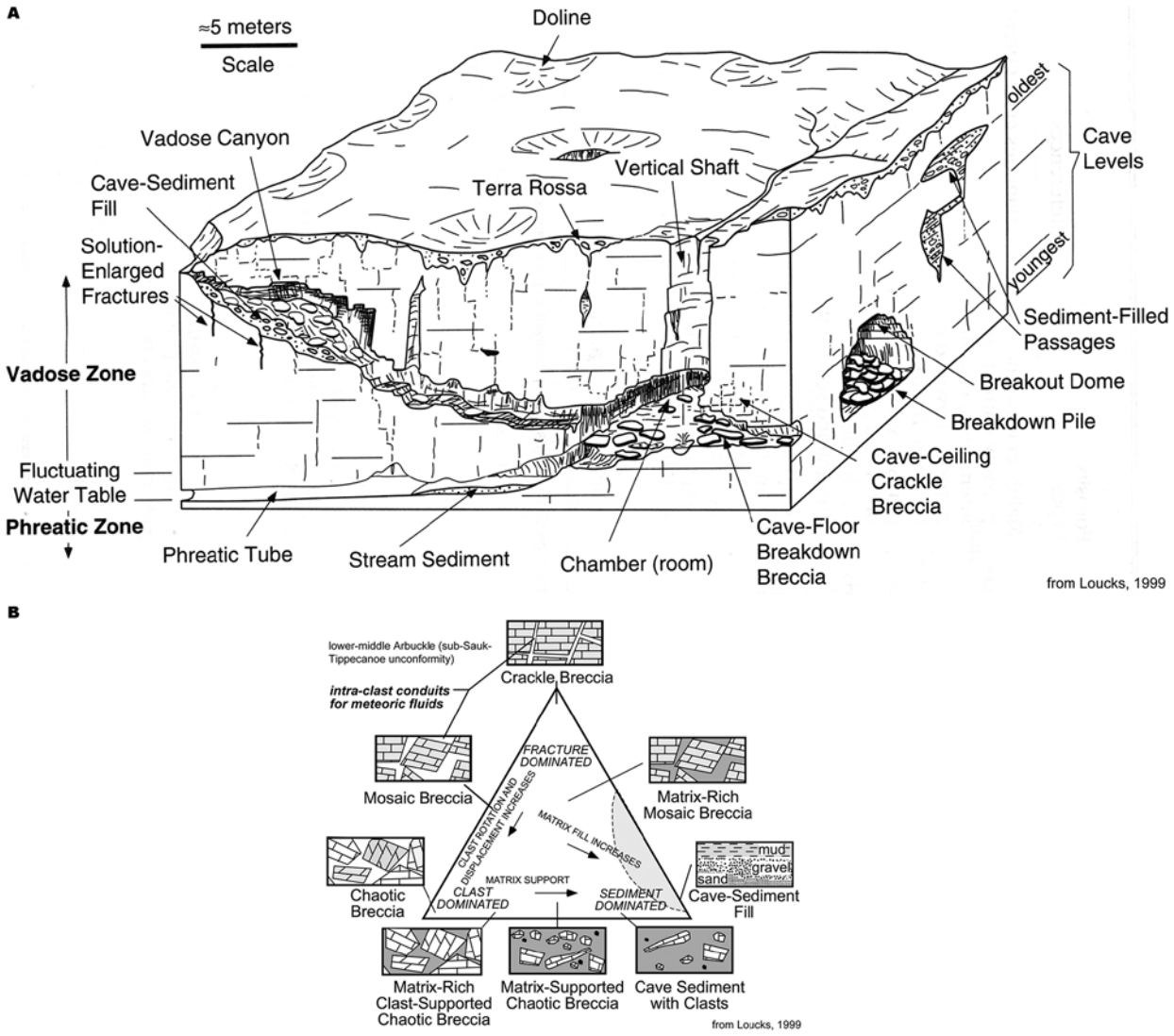

Figure 6. A) Block diagram showing examples of near-surface karst terrain that includes surface, vadose, and phreatic karst features (diagram from Loucks, 1999). This sedimentary process-based model can be used to interpret paleokarst in subsurface data. B) Classification of breccia and clastic deposits found in cave systems that can be used to infer near-surface and burial processes characteristic of paleocaverns (diagram from Loucks, 1999).

(aperture < 0.2 in.) are more common in the lower 20-ft of the core and coincide with polymict breccias and host strata (Figure 7).

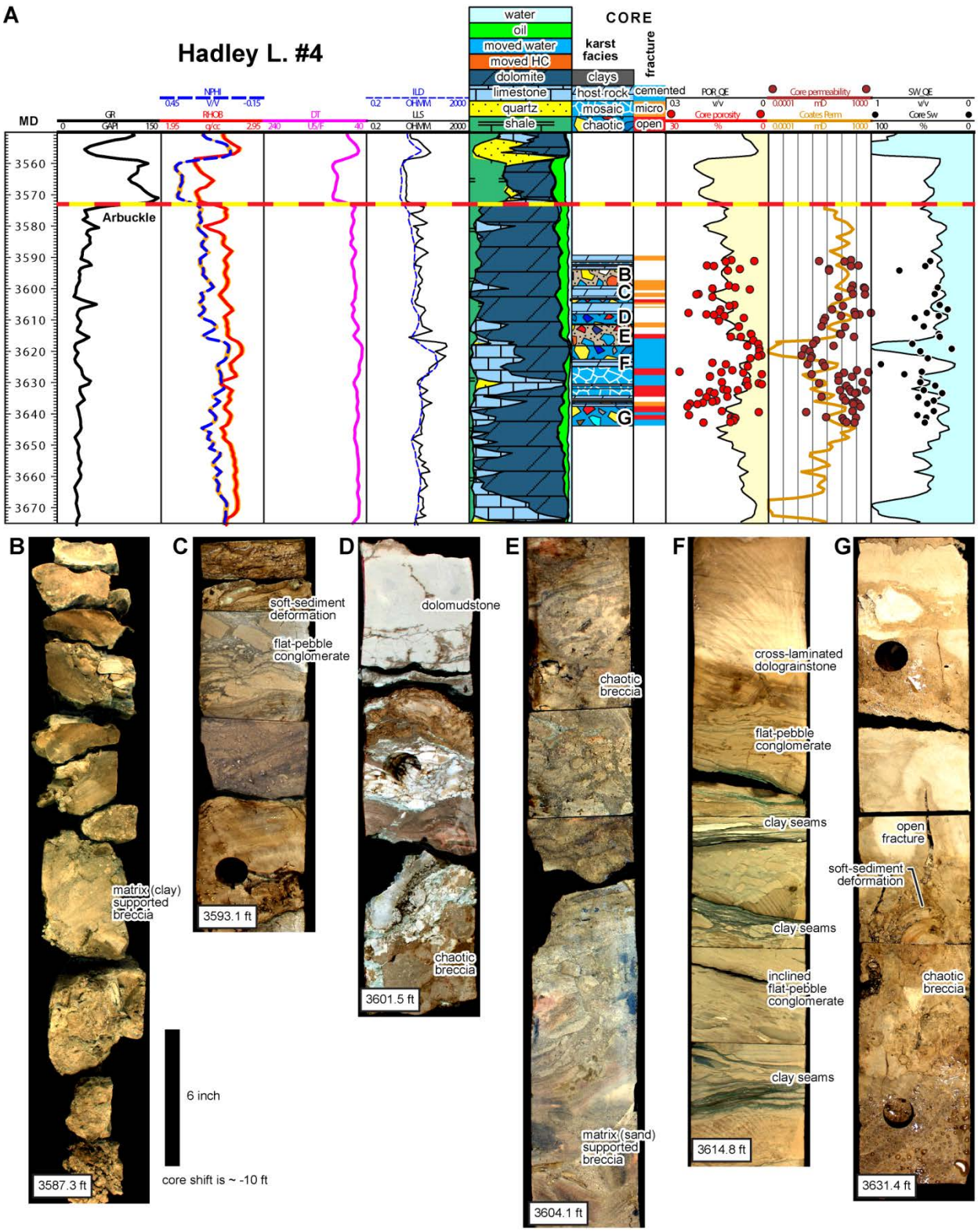

Figure 7. A) Petrophysical evaluation, facies descriptions, and core measurements from the Hadley L #4 well. B-G) Representatitive depositional and karst fabrics observed in the Hadley L #4 core. Note presence of matrix supported breccias, chaotic breccoias, soft sediment deformation, and open fractures. See text for further discussion.

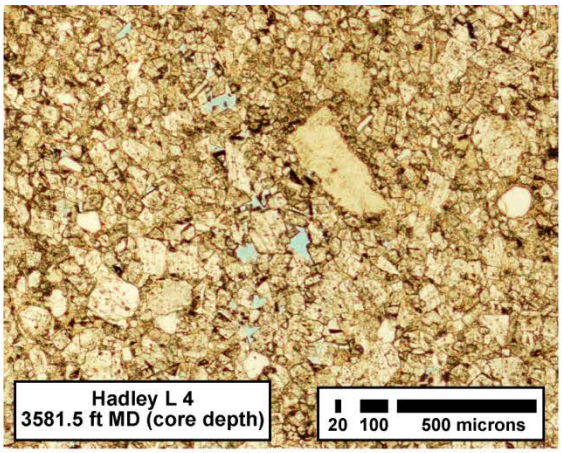

core plug porosity: 12.3% xy permeability: 16.29 mD

Description: Dolostone with local areas of intercrystalline porosity. Microporosity most common.

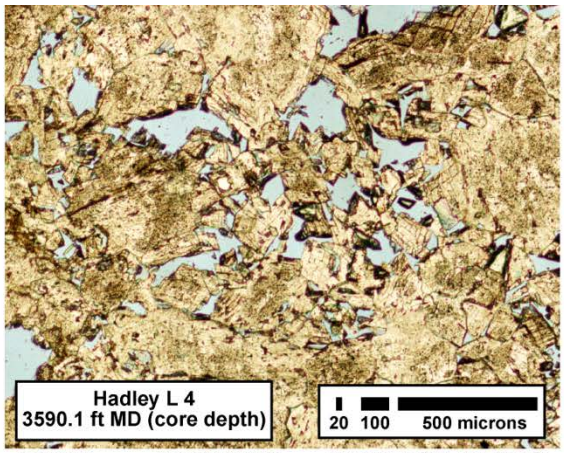

core plug porosity: 16.3% xy permeability: 403.60 mD

Description: Medium to coarse dolostone with excellent (100+ micron pores) intercrystalline porosity.

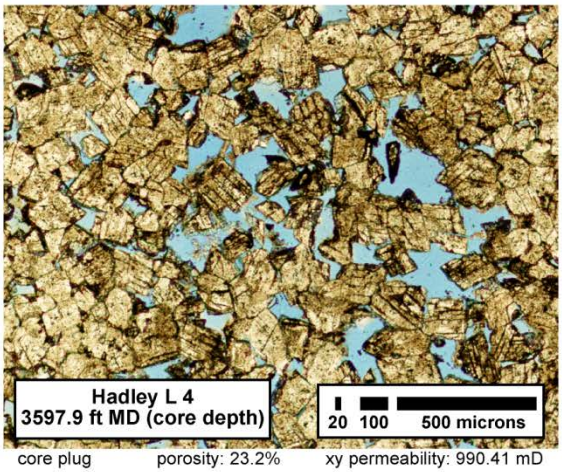

core plug porosity: 23.2% xy permeability: 990.41 mD

Description: Dolostone with excellent intercrystalline pores (100+ microns). Cleavage planes in dolonite crystals are commonly oil stained.

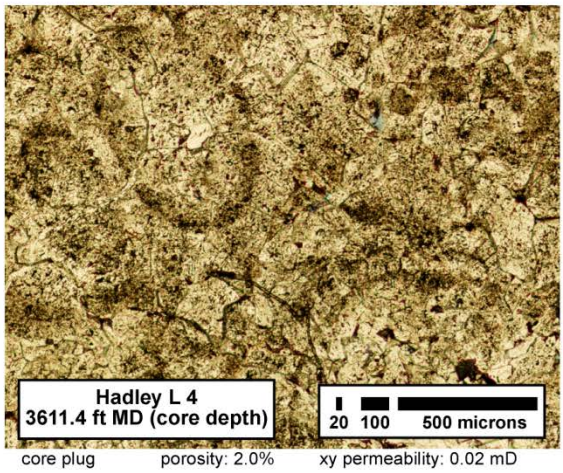

core plug porosity: 2.0% xy permeability: 0.02 mD

Description: pervasively dolomitized grainstone. Some porosity along intercrystalline contacts. Relict grains (coarse ovoid ooids?) are present.

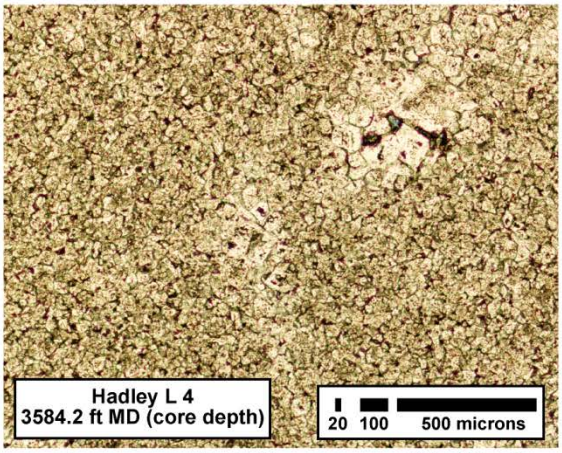

core plug porosity: 11.7% xy permeability: 1.4 mD

Description: fine dolostone with microporosity at intercrystalline contacts.

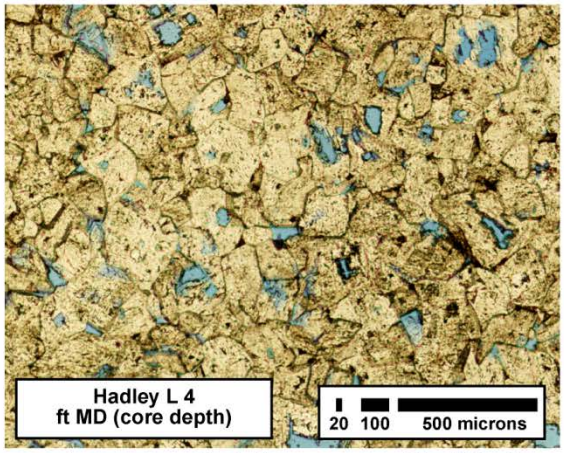

core plug porosity: 4.4% xy permeability: 0.19 mD

Description: 200 micron dolostone with intracrystalline porosity.

Figure 8. Representative dolostones from the Hadley L #4 core.

Core porosity/permeability

Porosity values range from 1 to 26% with greater values measured from core plugs especially within fractured intervals (Figure 7). The samples are not reflective of the primary depositional facies, but instead reflect post-depositional karst-related processes, specifically fracturing, brecciation, and cavernous infilling. Core plug permeability measurements (n = 55) span six-orders of magnitude (.01–4609.81 mD). Differences in permeability as measured from core plugs, whole core, and drill stem tests indicate permeability is largely scale-dependent with core plug samples exhibiting the greatest variability. Core plug and whole core permeability values are consistent with Lucia (1999) classes whereby the intercrystalline pore size primarily controls permeability values (i.e., 100 to 250 microns coincide with highest K values). Whole core permeability (n = 21) ranges from 0.09 to 456.29 mD. Drill stem test estimates of permeability are 382 mD for the interval between 3555 and 3595 ft and average ~10 mD/ft.

Interpretation

The relatively short Hadley L #4 core is best evaluated by comparing rock textures against the nearly continuous Arbuckle core acquired from the KGS 1-32 (Figure 9) well from Wellington Field, Sumner County (Figure 1). This core was acquired as part of DE-FE0002056. These two cores provide critical calibration for interpreting lithofacies from microresistivity image logs acquired from the McCord-A20H horizontal well. The KGS 1-32 core dominantly records shallow marine lithofacies and early soft sediment deformation (Figure 10). Lithofacies indicating shallow marine conditions include algal laminites, thrombolites, hemispheroidal stromatolites, pebbly grainstones, laminated mudstones with mudcracks, fenestral laminites, flat pebble conglomerates, and chaotic mudstone clasts (Figure 10B–G). Meter-scale, soft sediment deformation (Figure 10E–G) and breccias found in association with microbialites are considered

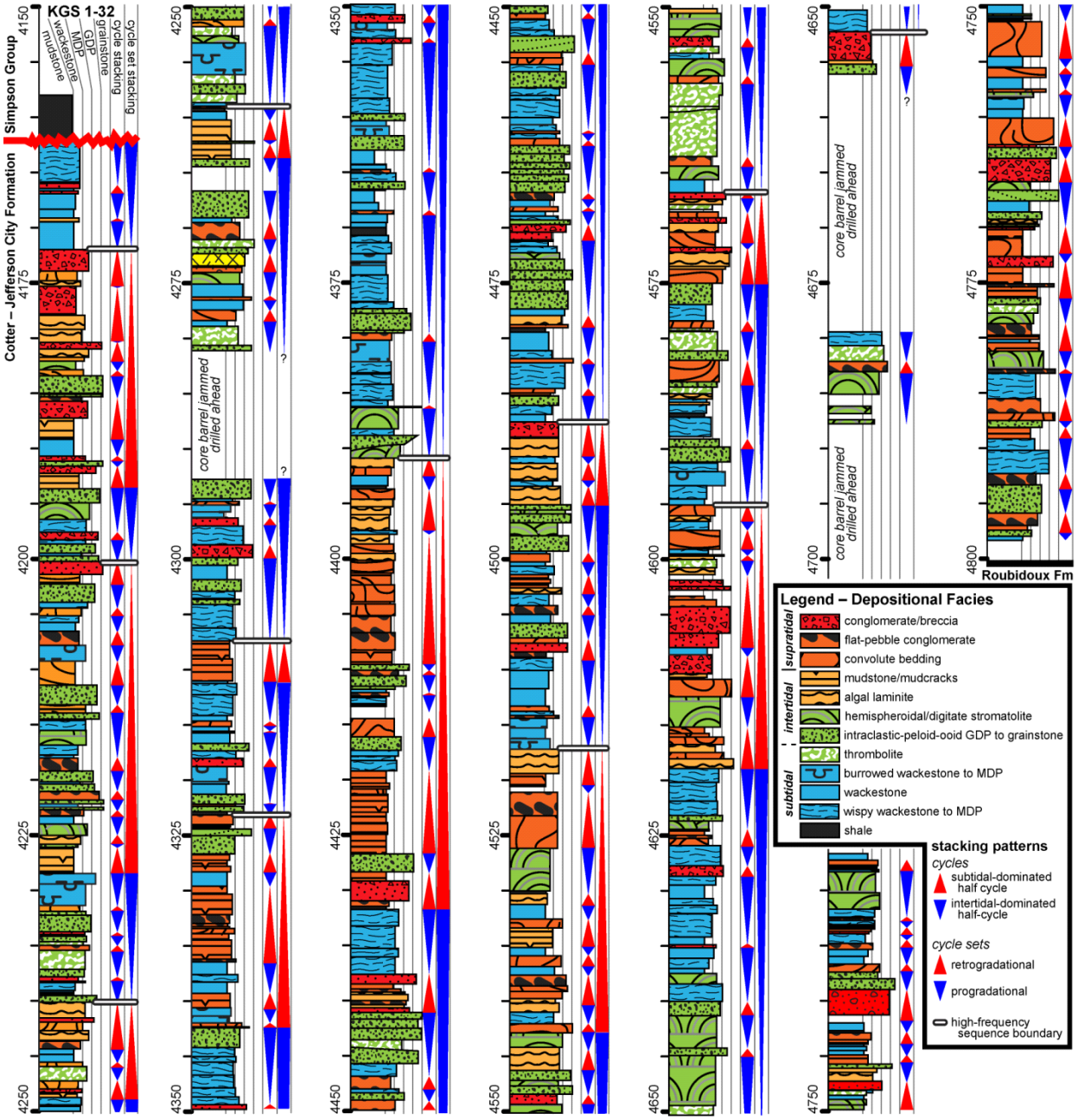

Figure 9. Core description and cycle stacking patterns for the Cotter–Jefferson City Formations from the KGS 1-32 from Wellington Field (Sumner, County, Kansas). Note that lithofacies dominantly reflect shallow normal to restricted marine facies. Similar facies are also common in the Hadley L #4 core, but they have been extensively modified by breccias derived from evaporite and/or near-surface vadose-to-phraetic karst.

"pointers to vanished evaporites" (Westphal et al., 2004; Warren, 2006). Warren (2006) notes that soft sediment deformation is pervasive across evaporite-rich mudflats and that breccias often overlie zones where gypsum has been subjected to burial-induced compaction and dewatering or

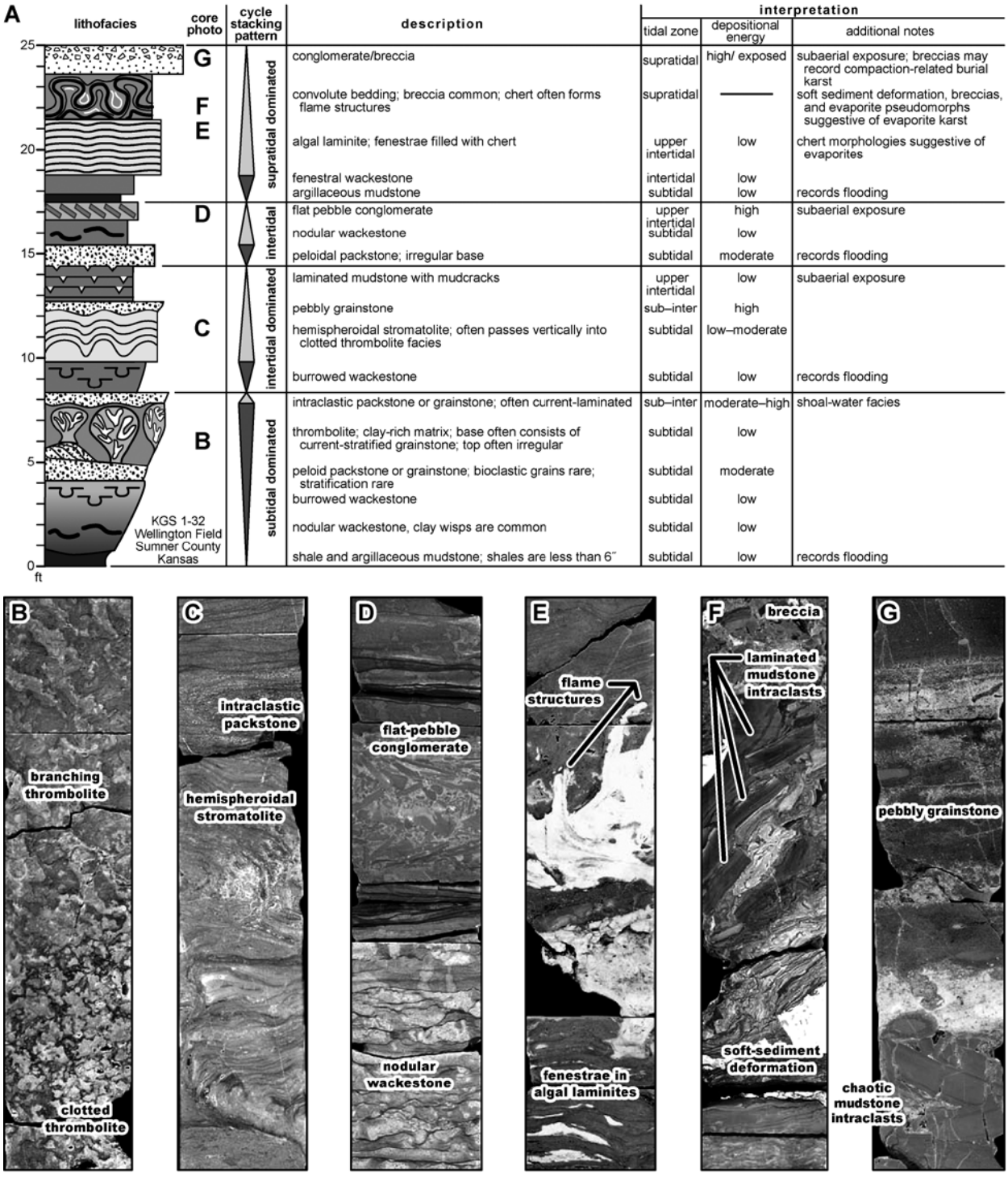

Figure 10. A) Idealized stacking patterns for intertidally dominated cycles from the KGS 1-32 from Wellington Field (Sumner County, Kansas). Cycle bases often consist of argillaceous mudstone to burrowed wackestone that pass vertically into microbialites (B, C, and E) and are capped by intraclastic grainstones (C), flat-pebble conglomerates (D), or mudstones exhibiting dessication cracks. Soft-sediment deformation is commonly present and consists of flame structures (E) and convolute bedding (F). The presence of large fenestrae (E) and convolute bedding likely indicate hypersaline conditions consistent with evaporite deposition.

has been flushed by groundwater. Hypersaline and evaporative conditions were likely operational during the Early Ordovician hothouse climate (Cooper and Sadler, 2012) especially across the interior parts of the bank (e.g., Kansas). The KGS 1-32 and Hadley L #4 record similar lithofacies, but chaotic, polymict breccias are more common in the Hadley L #4, which was situated across the persistently positive central Kansas uplift. Breccias from the Hadley L #4 core are commonly clay-supported and polymictic which likely indicates a vadose cave system that was ultimately filled by siliciclastics sediments sourced from the overlying Simpson Formation and clasts of various lithologies derived from mechanical breakdown of the cave roof (Figure 6).

PSDM VS PSTM SEISMIC

To date, published accounts of volumetric curvature investigations are limited to results derived from PSTM seismic volumes (e.g., Al-Dossary and Marfurt, 2006; Nissen et al., 2009). This project takes the next step and documents results of PSDM-derived volumetric curvature. PSDM volumes provide better imaging of complex subsurface geology (e.g., salt and paleokarst) that are characterized by rapid changes in vertical and lateral velocity that distorts traditional PSTM seismic. Time- and depth-migration solutions are concisely contrasted below by Herron (2000):

> *Depth migration moves reflections to their correct sub-surface positions based on travel times calculated from the migration velocity model. In comparison to time migration, which provides accurate images in areas where velocity is predominantly a function of depth and does not have large lateral variations, a depth migration velocity model contains significant lateral velocity variations—most often as discrete low- or high-velocity bodies embedded in a relatively smooth sediment velocity field. The geometries of these bodies effectively determine the shape of the migration operator, and any error in description (assignment of velocity) or placement of the bodies can result in mis-positioning of reflections in the final migrated image.*

The seismic volume was migrated using proprietary software and techniques. Anisotropic interval velocity models were constructed for the following: base anhydrite, Heebner Shale, and top Arbuckle. The PSDM process utilizes a Kirchhoff-based algorithm and amplitude preservation techniques for AVO-compliant output gathers. The migration performs TTI (tilted transverse isotropy) through the input of VTI (vertical transverse isotropy) models and dip and azimuth files. For a more-detailed description of the depth-migration process, the reader is referred to Appendix I.

VOLUMETRIC CURVATURE

Volumetric curvature attributes were generated for both the PSTM and PSDM volumes. PSDM data is more desirable for reservoir modeling applications as 3-D attributes can easily integrated into 3-D modeling workflows for faults, facies, and petrophysical properties. The input data (i.e., PSDM seismic) was also conditioned using different principal component analysis (PCA) techniques that remove noise while preserving or enhancing signal. Principal component analyses use a small sub-volume of data, which includes multiple traces, in order to separate noise from signal. Such a multi-trace operator may smooth out faults and otherwise alter subtle structure, but Geo-Texture™ software contains algorithms to prevent or minimize over-smoothing. Twelve different VC attributes were generated using PCA conditioning and different lateral windows (Figure 11). Each VC attribute was co-rendered with the PSDM amplitude volume and analyzed for a "best fit" (Figure 12). The volume that underwent basic PCA conditioning using a lateral window of 150-ft was consistent with faults, fractures, and sags observed in the PSDM amplitude volume.

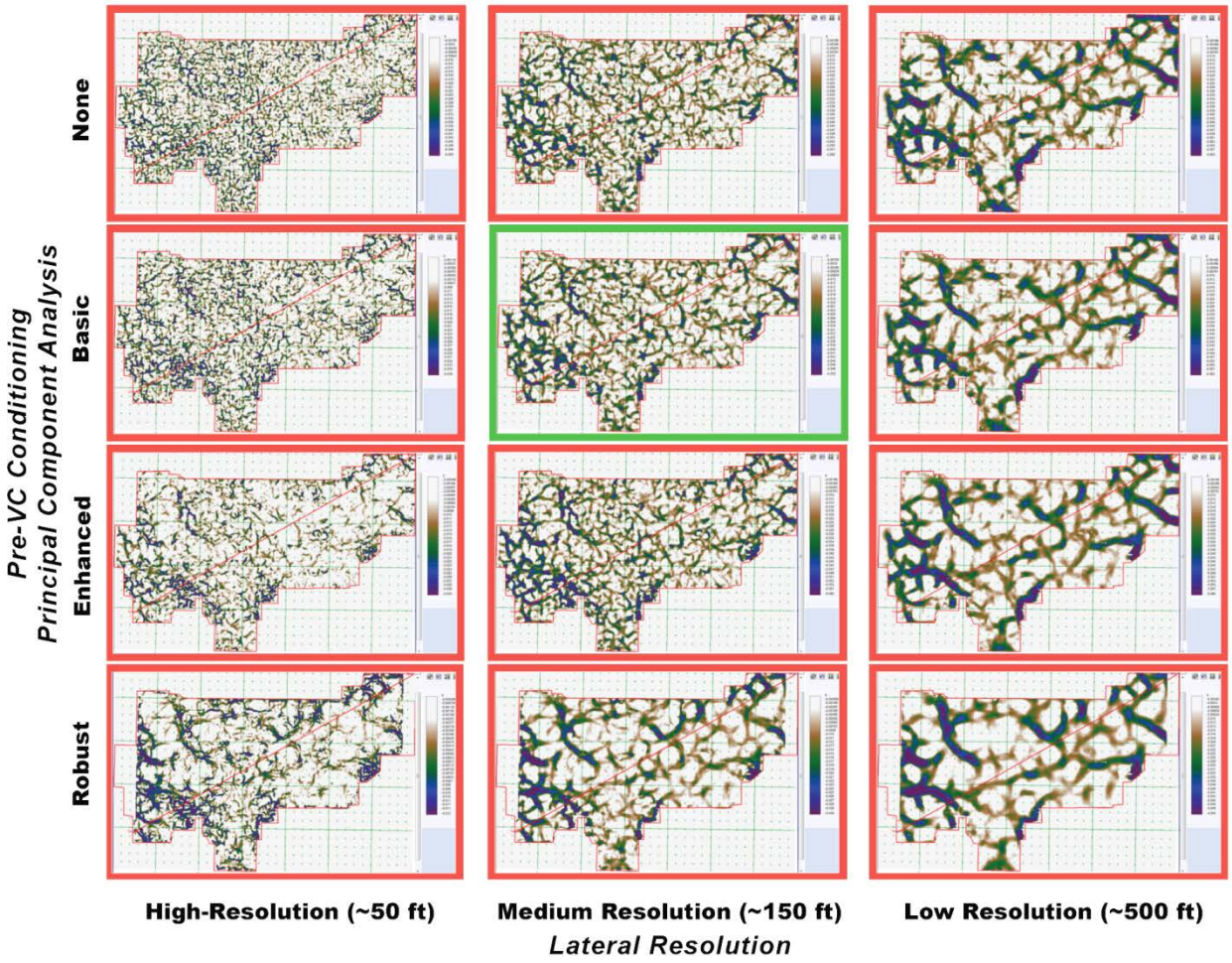

Figure 11. Volumetric curvature attributes (PSDM horizon slice) derived from different PCA conditioning techniques and for different lateral resolutions. Because they are generated using discrete 3-D window sizes, they appear nested, or fractal in appearance. Basic PCA conditioning with a lateral resolution of approximately 150 ft matched best with faults, fractures, and sags observed in the PSDM amplitude volume.

PSDM volumetric curvature

Volumetric curvature measurements attributes can be appear fractal depending on the window sizes selected for VC processing. As such, there are an almost limitless number of volumetric curvature attributes one can assess and the question arises "should each but the most geologically realistic be considered a seismic artifact?" For the purpose of this exercise, we will hold the volumetric curvature attribute constant (i.e., both will have same lateral and vertical dimension).

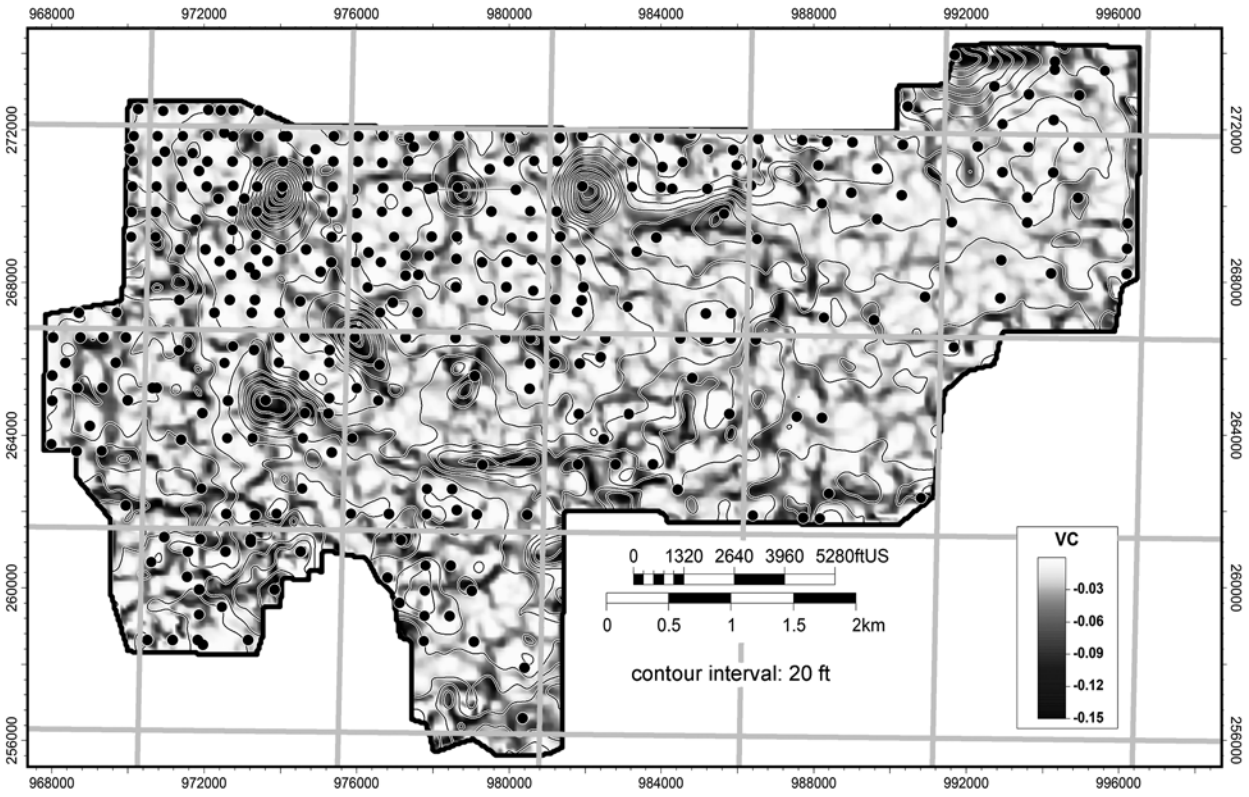

Figure 12. PSDM structure contour map and "best fit" volumetric curvature horizon attribute.

From the discussion above, it should follow that: 1) we need to demonstrate how the iteratively generated, migration velocity model improves focusing and positioning of reflections within the final PSDM seismic volume and 2) how the PSDM-based, volumetric curvature attribute is an improvement over the PSTM-based volumetric curvature attribute. Comparison of PSTM- and PSDM-imaged top Arbuckle (Figure 13) reveals significant differences that arise due to anisotropy. These solutions are based solely on migration and are not constrained by formation tops. Circular features consistent with paleokarst dolines, or collapse, are barely noticeable in the PSTM Arbuckle horizon. This demonstrates improved resolution via depth-migration. In Figure 14, the PSTM and PSDM structure contour maps co-rendered with equivalent volumetric curvature attributes (each are generated using the same lateral and vertical calculation windows).

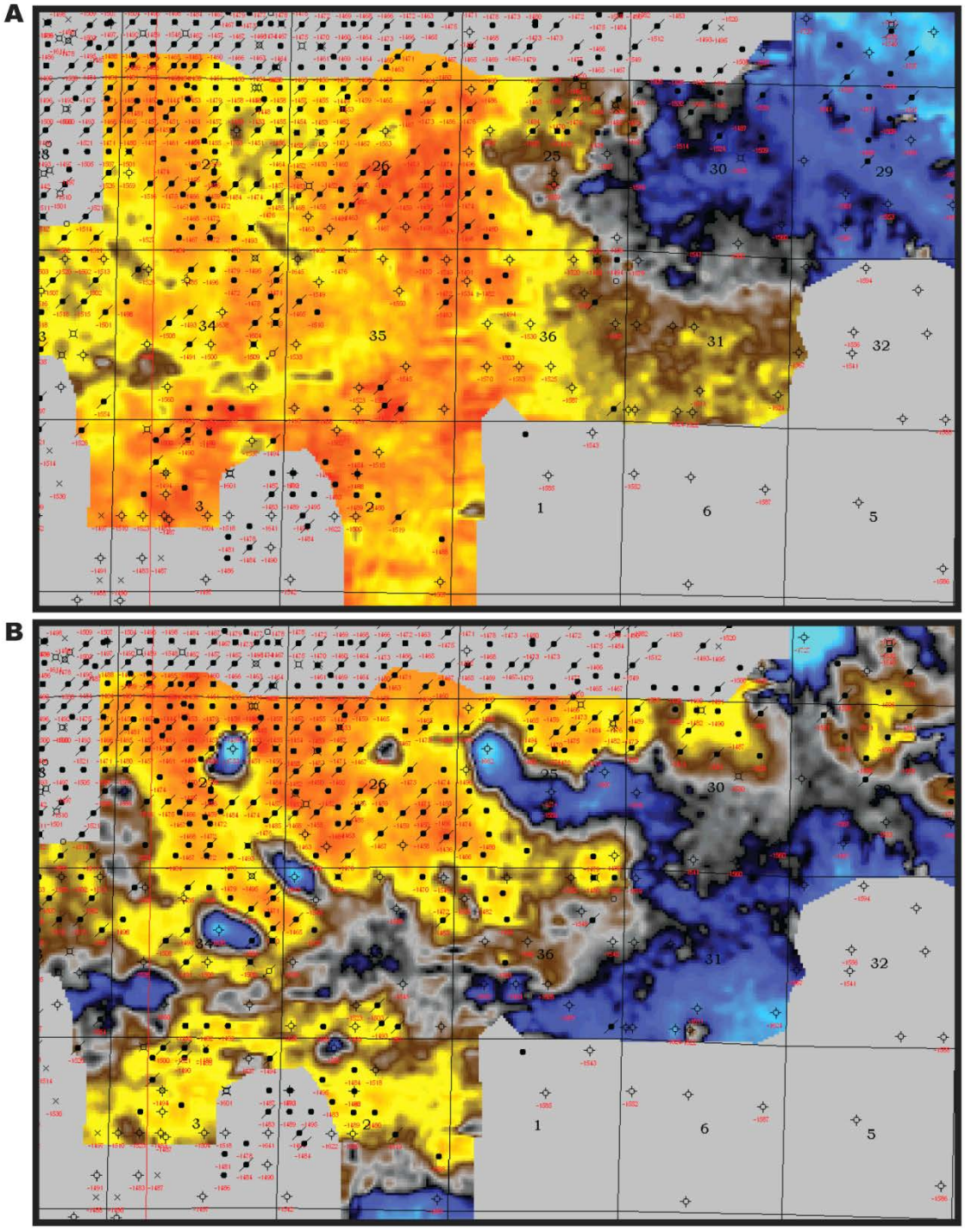

Figure 13. A) PSTM structure map for top Arbuckle. B) PSDM structure map for top Arbuckle. Only general trends are observed on the PTSM map. Circular depressions suggestive of paleokarst dolines are subdued or absent across the PSTM. On the PSTM map, the northwest part of the field which coincides with the crest of the field, is structurally low. In contrast, the PSDM horizon is consistent with well control and conceptual geologic models.

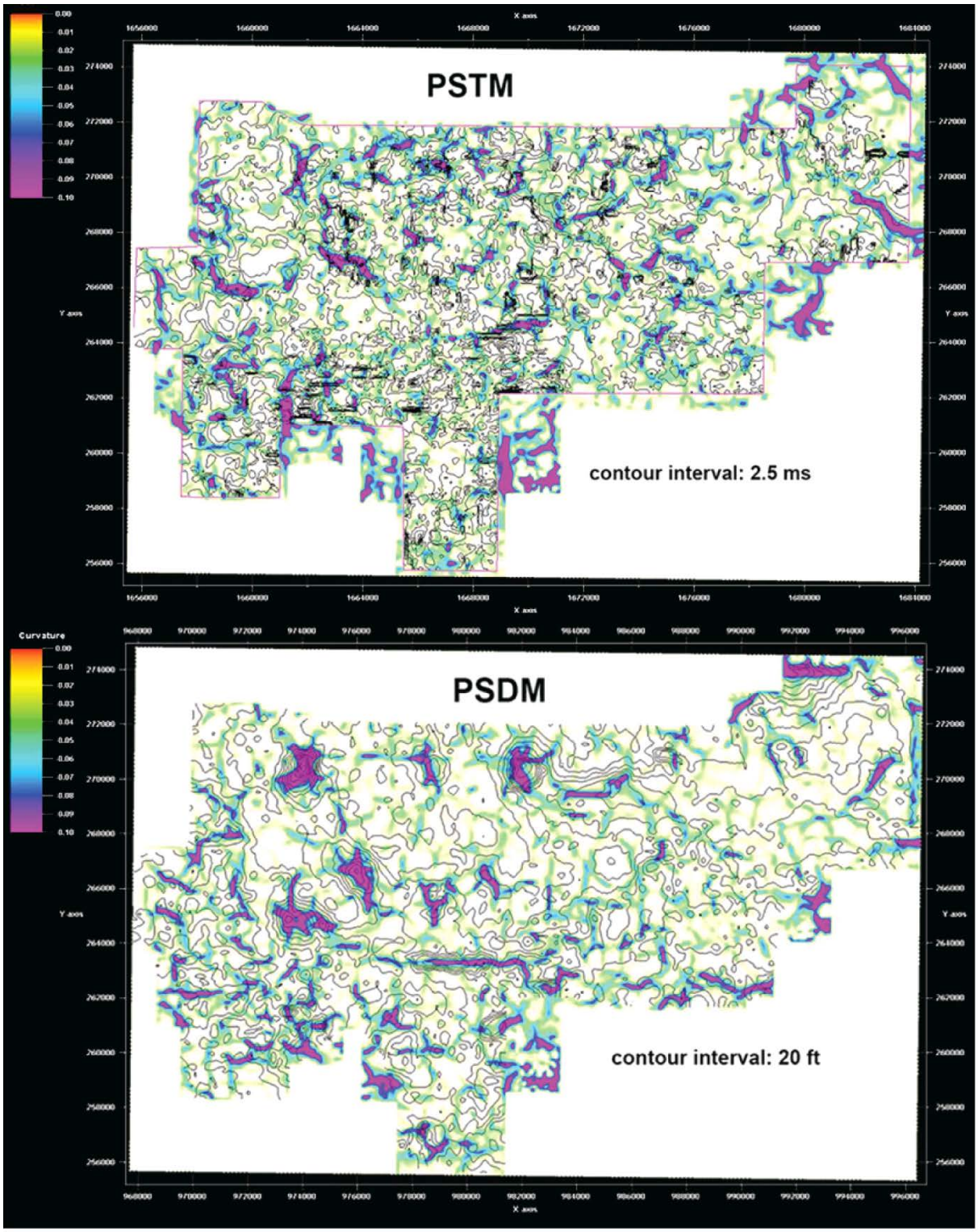

Figure 14. A) Volumetric curvature horizons from middle Arbuckle co-rendered with contours from top Arbuckle. Volumetric curvature was claculated using approximate lateral and vertical dimensions for both PSTm and PSDM volumes. Geometries derived from the PSDM volumes are consistent with the structure contours.

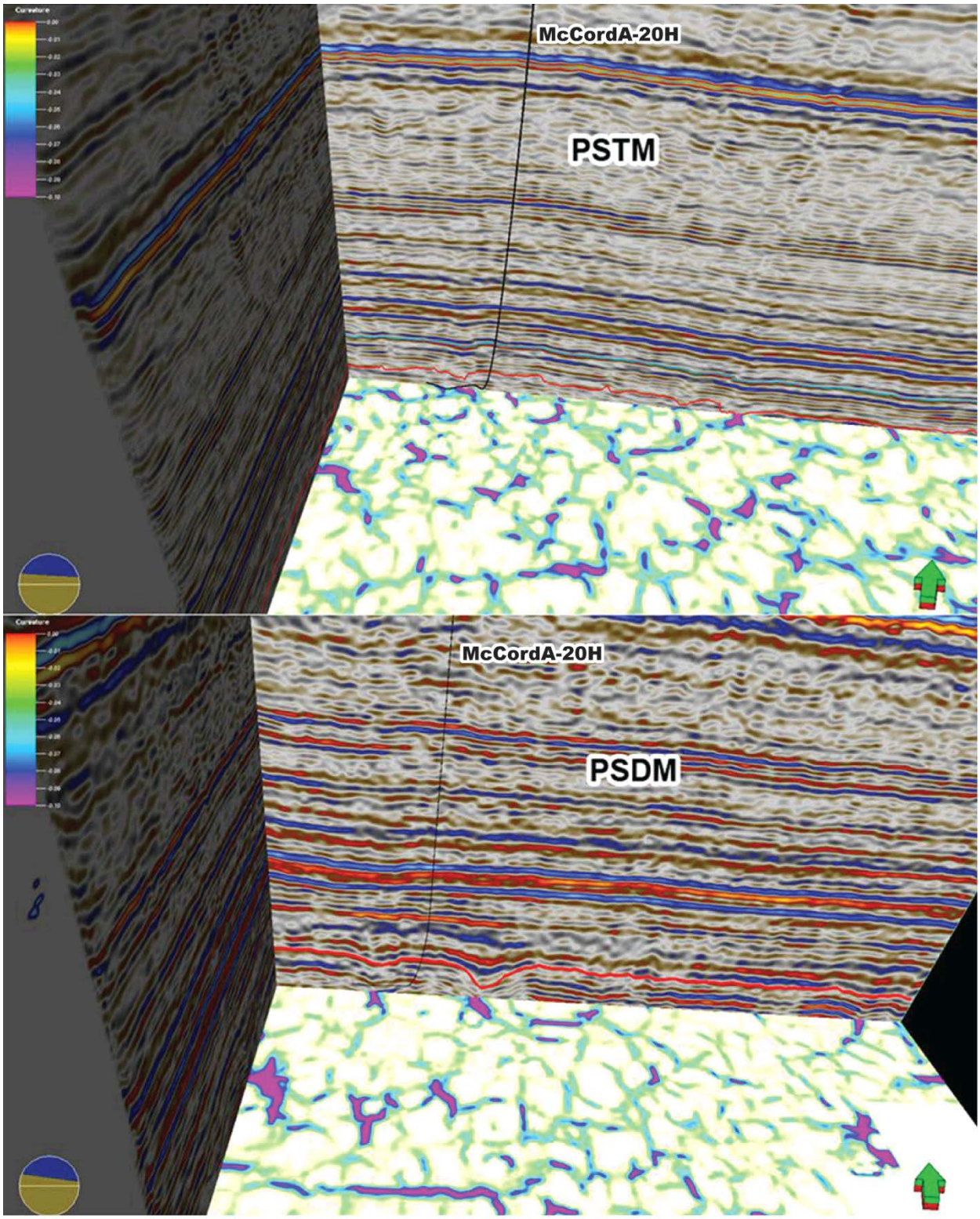

Figure 15. Comparison of co-rendered PSTM and PSDM amplitude inlines and crosslines and volumetric curvature attribute slices. Reflector geometries along top Arbuckle (red polyline) are more pronounced in the PSDM volume. Also shown is the McCord A 20H test boring.

The PSDM volume reveals improved lateral reflector continuity and reflector configurations consistent with paleokarst (Figure 15). Where well control is sufficiently dense (e.g., mature onshore fields), PSDM is a far superior volume for stratigraphic and structural interpretation. The final PSDM volume represents the best case with the velocity model migrating reflectors to their appropriate lateral position and to within ±10-ft of Arbuckle well control. The PSTM volume is important for visualizing how the migration velocity model affects focusing and positioning of reflectors in the final PSDM image. In short, we maintain that artifacts — or the improper positioning of reflectors and/or amplitude anomalies—are more likely to occur in, or be derived from, PSTM volumes.

VC VALIDATION BOREHOLE

Petrophysical analysis

A directional drilling plan and logging program was approved for a horizontal well in section 26 of the study area (Figure 5) that would permit critical evaluation of the seismic VC attribute. The prospective drilling target was a fault-bounded (1100-ft in diameter), paleokarst sag (i.e., doline) inferred from a radiating VC anomaly and the PSDM seismic volume (Figure 16). The paleokarst doline appears coincident with radial fault and fracture systems. These near-vertical faults appear basement-rooted and tip-out in the Chase Group. Strata overlying the Chase Group exhibit geometries consistent with compaction-induced folding above fault tips.

The Arbuckle was encountered just 4 ft (TVD) below the PSDM-mapped horizon. The borehole penetrated 2,190 ft of Arbuckle with a 2100-ft reach. The lateral borehole crossed the full extent of the fault-bounded paleokarst doline with preliminary formation evaluation results showing clearly defined intervals of paleokarst breccias, fractures, faults, and unaffected host

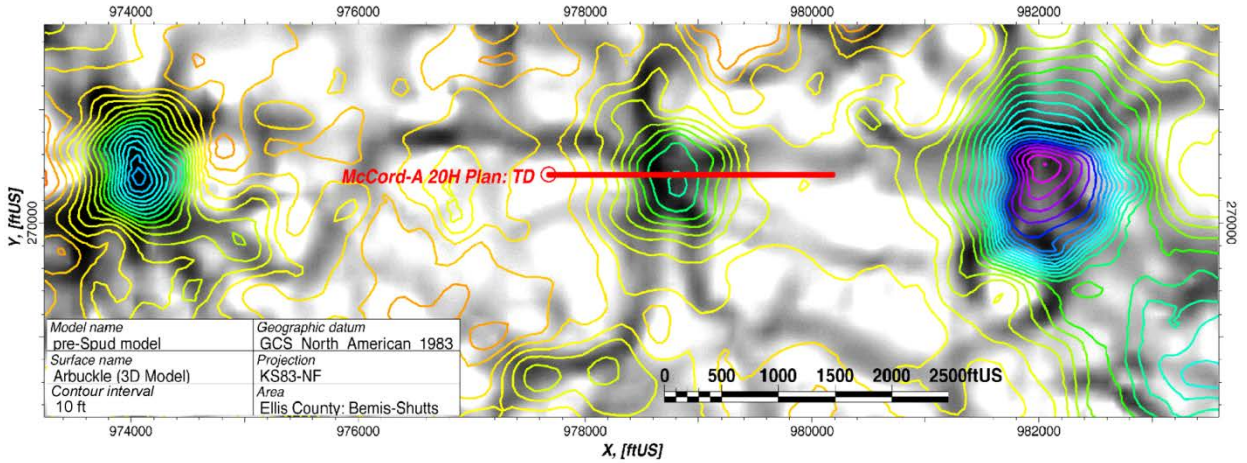

Figure 16. Map showing the proposed horizontal well location in relation to the Arbuckle structure map and "best fit" volumetric cruvature attribute. Negative curvature lineaments radiate in a spoke-like fashion from the center of the depressions. As planned, the wellbore would land 250-ft below the top of the Arbuckle at a near-horizontal (~90˚) inclination and exit the lateral extent of the doline at its western margin. Triple combo, full-waveform sonic, and a microresitivity (imaging) logging tools were run from TD to the 9 5/8″ casing shoe to directly confirm VC-imaged lineaments. See Figure 5 for the location within the study area.

strata consistent with the pre-spud VC interpretation. Logs from the build and horizontal section of the Arbuckle indicate lateral variations in lithology, rock fabrics, pore types, and structural features (Figure 17).

The total porosity of the Arbuckle was estimated using a multi-mineral model of dolomite, quartz, calcite, and shale applied to photoelectric factor, gamma-ray, density and neutron porosity curves. This porosity was then partitioned between "primary" and "secondary" porosity by comparing sonic porosity (calibrated to the multi-mineral matrix transit time) to the total volumetric porosity. Many empirical studies have suggested that the sonic porosity is primarily sensitive to interparticle porosity ("primary") and that the difference with total porosity reflects vugs ("secondary porosity"), although the explanatory physical model is mildly controversial.

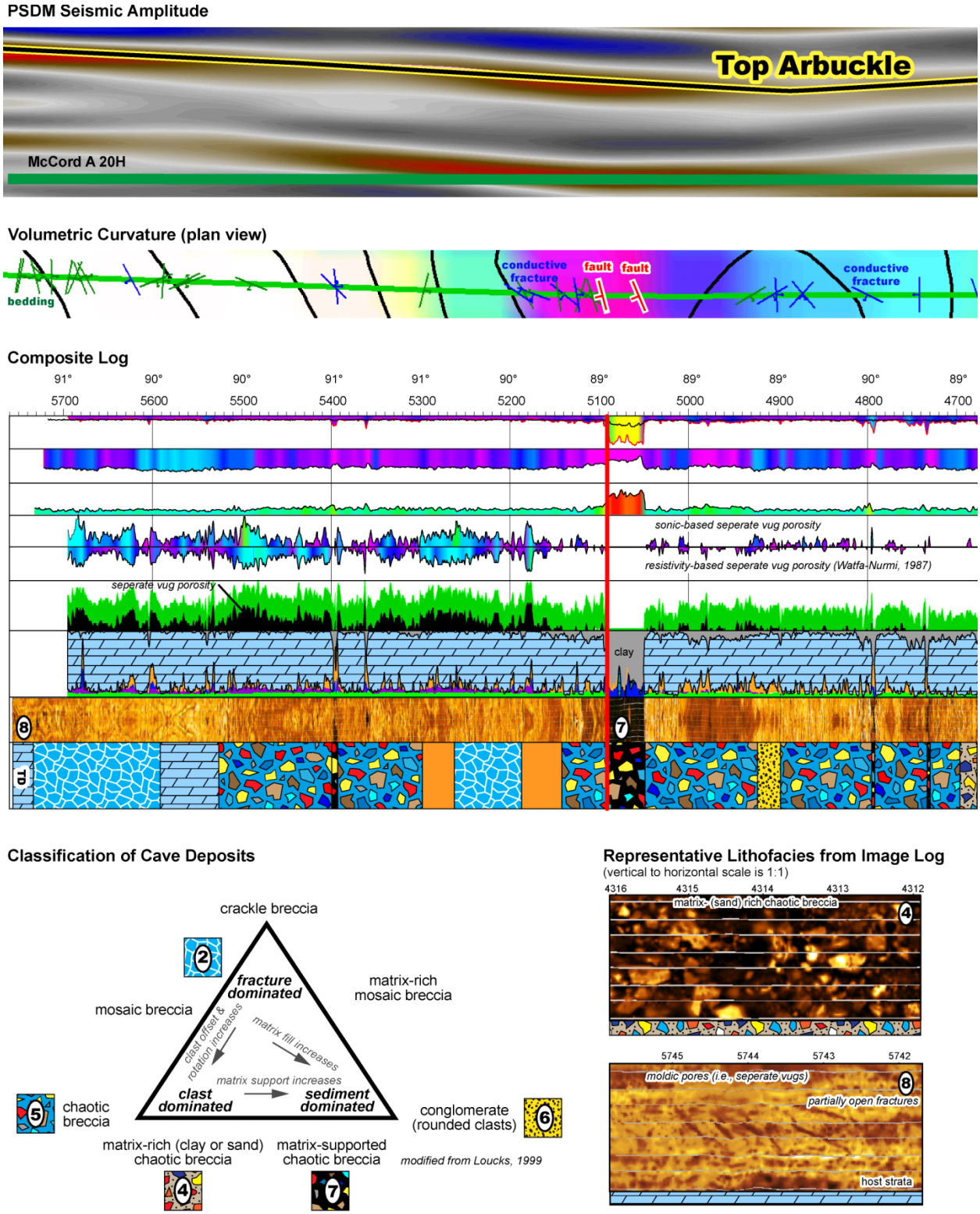

Figure 17. This illustration continues on the next page. Illustration showing seismic data, composite logs, and image log interpretation for the McCord A 20H. Breccias are present along the full extent of the wellbore. These include mosaic, chaotic, matrix-rich, matrix-supported, and sediment dominated breccias. The depression is bound by two faults that appear to be solution-enlarged as they coincide

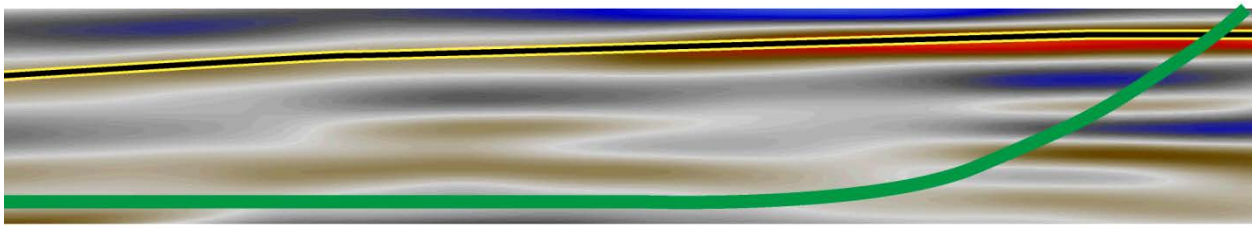

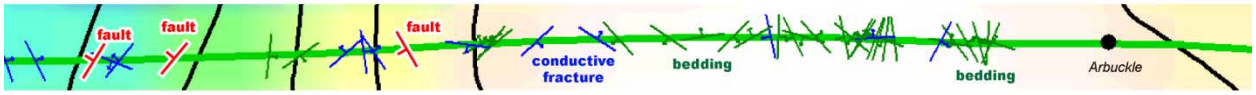

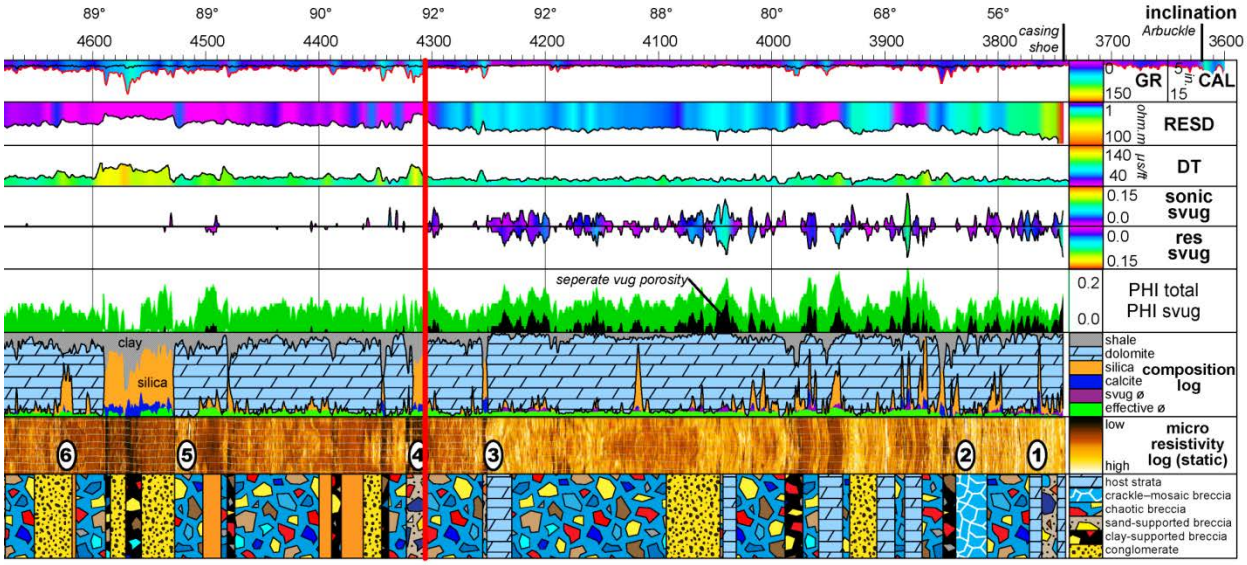

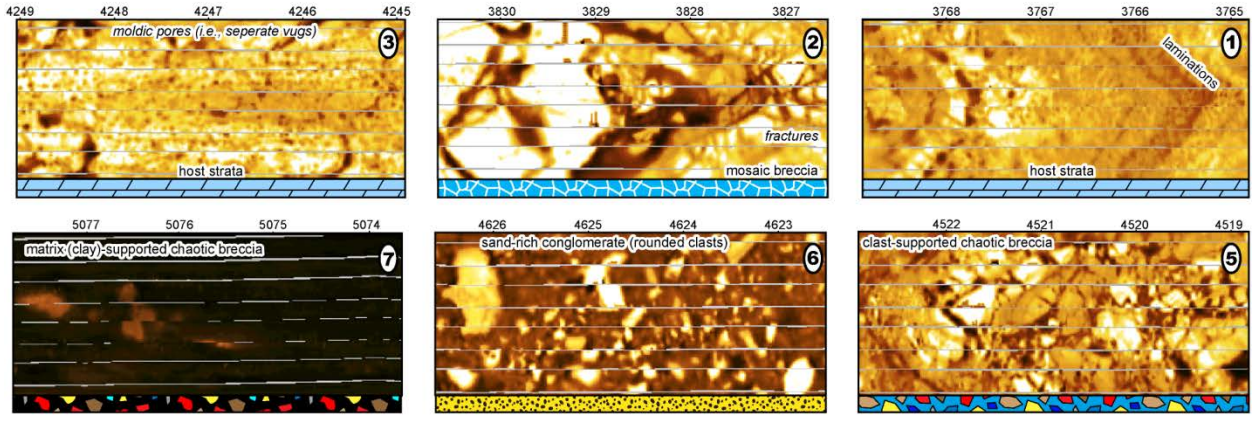

continued from previous page. with laterally extensive intervals (i.e., 4308–4322 ft and 5050–5090 ft MD) of clay and/or sand. A similar feature is also present with the depression from 4525–4600 ft MD). Sonic- and resistivity-based estimates of porosity indicate that separate vug pores are concentrated outside the depression. See text for further discussion.

An alternative method to partition the pore space was proposed by Watfa and Nurmi (1987) using some simple modifications to the Archie equation that incorporate fracture porosity and vug porosity. They reported that application of these equations were matched well by core measurements from a variety of Middle Eastern carbonate reservoirs and were an improvement on the simple Archie equation with cementation exponent, *m* of 2 that is generally applicable for carbonates dominated by interparticle porosity. If planar fractures have an *m* value of unity and the matrix has intergranular and intercrystalline porosity with *m* = 2, then the apparent *m* of a fractured carbonate can be solved by considering the fractures and matrix as resistances in parallel. Then:

$$\Phi^m = \Phi_f + \Phi_{mx}^2$$

where Φ^m is the total porosity made up of Φ_f, the fracture porosity and Φ_{mx}, the "matrix porosity" (intergranular plus intercrystalline porosities). If the vugs are not connected, then electrical current bypasses them and they are non-conductive voids. For this model, the equation is:

$$\Phi^m = (\Phi - \Phi_{nc})^2$$

where Φ_{nc} is the vug porosity. There is insufficient information to solve for both fractures and vugs. However, if the apparent *m* of the carbonate is clearly higher than 2, then unconnected or poorly connected "vugs" (either molds or vugs) are suggested. In this case, the vug equation can be used to solve for vuggy porosity. (This assumes that the elevated *m* values are not caused by hydrocarbon saturations.) If the apparent *m* value is markedly less than 2, then fracture porosity may be suspected.

There is an excellent visual match between the sonic secondary porosity and the non-connected vuggy porosity calculated by the Watfa and Nurmi (1987) equation which is a mutually supportive confirmation that both approaches are sensitive measures of larger pores, even though

they are based on different physical properties. The presence of large (5+ ft wide) clay-filled faults and fractures, vuggy porosity outside the depression, and a greater proportion of shale within the depression (Figure 17) lend support to the interpretation that dolines formed along the top of the Arbuckle and were linked vertically with an underlying system of caverns. In this scenario, faults and fractures would have preferentially formed along the cavern roof creating pathways for clays and sands, derived from the overlying Simpson Group, to infiltrate fractures and vugs within collapsing and compacting caverns (Figure 6).

Image log analysis

Image interpretation consisted of describing 1) structural features and 2) facies. The horizontal borehole crossed the first bounding fault (strike: 330º) at 4,308 ft MD, penetrate ~780 ft of paleokarst breccias, and exit the westernmost, near-vertical, bounding fault (strike: 350º) at 5,090-ft MD (Figure 17). Four types of structural features were identified from the image log. These consist of conductive fractures/faults, partially conductive faults/fractures, faults (having obvious offset), and bedding planes. Sand and clay are present within solution-enlarges faults and fractures. Fractures occur more frequently near and within the VC-identified, fault-bound doline. Breccias were anticipated only in the uppermost Arbuckle and within the paleocavern. However, breccias are present along the entire length of the image log. Bedding indicators are dominantly recorded outside of the paleocavern. The lithology logs indicate a fair amount of siliciclastics and clays in the upper Arbuckle and within the paleocavern. Non-touching vugs are only present outside the paleocavern.

Louck's (1999) paleokarst classification system was used for describing facies (Figure 17). Six lithofacies were described using a combination of the image and lithology logs. These include: 1) dolostone, 2) crackle–mosaic breccia, 3) chaotic breccia, 4) sand-supported breccia,

5) clay-supported breccia, and 6) conglomerate. Sand-supported breccias coincide with high silica measurements. Clay- and sand-supported breccias are most often associated with solution-enlarged faults and fractures. Faults and fractures identified from the image log are tied to their respective fault in the geocellular model.

STATIC GEOLOGIC MODEL

Model zones

Kerans (1988) presents a conceptual model for the age-equivalent and karst-modified Ellenburger of Texas. The Ellenburger and Arbuckle have similar depositional facies (Kerans, 1988; Franseen and Byrnes, 2012; Fritz et al., 2012) and the large-scale (1000 × 100 ft) morphologies described as part of this study are consistent with burial modification of a near-surface karst terrain (Kerans, 1988; Hardage et al., 1996; Loucks, 1999) (Figure 18). To generate layering consistent with paleokarst architecture three zones were generated. The lower and middle zones are generally evenly bedded except where they have been truncated by the uppermost zone. This zonation and layering scheme mimics paleocavern architecture whereby the roof collapses into cavern (Figure 19). The 3-D structural grid contains 3,164,112 cells (x=275; y=98; x=75). The average cell dimension is: x = 50.0 ft, y = 49.9 ft, and z=9.6 ft. All property models are assigned the same 3-D grid geometry.

Fault model

Negative curvature values were used to construct the fault model (Figure 18). Although vertical offset is recognizable in the amplitude volume, some of the “faults” in the fault model are best described as fractures. The fault model was constructed using vertical pillars, which is consistent with the observations from the image log and the PSDM volume where faults and fractures

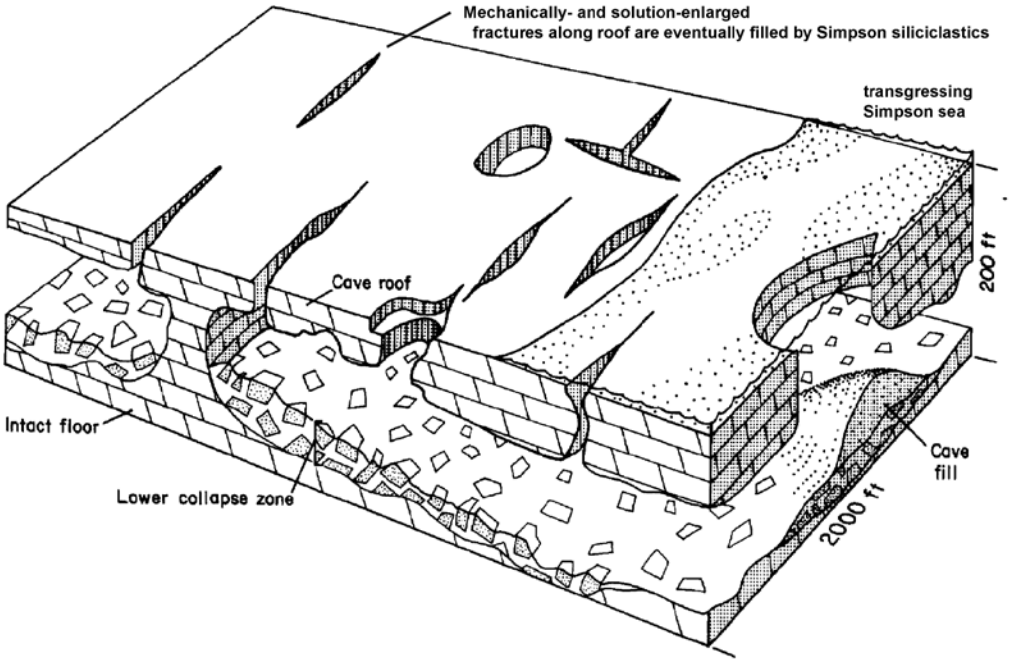

Figure 18. Block diagram showing laterally extensive cave system developed in the Ellenburger Group. Collapse breccias mantling cave floor are infilled by siliciclastics delivered by transgressive Simpson Group. Roof collapse would likely generate similar depressions (i.e, dolines) and radial fault systems similar to that observed in PSDM VC. Ultimately, the solution-enlarged fractures within roof strata are infilled by siliciclastics. Modified from Kerans, 1988.

generally dip 80–90˚. Faults intersecting the McCord- A 20H well bore are tied to their corresponding image log pick. The model contains 201 faults, which were successfully gridded using Rock Deformation Research's (RDR) module for Petrel™. The RDR module generates the grid by individually rotating each fault to a "best fit" plane. Additional faults can be observed in the 3-D seismic volume (Fig. 16). However, their inclusion is not practical because: (1) individual 3-D grid cells cannot accommodate more than one fault pillar, and (2) the project objective is to evaluate seismic VC, which is of lower resolution than the 3-D seismic volume.

Facies model

Five facies were ultimately modeled using descriptions from the Hadley L #4 core (Figure 7) and the McCord-A 20H lithology and image logs (Figure 17). These include: 1) clay, 2) dolostone, 3) matrix-supported breccias, 4) crackle breccia, and 5) chaotic breccia. Facies logs were

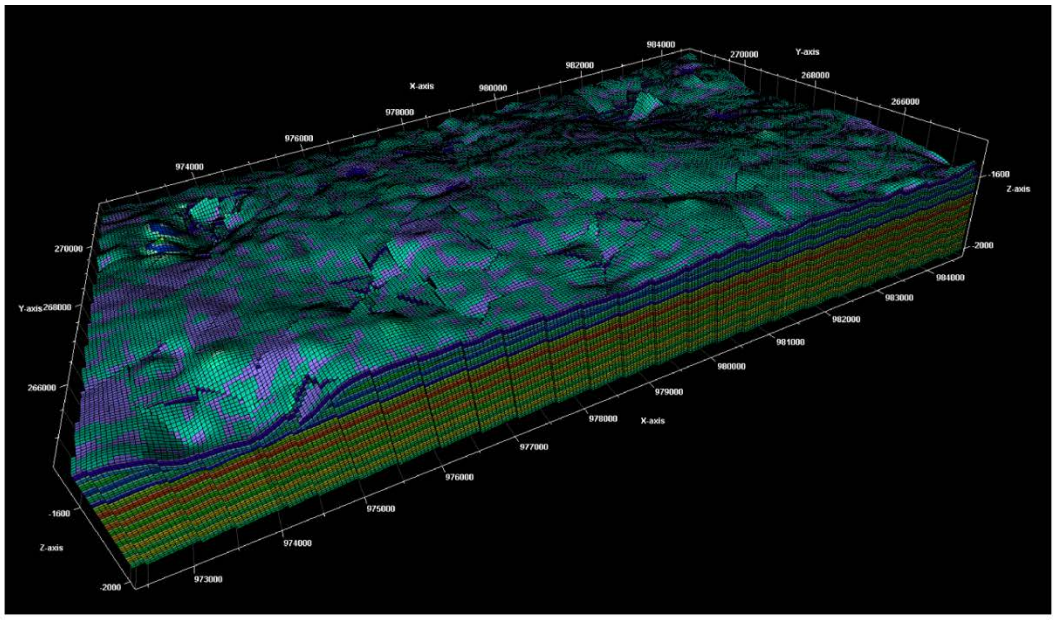

Figure 19. 3-D Model showing zonation and layering for the Arbuckle. Notice how the uppermost zone truncates the middle zone reflecting collpase of the paleocavern roof.

constructed using a sample spacing of 0.5 ft. The L. Hadley-4 well is located outside the study area (Figure 17). In order to use core descriptions of facies and routine core measurements from the L. Hadley-4 well, its logs (i.e., GR, XPHI) were compared to wells within the study area, so that it could be used as a "pseudo well." The best match is to Colahan-B29. The surface location for the Hadley L #4 pseudo well is immediately NE of Colahan-B29. The KB elevation for the pseudo well was changed so that the Arbuckle log pick intersected the Arbuckle surface. The facies logs were upscaled using the "most of" averaging method.

Well log-based facies distributions are biased in several ways. First, the McCord A 20H, prior to its landing (3618–4309-ft MD), was drilled outside the margins of the doline and passed vertically through the stratigraphic section. A facies log from this part of the test boring would be biased toward "unaffected" host strata. Then the test boring passes horizontally through the paleocavern system (4,309–5,090-ft MD). Here, the facies log is biased toward mechanically compacted rock fabrics, such as crackle and chaotic breccias. The final segment, drilled

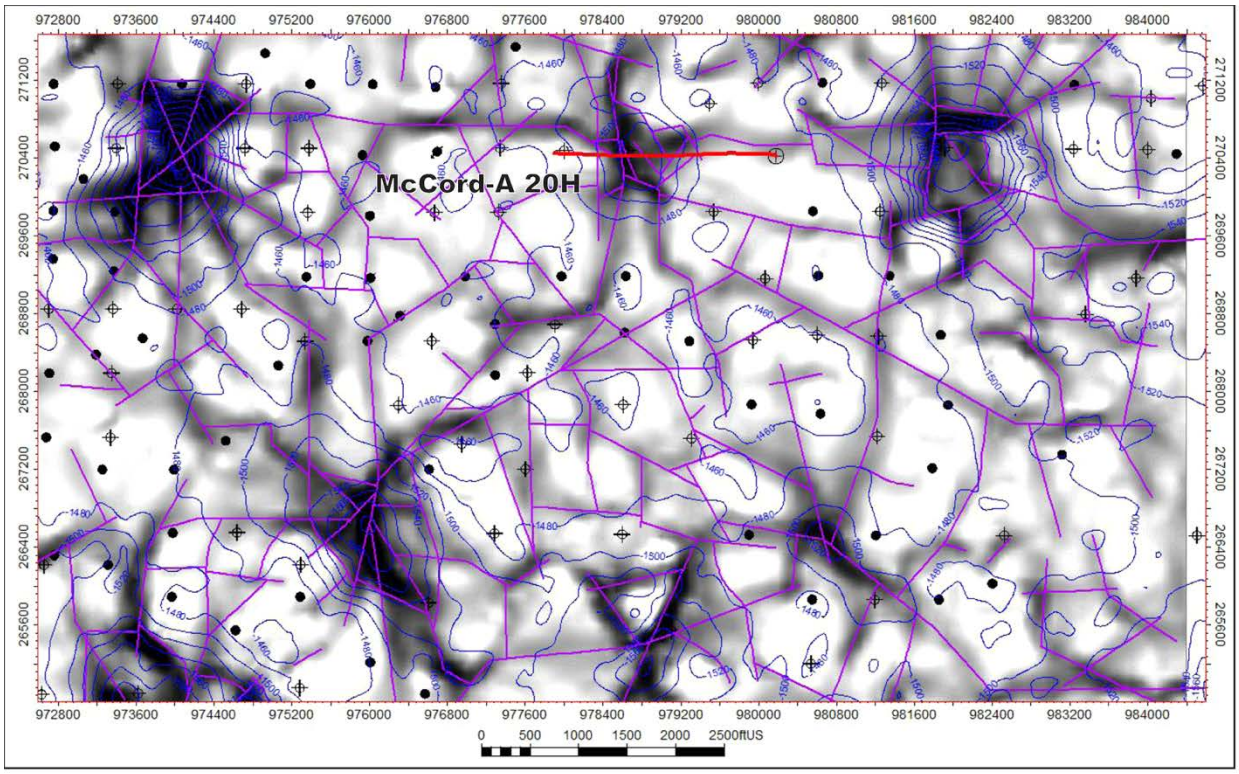

Figure 20. Map showing volumetric curvature attribute and fault model. The fault mode consists of 201 faults and was constructed using vertical pillars. Interpretations from the McCord A 20H logs suggest that negative curvature is often associated with clay-filled, solution-enlarged faults or fractures.

horizontally through unaffected host strata, is biased strongly toward bedded dolostones. The Hadley L #4 core provides additional constraint on facies distributions for the uppermost Arbuckle. Because the few basement penetrations in the area lack core or modern logs there is no information regarding facies for the lowermost (~250 ft TVD) Arbuckle section. As such, the facies distributions within the lower Arbuckle are entirely model-driven (Figure 20).

Five 2-D facies probability grids were and five vertical facies proportion curves (as functions) were constructed to constrain the spatial distribution of the karst-related facies during truncated Gaussian simulation (Figure 21). Their distribution is based upon morphology as indicated by the VC attribute and subsurface and outcrop analog studies of Ellenburger paleokarst (e.g., Kerans, 1988; Lucia, 1995). The first step was to create a geometrical trend

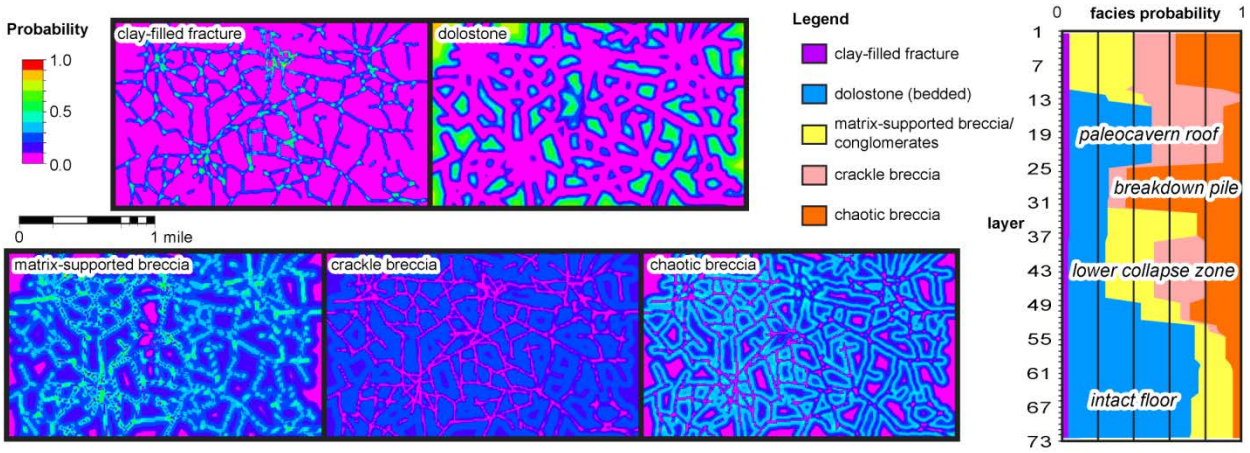

Figure 21. Facies probability maps and vertical facies probability curves. The facies probability maps were generated using distance-from-fault trend lines. Note how clays have ahigher probability of occurrence near faults, whereas bedded dolostones are situated away from from faults. The vertical facies probability curves are based upon core, image logs, and analogs (review Figure 19). The Arbuckle is capped by unconformity and often has conglomerates across its uppermost extent. Layering within the uppermost model zone locally thins to 0-ft thick.

model using the VC-conditioned fault polygons. Secondly, 2-D facies probability grids were constructed whereby the facies probabilities were a function (i.e., smoothed liner regression) of their distance from the fault trend lines. Volumetric curvature was used to delineate three main facies associations: (1) those coincident with VC-imaged fractures and faults (facies: clay-filled fractures and matrix-supported breccia); (2) those coincident with dolines (facies: chaotic and crackle breccia); and (3) those coincident with host strata (facies: bedded dolostone). It should be reiterated that strataform breccias probably formed in response to evaporite dissolution and/or burial compaction. These strata-bound, comparatively thin- bedded breccias (meter-scale) reflect an arid, peritidal to supratidal setting in contrast to seismic- scale paleocaverns linked to glacio-eustatic, vadose karst processes.

Facies were modeled using truncated Gaussian simulation (TGS) as there is a logical progression of facies away from the faults (Figure 22). Facies were modeled in the following order; 1) clay-filled fractures, 2) matrix-supported breccias, 3) chaotic breccia, 4) crackle

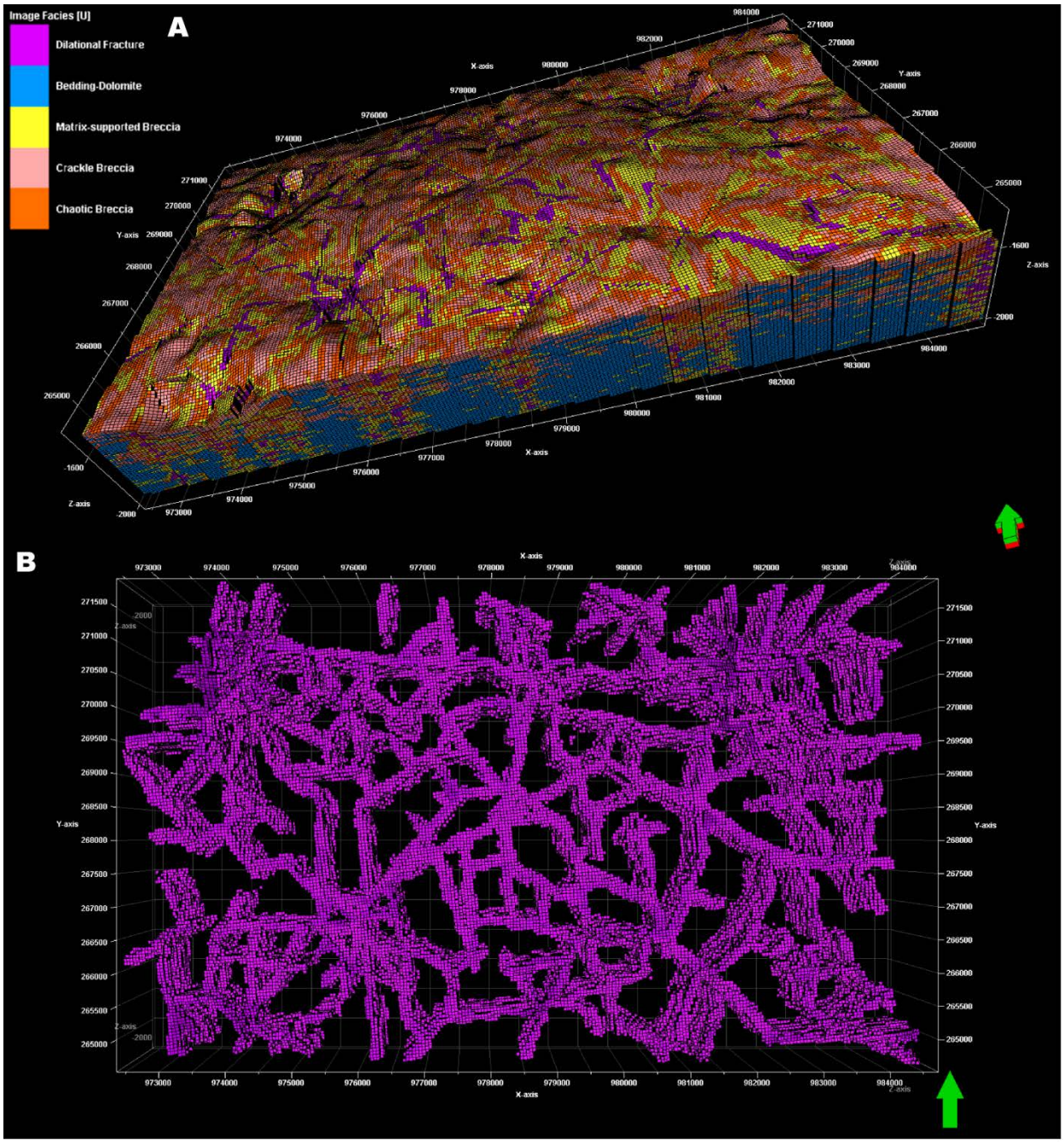

Figure 22. Facies models generated using truncated Gaussian simulation. A) Notice preferential alignment of facies relative to faults. Chaotic and crackle breccias are concentrated in upper Arbuckle and bedded dolostones are more common in the lower section (compare with Figure 20). B) Facies model displaying only cells assigned as clay-filled fractures. This fault architecture generates partially sealing faults thereby reducing transmissibility between adjacent fault-bounded blocks.

breccia, and 5) bedded dolostone. A locally varying azimuth (i.e., directional trend) was included during TGS modeling. This option aligns the major variogram direction parallel to the

faults. TGS only permits a single variogram for all facies. The major direction is set to 2000 ft and the minor direction is set to 250 ft., and vertical was set to 10-ft based upon average bed thickness. The nugget for all facies was set artificially low (0.001) as outcrop studies indicate that the nugget is largely a function of small-scale heterogeneities (<1 ft) that do not impact effective reservoir properties.

Porosity model

In contrast to well data, seismic data is areally extensive over the reservoir and is, therefore, of great value in porosity trends within models. A PSTM acoustic impedance inversion solution was generated. However, because it is in time, it offers little 3-D utility other than visualization. Petrel's™ volume attribute processing (i.e., genetic inversion) was used to derive a PSDM porosity attribute to condition the revised porosity model. A new seismic volume was created by re-sampling (using the original exact amplitude values) the PSDM 50-ft above the Arbuckle and 500-ft below (i.e., approximate basement). A cropped PSDM volume and porosity logs (XPHI) were used as learning inputs during neural network processing. A correlation threshold of 0.85 was selected and 10,000 iterations were run to provide the best correlation. The resulting porosity attribute was then re-sampled, or upscaled (i.e., average method), into their corresponding 3-D property grid cell.

The porosity model was constructed using Gaussian random function simulation (Figure 23). The porosity logs were biased to the 3-D facies model during arithmetic average upscaling. A normal porosity distribution was used as input for each facies during SGS. The same variogram settings used during facies modeling were also used during SGS of porosity. During SGS, the seismic porosity grid was used as a secondary variable for collocated co-Kriging and the correlation coefficient was arbitrarily set to 0.8 for each facies.

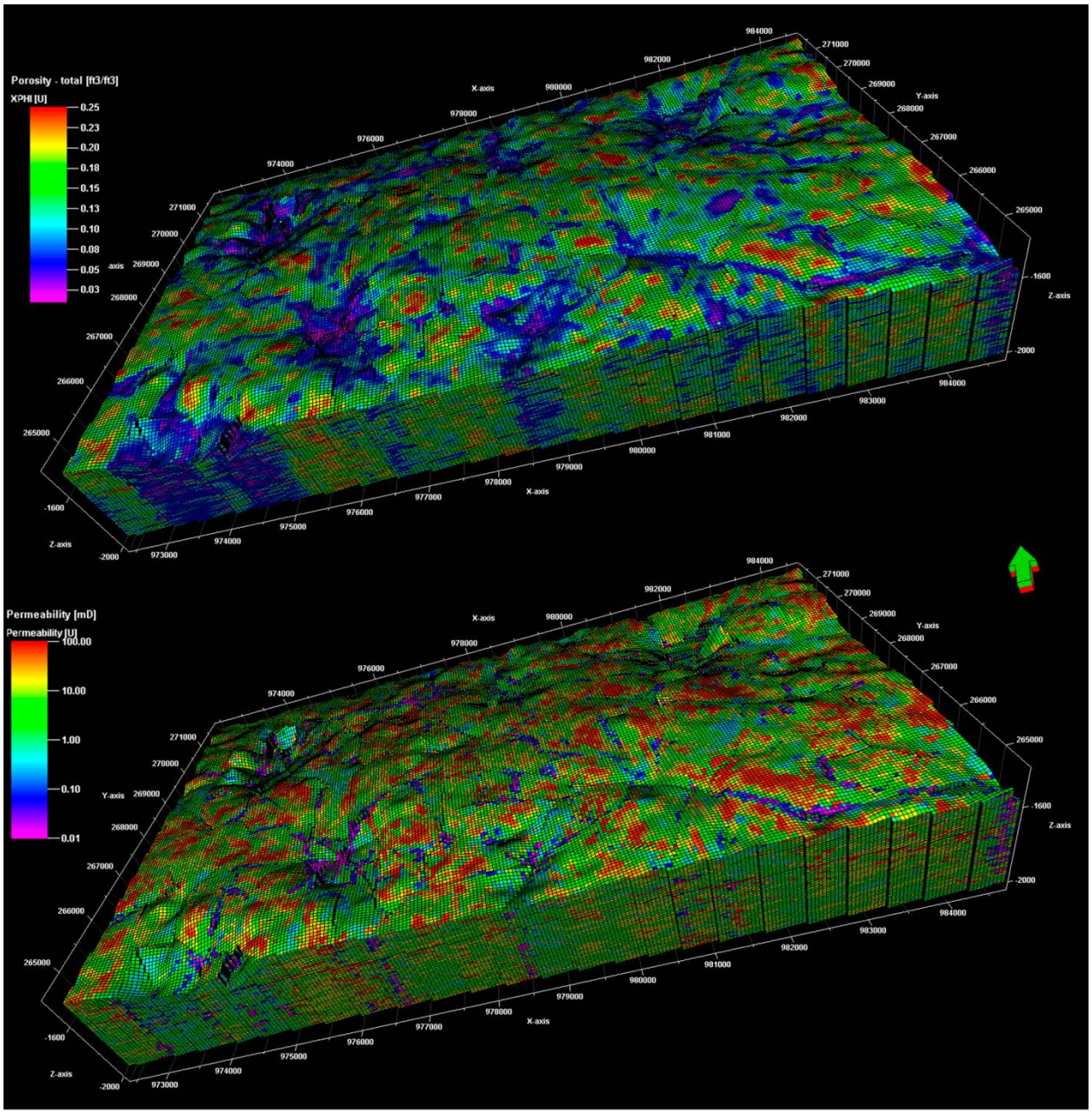

Figure 23. Porosity and permeability models were conditioned to the facies model using Gaussian random function simulation. Note how low porosity and permeability values are concentrated near dolines and fracture systems. See text for further discussion.

Permeability model

Permeability was estimated using a combination of results from drill stem tests (DSTs) and routine porosity and permeability measurements. Drill stem tests were evaluated for the Hadley

L #4 well and three wells from the study area (Colahan-B31, -B32, and -B33). Drill stem tests from the uppermost 50-ft of the Arbuckle indicate permeability ranges from 0.06–288 mD for 15 to 40 ft packer intervals with an average permeability range between 0.004 mD/ft and 12.00 mD/ft. Core measurements from the Hadley L #4 core were artificially imported into the Bemis-Shutts study area as a pseudo well to permit upscaling of permeability data. Permeability values range from 0.01–77.95 for plug samples lacking fractures. Values greater than 100 mD were associated with solution-enlarged fractures (Figure 7). These values when upscaled to the reservoir layering scale increased permeability values to an order of magnitude greater than that indicated by drill stem tests, so permeability values from the fractured samples were not included during the upscaling process.

Fifty-five permeability measurements from Hadley L 4# core plugs were upscaled using harmonic mean and bias to facies (Fig. 17). Log normal permeability distribution were used for each facies: 1) clay-supported breccias (0.01–1.00 mD; mean: 0.1mD); 2) bedded dolostones (0.46–17.30 mD; mean: 7.7 mD); 3) matrix-supported breccias (1.68–77.66 mD; mean: 23.7 mD); 4) crackle breccia (0.26–74.66 mD; mean: 10.0 mD), and; 5) chaotic breccia (0.01–77.95 mD; mean: 16.5 mD). Permeability was modeled using Gaussian random function simulation (Figure 23 B). A log normal permeability distribution was chosen for each facies because the sample size per facies is not statistically valid. Variogram ranges were set to the same range as facies. Probability maps were used as a local varying azimuth for their respective facies. Except for clay-filled fractures, each facies was conditioned to the 3-D porosity model using collocated co-Kriging and a 0.8 correlation coefficient. The resulting permeability model reveals geologic complexity consistent with paleokarst analogs where the permeability architecture is dominantly strataform within host rocks.

STATIC MODELING DISCUSSION

The RDR fault modeling module permitted gridding of complex fault geometries that are consistent with the VC interpretations of paleokarst architecture. Such complex 3-D grid geometries are critical for assessing the utility of seismic VC using simulation techniques. If the structural grids are a crude approximation of the actual fault geometry, then all subsequent simulation scenarios will abide by the idiom garbage in, garbage out. The new structural provides a skeleton upon which to (1) construct fault/fracture damage zones using discrete fracture network (DFN) models and (2) generate local grid refinements to accommodate properties related to complex permeability patterns (e.g., clay smears, cataclastites). This new structural framework provides more than 50 fault-bound segments that will foster compartmentalization studies. The new facies probability maps and facies model provide a geologically realistic approximation of the stratigraphic architecture with collapsed paleocaves, suprastratal deformation, and strataform host rock. Arbuckle geomorphology at the study area suggests capture via karst depressions and solution-enlargement of antecedent faults/fractures recorded by clastic-filled fissures. Likewise, the facies used for the model are consistent to those observed in outcrop analog studies (Loucks, 1999; Loucks et al. 2004) and subsurface studies of Ordovician paleokarst (Kerans, 1988).

SIMULATING CO_2 STORAGE CAPACITY FOR A COMPARTMENTALIZED CARBONATE RESERVOIR

The Bemis-Shutts has 594 wells producing a total of 2950 BO/day for an average of 5 BO/day per well, and it has cumulatively produced 262.9 MMBO since 1928 (Figure 24). Currently, this field is going through final stages of secondary oil recovery. Its operational pressure is 1100 psi and temperature is around 110-120˚ F.

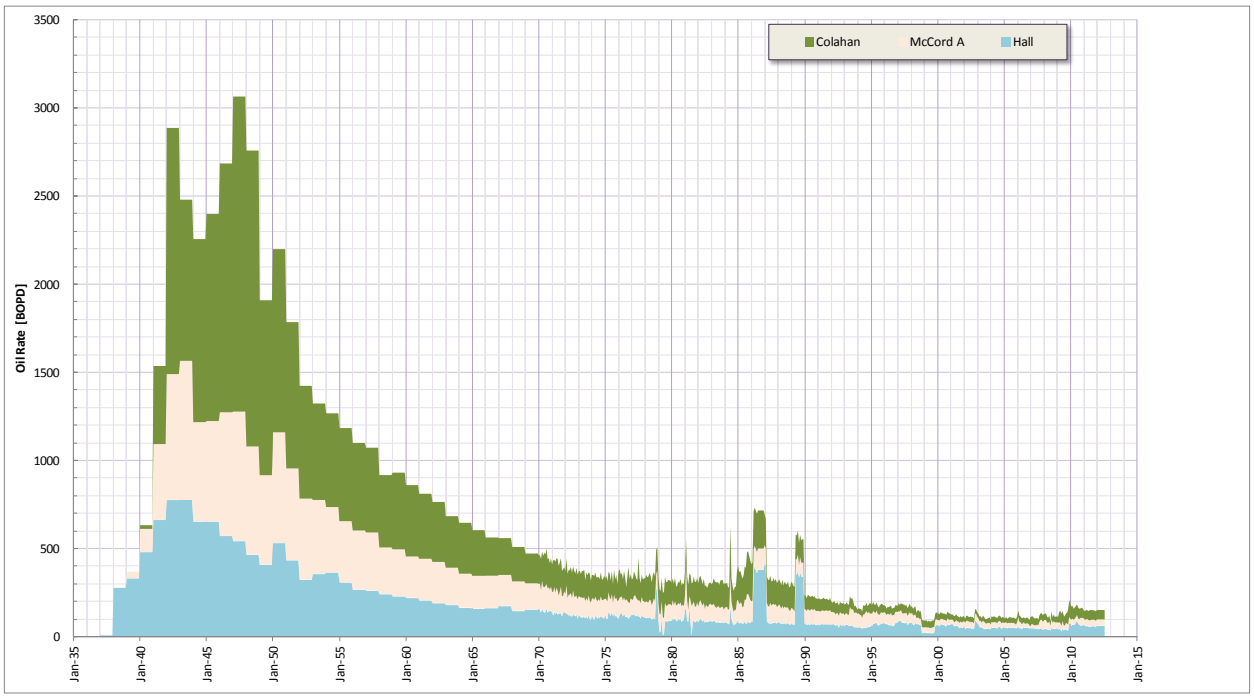

Figure 24. Production from KGS Database for Leases of Interest.

RESERVOIR MODELING

Model set-up

A numerical simulation model has been created for the Bemis-Shutts Arbuckle to evaluate flux between fracture blocks and the applicability of directional wells in this style of reservoir. Water saturation was modeled using Lucia (1999). Water saturation were calculated using the following rock fabric numbers: 1) matrix-supported breccias (rfn 1); 2) dolostones, crackle breccias, chaotic

breccias (rfn 2), and; 3) clay, which includes clay-supported breccias (rfn 3). The simulation model focused on the fault block including or adjacent to the McCord-A 20H well. The model has been validated as a predictive tool by history matching individual well production history. The Leases in the study area have been on production from 1937, but the principal validation is based on well tests and historical water cut performance over the period from September 1990 through December 2011.

Static model integrating the petrophysical and seismic data with a geologic interpretation was imported from Petrel. Specific reservoir structure and data were exported from the static model for use in the dynamic numerical simulation models. For these studies, numerical simulation modeling is carried out utilizing the Computer Modeling Group simulation tools IMEX and GEM.

A pseudo steady state (Fetkovich) aquifer function is connected to the bottom of the model. Aquifer parameters (height, area, porosity, permeability, etc) are history matching variables. Rock compressibility was set to 5.0E-6 psi-1 at 1500 psi. The reservoir fluid properties were determined from correlations and the oil PVT report for the Peavy No B-1 well which is located in the nearby field.

Oil production data, by lease was available on an annual basis from 1937 to 1970 and monthly from 1970 to 2011. Also, the number of wells available for production in each lease was available over this period. But, allocated production by well was not available. For purposes of these models, the indicated lease production was assumed to be divided equally by the number of wells shown as available for production.

SCAL was not available for the Bemis-Shutts reservoir but typical values for similar reservoirs were taken from the available literature. For the reference case a residual oil saturation of 35%, a connate water saturation of 27%, and a Krw at residual oil of 0.25 were assumed. Note that these endpoints are history matching variables and the values assumed were selected to ensure that they would serve as limiting values.

The water saturation for the reservoir model was taken from static model. However at time 0, the simulation model is initialized assuming capillary equilibrium. For this, a capillary pressure curve is estimated from the saturation versus height above free water level as illustrated in Figure 8 – the capillary pressure function is the black line with the yellow markers.

This capillary pressure function was applied to an uncertain original oil water contact (OWC) near 1550 ft SS. For capillary equilibrium, IMEX calculates first an initial cell pressure based on height above the contact and density differences between the oil and water. With this pressure the software then calculates a capillary pressure shift from the capillary pressure curve to match the input water saturation. This process ensures that the model is initially in equilibrium.

Relative Permeability

Six sets of relative permeability curves for both drainage and imbibition were calculated for the nine rock types. These sets of relative permeability curves were calculated based on a recently patented formula (SMH reference No: 1002061-0002) that relates the end-points to Reservoir Quality Index (RQI), thereby resulting in a realistic relative permeability data set. The validation of the method is presented below under “Validation of the Capillary Pressure and Relative Permeability Methods”. Literature experimental studies including Krevor and Benson et al.,

(2012 and 2015), indicate that the maximum experimental CO_2 saturation (SCO_2max) and maximum CO_2 relative permeability ($KrCO_2$ max) in higher permeability samples typically do not reach their actual values and are lower than expected. The authors note that the cause of low experimental endpoints are the unattainable high capillary pressure in the high permeability core samples. Calculations based on the new patented method addresses and resolves this issue. The highest maximum CO_2 relative permeability ($KrCO_2$ max) for drainage curves from literature (Bennion & Bachu, 2007) is 0.54 which is lower than expected; however, the highest maximum CO_2 relative permeability using the new method is 0.71, which is a more realistic value. As noted above, measured relative permeabilities from literature do not represent the endpoints of relative permeability curves and they need to be adjusted. Using this new method, SCO_2max and $KrCO_2max$ are scaled up to reasonable values.

Highest and lowest Corey CO_2 exponent values from (Bennion & Bachu, 2010) were selected and they were assigned to the nine RQIs in a descending order from high to low. Corey Water exponents for different permeabilities from literature did not show much variability. Therefore, average values were used for both drainage and imbibition curves. Relative permeability curves for RQI of 0.35 is presented in Figure 25. Residual CO_2 saturation (SCO_2r) for calculating imbibition curves was needed. SCO_2r was calculated based on a correlation between residual CO_2 saturation (SCO_2r) and initial CO_2 saturation (SCO_2i) (Burnside and Naylor, 2014).

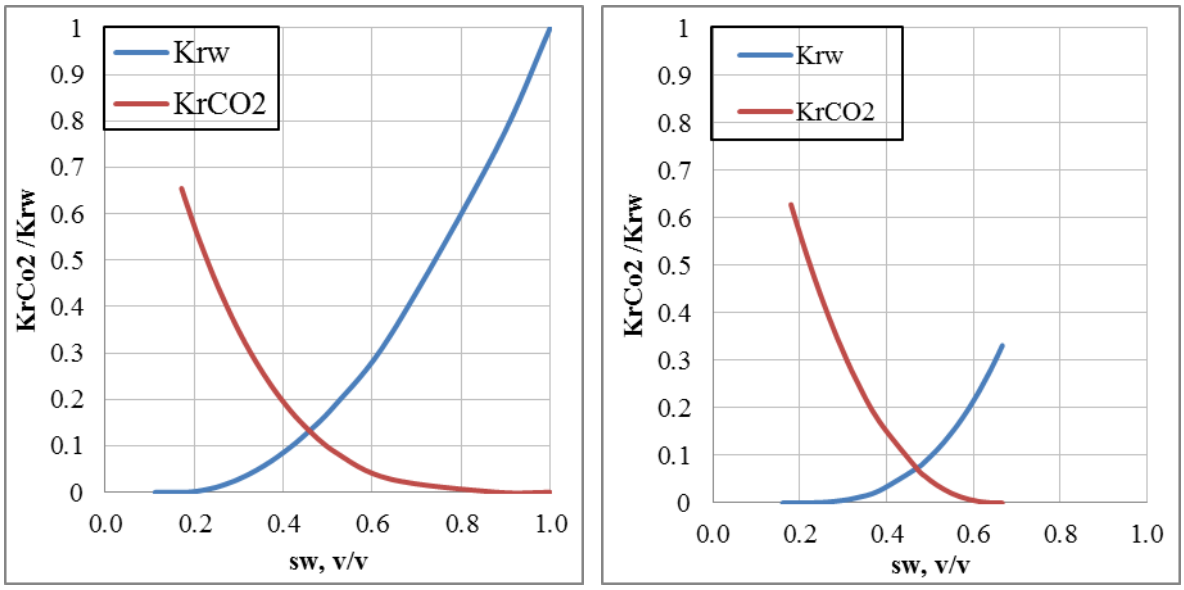

Figure 25. Example of calculated relative permeability for drainage (left) and imbibition (right)

Capillary pressure curves

Six capillary pressure curves were calculated for drainage and imbibition for nine RQI values based on a recently patented formula (SMH reference No: 1002061-0002). The formula constitutes a function for the shape of Pc curves and functions for the end-points that are entry pressure (Pentry) and irreducible water saturation (Swir). The end-points are correlated to RQI. Pentry was calculated from entry radius (R15) and Winland (R35). There is a relationship between R35 and R15 and a relationship between Pentry and R15; therefore, Pentry can be calculated from R15 derived from R35. Swir was calculated from the NMR log at a Pc equal to 20 bars (290 psi). For calculating the imbibition curves, another term which is the residual CO_2 saturation (CO_2r) was needed. CO_2r was calculated from a relationship between initial CO_2 saturation and CO_2r that was discussed above. The capillary pressure curves for drainage and imbibition for RQI of 0.35 is presented in Figure 26.

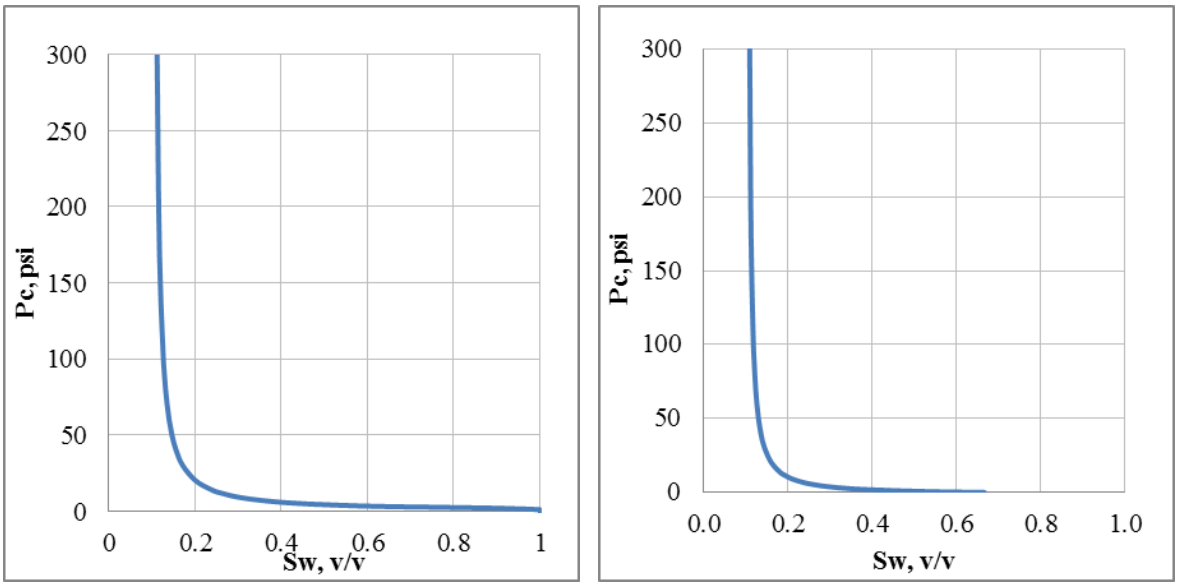

Figure 26. Example of calculated capillary pressure curves for drainage (left) and imbibition (right).

Rock type assignment

Six rock types and corresponding tables with capillary pressure hysteresis were developed based on RQI ranges, where RQI is calculated for each grid cell using the formula:

$$RQI = 0.0314\sqrt{Perm/Porosity}$$

Using RQI ranges, rock types are assigned using CMG Builder's Formula Manager. The resulting maps of rock types distribution in the model is outlined in Figure 27. The division of the 6 rock-types (RT) was based on dividing the irreducible water saturation into 6 ranges to find their equivalent RQI as shown in the table below. Relative permeability and capillary pressure curves were calculated for each of the 6 RQI.

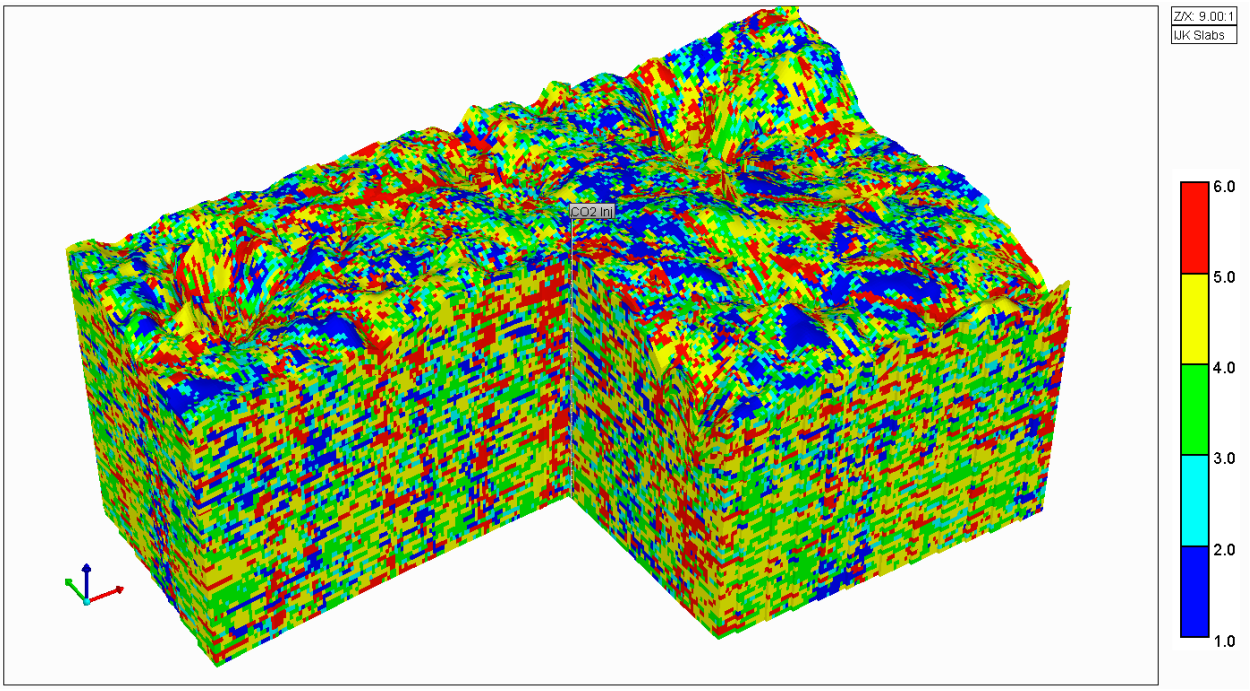

Figure 27. Rock type distribution model

History matching

For history matching, data was available monthly and from test separator for a period from 1994 to 2011. It is this monthly data, especially the water cut information that is used to validate the simulation model.

History matching was carried out using the CMG automatic history matching software program CMOST. Uncertain history matching parameters include: 1) Aquifer Parameters; 2) Angle, radius, thickness; 3) Depth to Oil Water Contact; 4) Reference Pressure (at the oil water contact); 5) Relative Permeability shape and end-points; 6) Gravity Stable or Corey; 7) Critical water saturation; 8) Residual oil saturation; 9) Transmissibility (i.e. Connectivity or Tortuousity); 10) Variable by fault block; 11) Anisotropy; 12) Pore volume modifiers by fault block. The objective functions for the history matching were the water cut match for the 4 wells.

However, it is important to note that history match is not a unique solution. Several suitable matches could be derived under different values for the uncertainty parameters. Nevertheless, the comparison of history matching runs where fault properties and fluxes were included into a mix of variables versus history matches without structural elements suggest that accuracy of a history match depends of inclusion of structural elements and compartments.

The results of the history match showing an oil production and water cut case for the combined wells is illustrated in Figure 28. In this figure the dark green line represents cumulative oil production, the lighter green line represents oil rate in stb/day. The black line shows the water cut – which is very high throughout the productive life of these wells.

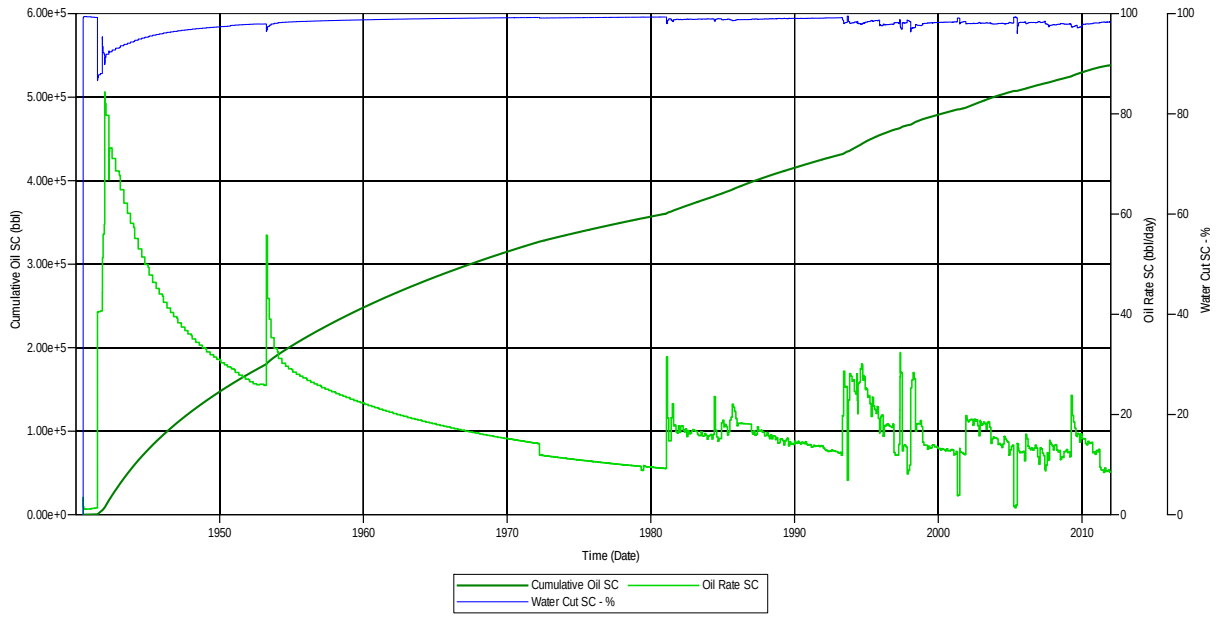

Figure 28. Full Model Calculated Production

CO_2 geological storage capacity estimations

Considerable effort has been directed at simulating plume behavior in response to variable transmissibility values along compartment boundaries. In order to calculate CO_2 storage potential, develop optimization strategies for CO_2 storage operations, and evaluate influence of natural

fractures and karst features on fluid flow, several injection strategies were tested. Among tested injection scenarios are: (1) injection via horizontal wells; (2) injection via one and several vertical wells; and (3) injection with additional brine production for pressure and storage capacity management. For more realistic calculations bottom-hole pressure (BHP) for injection wells was capped at 2,750 psi, 90% of typical fracture gradient in Arbuckle. Reservoir conditions were altered to better accommodate CO_2 geological storage scenario in a more suitable setting. The reservoir pressure was set to 2000 psi and reservoir temperature to 140 F, which resembles conditions of typical Arbuckle reservoir in a South-Central to South-Western part of Kansas.

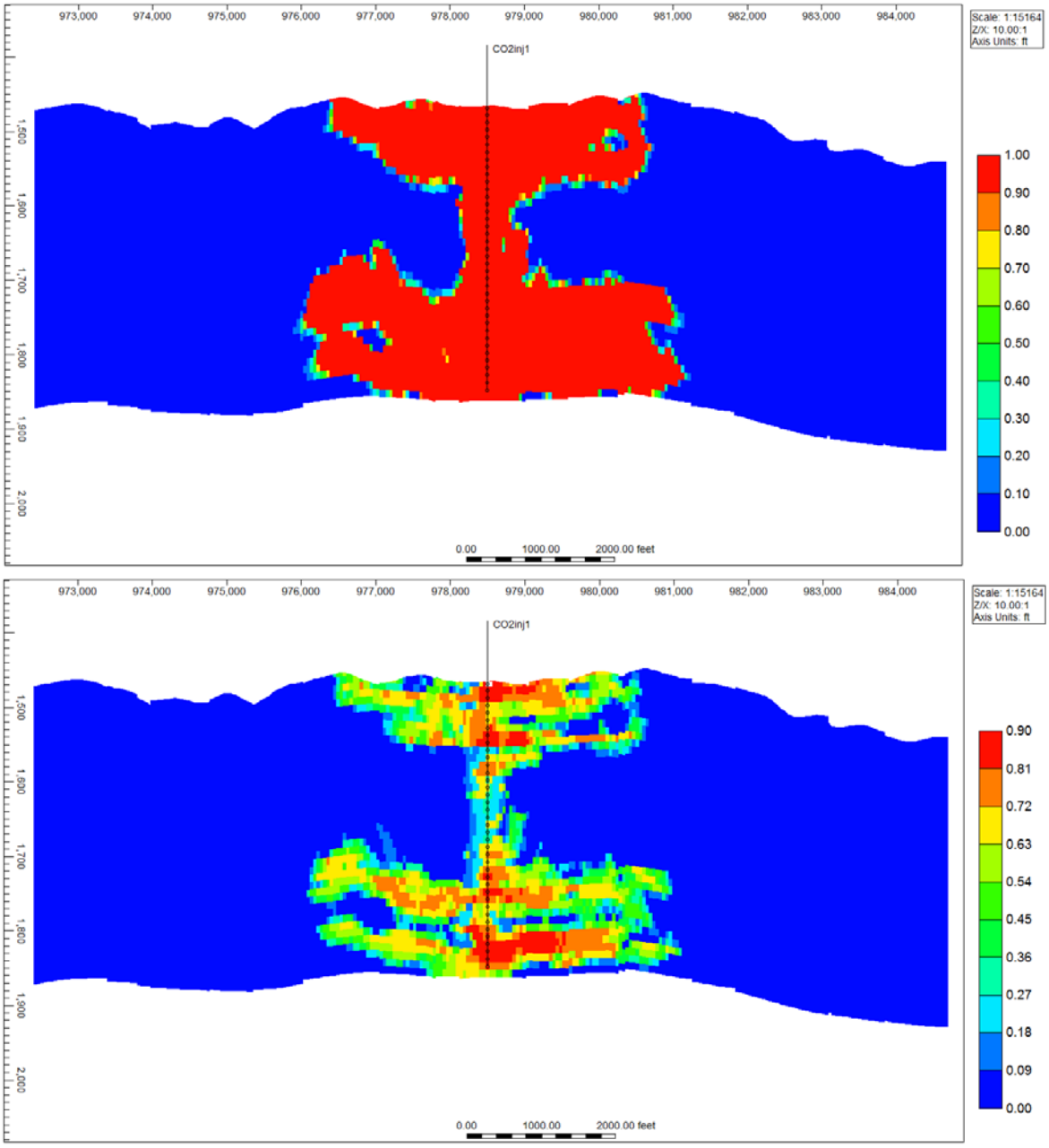

Figure 29. West to East vertical cross section that is comparing total CO_2 concentrations in the reservoir and free phase supercritical CO_2 for vertical injection well set-up.

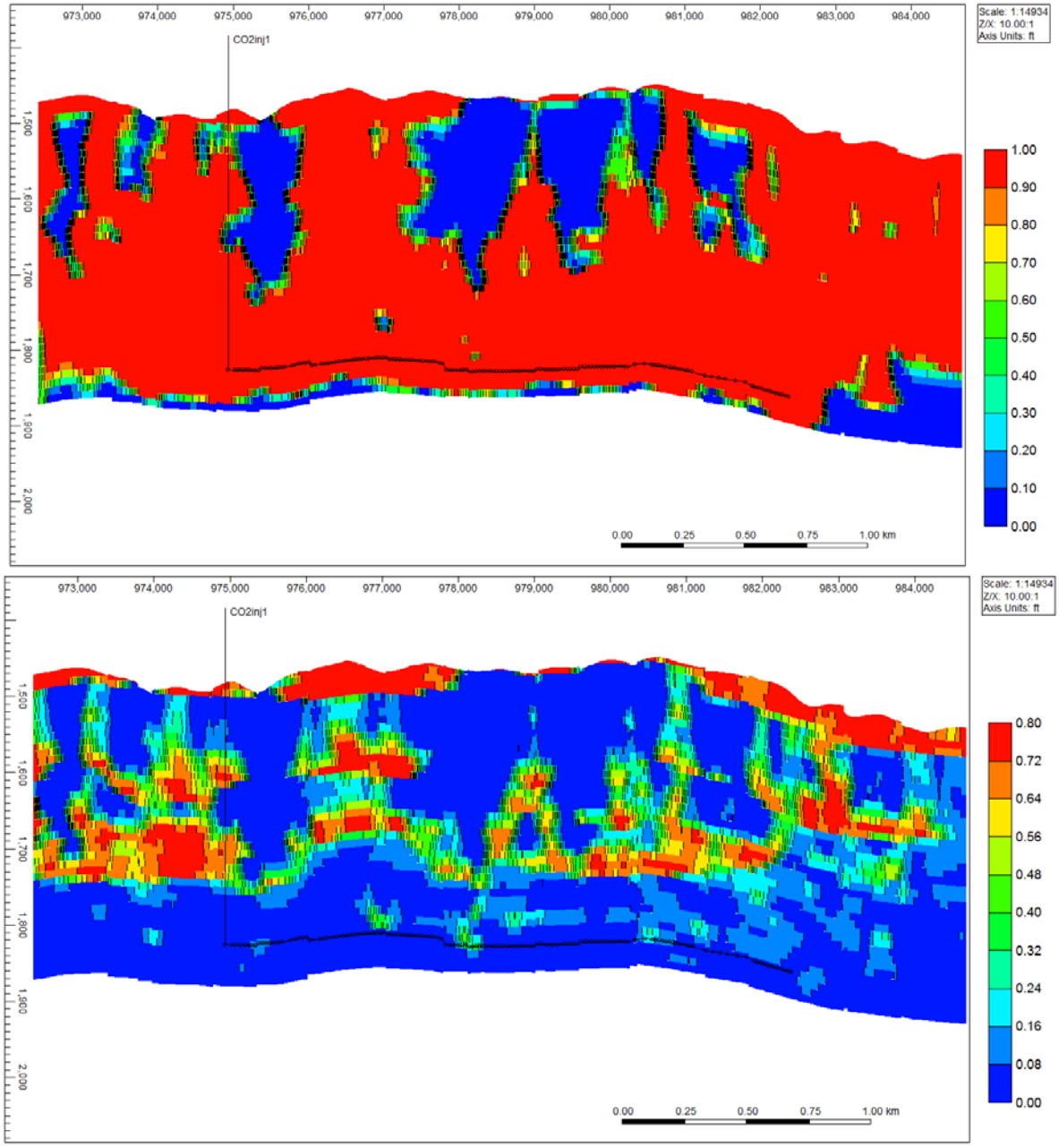

Figure 30. West to East vertical cross section that is comparing total CO_2 concentrations in the reservoir and free phase supercritical CO_2 for horizontal injection well set-up.

Overall, for the simulated portion of a Bemis-Shutts field, the best injections set-up a is a horizontal well drilled for ~5000 ft in horizontal direction across existing compartments through the reservoir. According to Table 1 and Figures 29 and 30, for all considered scenarios; closed vs. open boundary, co-production of brine, etc., horizontal well shows optimal results for geologic

storage of CO_2. BHP is maintained lower levels than using vertical well (Figure 31) with higher efficiencies for CO_2 structural, dissolution, and residual trapping (Figure 32). Co-production of formation water is optimal at a rate of ~1000 bbls/day through 4 producing wells with perforations at the top 50 ft of Arbuckle reservoir. Increasing production rate to ~2000 bbls/day did not equally increase CO_2 storage capacity for this given part of a field. Additional CMOST simulations supported these findings.

When estimating CO_2 permanent storage potential for a vertical well set-up, it was calculated that 68% of CO_2 will be structurally trapped, 17% will be trapped through residual trapping mechanism, and 15% will be dissolved in formation brine (Figure 32). However, it was found that horizontal injection well set-up allows for more efficient dissolution and residual trapping and improves both trapping mechanisms to Mineralogical trapping was calculated to be insignificant and it is described in more detail below.

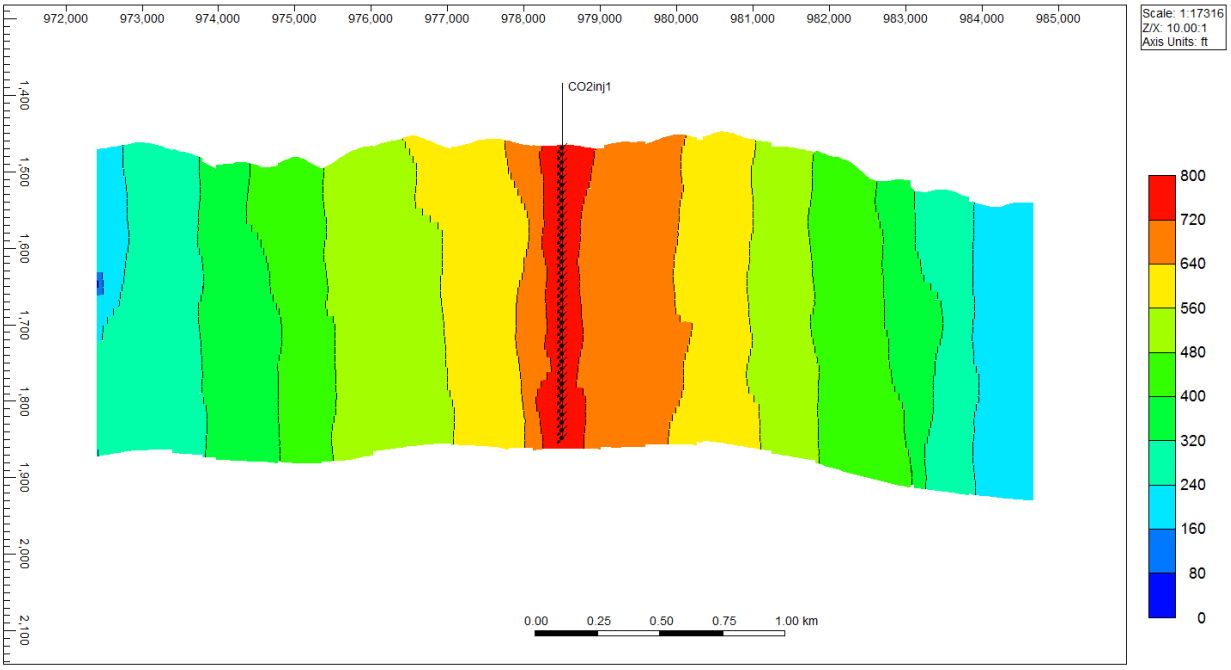

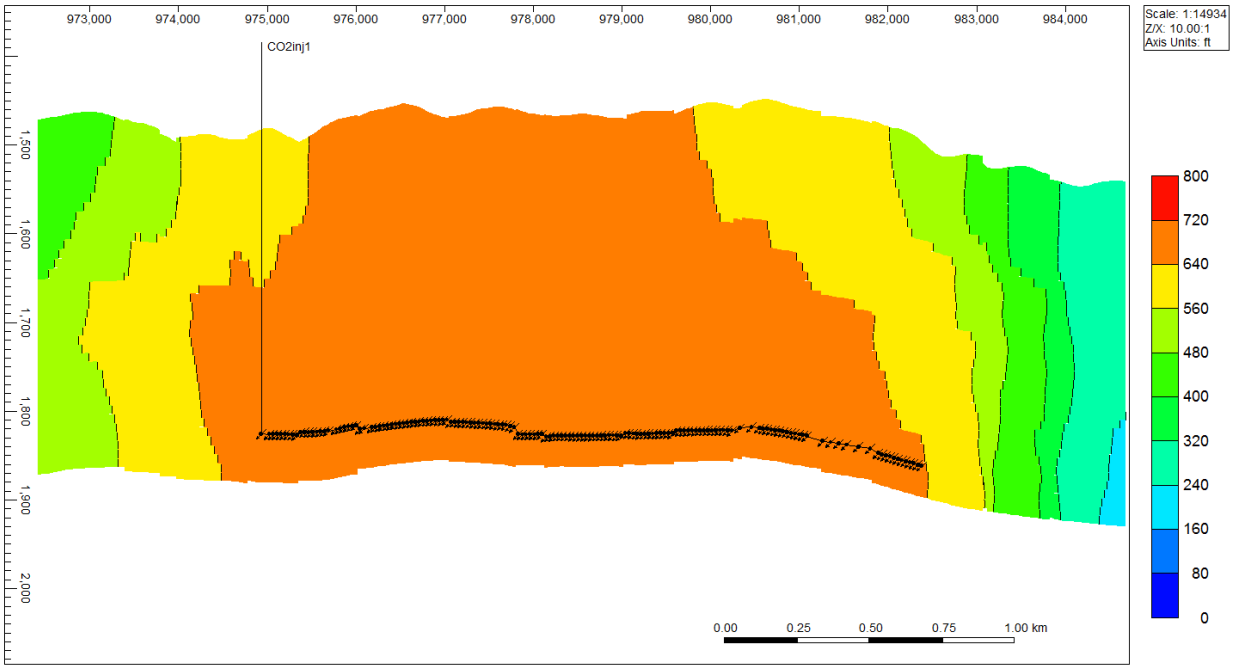

Figure 31. West to East vertical cross section that is comparing maximum reservoir pressure (psi) distribution for vertical vs. horizontal well injection scenario

Table 1. Storage capacity estimations for different modeled conditions

Conditions	CO_2 **storage capacity, million tons**
DOE formula calculated	6.6
No heterogeneity modeling domain, vertical well, closed boundary	1.2
No heterogeneity modeling domain, vertical well, open boundary	4.6
No heterogeneity modeling domain, horizontal well, closed boundary	2.1
No heterogeneity modeling domain, horizontal well, open boundary	5.8
Geological model, one vertical well, closed boundary	1.1
Geological model, one vertical well, open boundary	2.1
Geological model, horizontal well, closed boundary	3.3
Geological model, horizontal well, open boundary	5.3
Geological model, open boundary, one vertical well with 4 wells co-production at 500 bbls/day	4.5
Geological model, open boundary, one vertical well with 4 wells co-production at 1000 bbls/day	5.1
Geological model, open boundary, one vertical well with 4 wells co-production at 1500 bbls/day	5.2
Geological model, open boundary, one vertical well with 4 wells co-production at 2000 bbls/day	5.2
Geological model, open boundary, horizontal well with 4 wells co-production at 500 bbls/day	6.5
Geological model, open boundary, horizontal well with 4 wells co-production at 1000 bbls/day	6.7
Geological model, open boundary, horizontal well with 4 wells co-production at 1500 bbls/day	7.1
Geological model, open boundary, horizontal well with 4 wells co-production at 2000 bbls/day	7.2

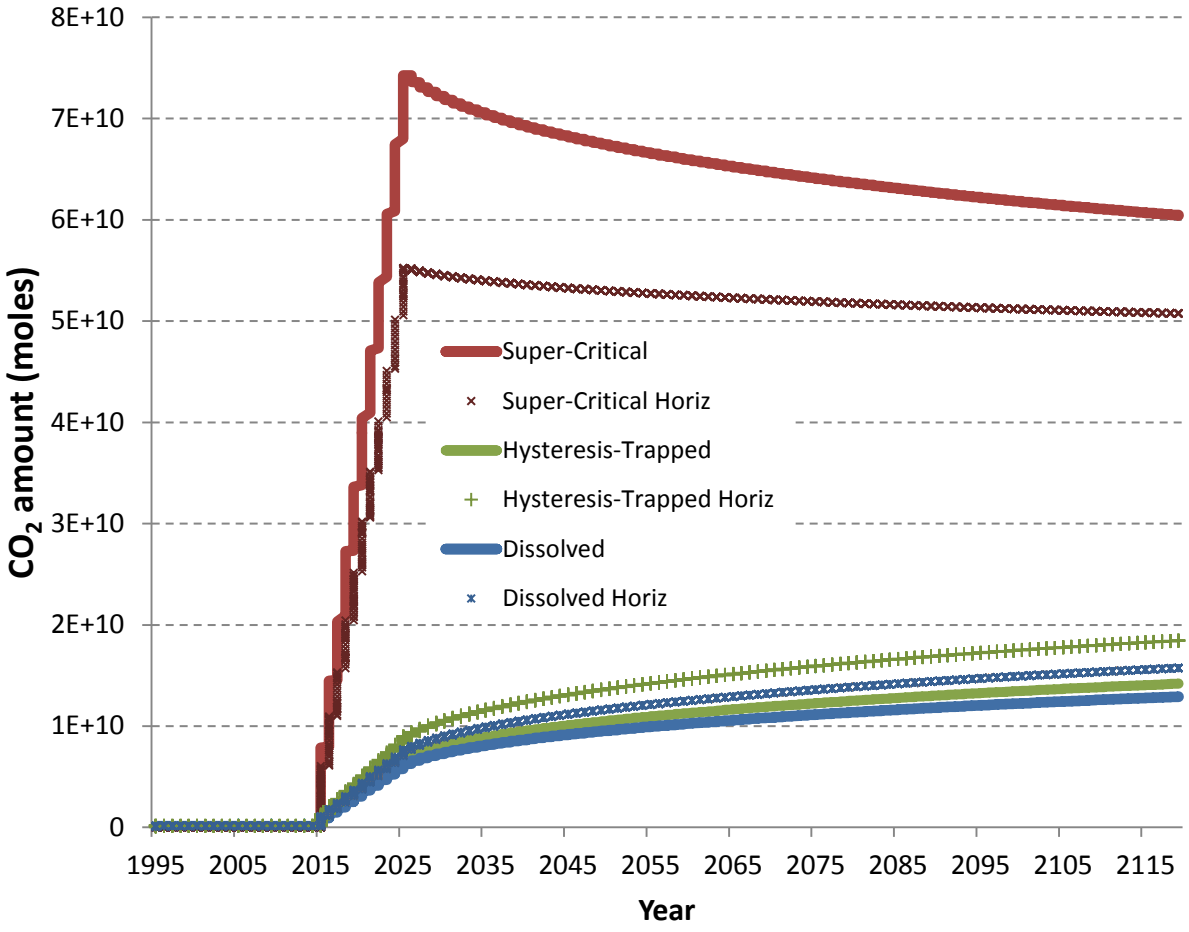

Figure 32. Comparison of CO_2 amounts of free-phase supercritical, dissolved, and residual hysteresis-trapped CO_2 after injection in reservoir via horizontal and vertical wells.

As a result of numerical simulations it was that found fault and fracture transmissibility affects CO_2 mobility and reservoir performance and should be included in decision making process for the well location determination (Figure 33) and fault and fracture transmissibility complicates other field operations which might be implemented in order to increase CO_2 storage capacity and injectivity, for instance, water management, such as water production or injection, will be affected by the presence of faults, fractures, and other structural elements in the reservoir.

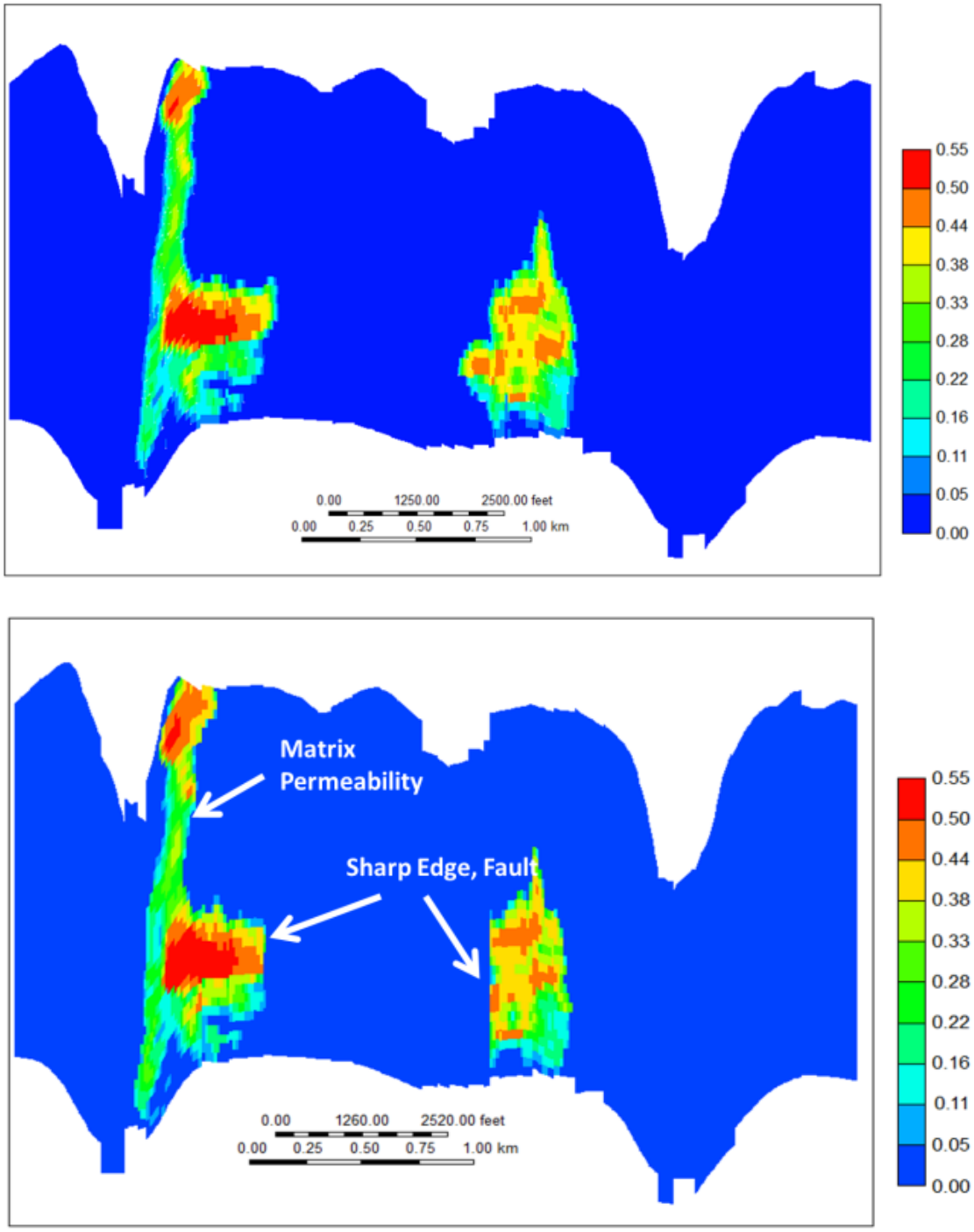

Figure 33. Vertical cross section from west to east: CO_2 movement front with fault permeability multiplier set to 1 - transmissible (top) and with the fault transmissibility multiplier set to 0 – not transmissible (bottom). The flow of CO_2 is determined by permeability and faults (fractures). In this case the vertical flow is possible because of permeability pathway associated with the fault, and if the fault transmissibility is set to 0 the vertical flow is still happening. In contrast, the plume on the right side of each image is not moving upwards, due to low permeability barrier in the Mid. Arbuckle.

CO_2, brine, and rock interactions

Twelve water samples from the Bemis-Shutts field site were analyzed via Inductively Coupled Plasma Optical Emission Spectrometry (ICP-OES) and by Inductively Coupled Plasma Mass Spectrometry (HR ICP-MS) and Ion Chromatography (IC) techniques for dissolved ions and total metal concentrations at Kansas State University.

Several spatial observations about the behavior of some of the constituents were analyzed. Although no strong correlation was derived, it is possible to speculate that there are two main groups of elements that act similarly, and then a few of outlier elements with no significant correlation to any other elements. Elements of Group 1, which show a significant west to east increase from Dehoff 'A' 7 well to Dehoff 'A' 6 well, this group includes Na, Ca, Mg, and Cl. These elements show good correlation with each other and are generally homogenous across the study site except across a sharp gradient located between Dehoff 'A' 7 and Dehoff 'A' 6. Group 2 elements (are Li, S, Si, and SO4) that show a significant decrease from Dehoff 'A' 7 to Dehoff 'A' 6. These elements exhibit less homogeneity than group 1 across the study site, but still display one main gradient again located between Dehoff 'A' 7 and Dehoff 'A' 6 (Figure 34 and Table 2). However, this gradient is the inverse of group 1 elements (they decrease). Potassium is similar to group 1 elements in that it increases from Dehoff 'A' 7 to Dehoff 'A' 6, however it is less homogenous throughout the rest of the study area with a significant minimum in concentration in the center of the study area.

Overall, we may be able to justify that in this study site encompassing the 12 wells the hydrogeochemistry of the brines indicates two major hydrochemical facies, as in group 1 and group 2. One particular structural control either in the form of faults or lineaments may be interpreted to be present as a north-south trend in between Dehoff 'A' 7 and Dehoff 'A' 6 wells.

These hydrochemical facies may indicate two separate formations of provenance for the two groups.

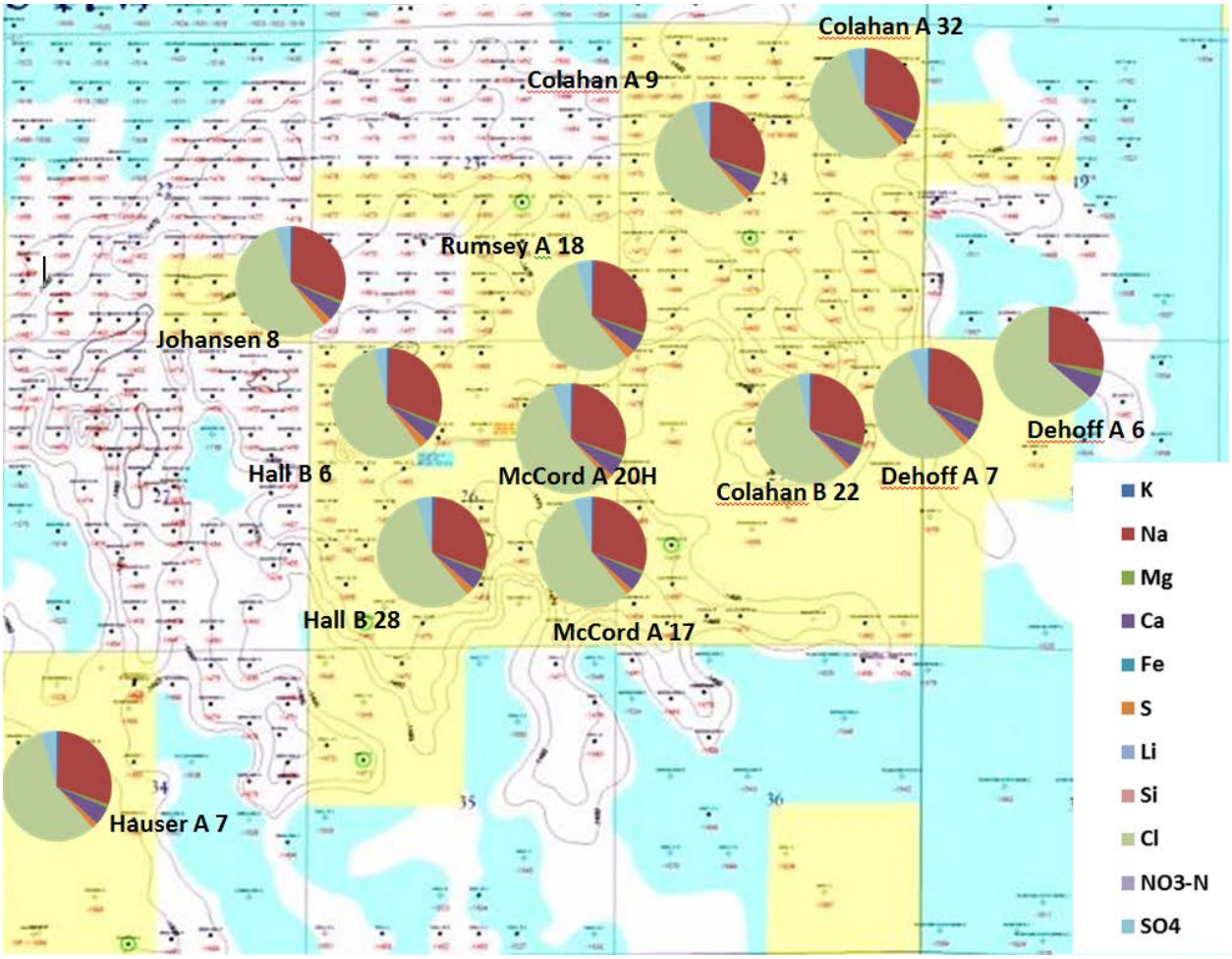

Figure 34. Brine sample concentration charts from each sampled well in a field

Table 2. Brine anion and cation concentrations for each sampled well in a field analyzed

	Cation Concentrations (mg/l)								Anion Concentrations (mg/l)		
Well ID	**K^+**	**Na^+**	**Mg^{2+}**	**Ca^{2+}**	**Fe_t**	**S**	**Li^+**	**Si**	**Cl^-**	**NO_3-N**	**SO_4^{2-}**
Colahan 'A' #32	387	12800	442	2390	0.16	1050	8.21	6.5	24200	<10	2380
Colahan 'A' #9	395	13100	459	2380	0.17	944	8.16	6.5	25200	<10	2410
Colahan 'B' #32	369	13100	585	2620	0.22	640	7.91	6.6	26500	41.4	1530
Dehoff 'A' #6	435	29200	2160	7290	0.24	35	3.54	4.6	68800	22	<30
Hall 'B' #28	399	13100	457	2300	0.19	1100	8.05	6.7	25200	<10	2070
Hall 'B' #6	400	13200	456	2180	0.18	1240	8.17	6.6	25100	<10	1590
Hauser 'A' #7	418	13000	477	2400	0.27	792	8.91	6.8	25100	<10	2000
Johnasen #8	393	13700	476	2350	0.2	1250	7.95	6.7	25700	<10	1970

McCord 'A' #20H	376	13000	454	2400	0.21	898	7.99	6.4	25000	23.5	2350
Rumsey 'A' #18	395	13000	443	2270	0.27	1270	8.04	6.5	25300	<10	2070
McCord 'A' #17	391	12800	454	2350	0.21	828	8.32	6.6	24200	<10	2290
Dehoff 'A' #7	395	12400	436	2200	0.43	802	8.31	5.9	23500	<10	2390

Batch experiments and geochemical models provide insight as to the types of weathering reactions that may take place under high CO_2 pressure conditions in the Arbuckle reservoir. Models indicate the minerals most affected by exposure to CO_2-laden brine include anhydrite, calcite, dolomite, ankerite, and siderite. Pyrite is also predicted to dissolve, but the wt% of pyrite in the system is very low. The rates of dissolution for quartz, illite, and kaolinite, are relatively slow, and as such, the effects of CO_2 exposure on those minerals are expected to be minimal. The model predictions are also reflected in the experiment results. Brines have higher concentrations of Ca^{2+}, Mg^{2+}, HCO^{3-}, and SO_4^{2-} after exposure to CO_2. The increases in ion concentrations are consistent with the dissolution of dolomite and anhydrite. Dissolution features on dolomite grains were observed via SEM in CO_2-reacted Arbuckle.

Geochemical models of the experiments predict an overall decrease in rock mass of up to 0.65% over the course of 32 days. This dissolution prediction is considered a maximum estimate for the following reasons:

1) Rock samples were powdered before addition to experiments. Powdering the rock increased the surface area, which also increased the mineral reaction rates (e.g. Alemu et al., 2011). Reaction kinetics are expected to be slower in the actual reservoir and seal, as the reactive surface area per gram is less than that of the experiments.

2) The water/rock ratio of the experiments is ~1500 times higher, on average, than in the reservoir injection zone. A higher water/rock ratio translates to increased reactivity (i.e. more fluid-mineral contact means a higher reaction rate) (e.g. Alemu et al., 2011).

3) Experiment brine salinity was 61-65 ‰, which is at the low end for the Arbuckle Reservoir. Injection zone salinity is higher, at ~120 ‰ (average sea water salinity is 35 ‰) (Arbuckle reservoir brine chemistry data from Scheffer, 2012). Models with higher salinity brines (at or near 120 ‰), but with mineral composition and surface area identical to the Arbuckle experiment models, predict less total rock mass dissolved (a net decrease in rock mass of 0.56% rather than 0.65%).

Models depicting a decrease in CO_2 pressure (e.g. after injection ceases, and/or as the CO_2 plume migrates/dissipates) predict that pH will rise, and carbonate mineral precipitation will be the dominant reaction pathway.

Geochemical reservoir model was constructed with CMG GEM and WinProp software. The geochemical model took into account following minerals: halite, dolomite, calcite, anhydrite, gypsum, hematite, siderite, and pyrite. This model was correlated with the laboratory observation and previous reaction kinetics modeling studies conducted with the Geochemist Workbench and PHREEQC software.

Mineral dissolution and precipitation was predicted by this model; however, the volume of the minerals participating in reactions is predicted to be small (less than 0.5 % of minerals volume in contact with CO_2 predicted by laboratory studies and previous modeling). For instance, the changes in porosity during the course of injection and many years after the injection are predicted to be less than ±0.13%.

SIMULATION DISCUSSION

The implication of this model for reservoir simulations is the fluid flow constrained not only by faults transmissibility properties but also by grid properties, which is more accurate

representation of a fluid flow, comparable to actual reservoir flow. As a result, storage capacity estimations were greatly affected by the presence of karst features and associated facies, and, although structural features are not presenting an ultimate barrier or a conductive path for a fluid, they direct the flow and in many cases limit available storage space which could be impacted by an injector well.

Horizontal injection well set-up is more suitable for CO_2 storage scenario in fractured and compartmentalized Arbuckle reservoir due to higher efficiencies of CO_2 storage mechanisms, such as brine dissolution, residual, and structural trapping. Horizontal well also allows for a more sustainable pressure management.

Formation water co-production is enhancing CO_2 storage capacities and allows for better reservoir pressure management as well; however, rate selection must be estimated prior filed operations for optimal field performance.

Mineralogical interactions of injected CO_2 and formation rocks and brine are expected to be minimal due high water concentrations and mineralogical composition. Models indicate the minerals most affected by exposure to CO_2-laden brine include anhydrite, calcite, dolomite, ankerite, and siderite. Pyrite is also predicted to dissolve, but the wt% of pyrite in the system is very low. The increases in ion concentrations are consistent with the dissolution of dolomite and anhydrite. However, it is calculated that less than 0.5 % of minerals volume in contact with CO_2 predicted by laboratory studies and previous modeling. The changes in porosity during the course of injection and many years after the injection are predicted to be less than ±0.13%.

CONCLUSIONS

A lateral borehole was successfully drilled across the full extent (~1000 ft) of a VC-inferred, fault-bounded, paleokarst doline. Triple combo (GR-neutron/density-resistivity), full-wave sonic, and borehole micro-imager logs were run successfully to TD. Results from the formation evaluation reveal well-rounded pebbles, breccias (e.g., crackle, mosaic, chaotic), fractures, faults, vugs, and unaffected host strata consistent with the pre-spud interpretation inferring paleocavern collapse. VC-imaged lineaments coincide with 5–30-m wide intervals of high GR values (100+ API) and matrix-rich breccias and faults/fractures as revealed on the microresistivity image log. PSDM seismic, VC attributes, and formation evaluation permit an integrative assessment of fault/fracture architecture and karst evolution and provide spatial constraints on the geostatistical models. This project validates the predictive utility of VC via a horizontal test boring and demonstrates the usefulness of this tool for detailed characterization and simulation studies of paleokarst reservoirs. Such applications are especially relevant for other CCS projects in Lower Ordovician strata as these karst-overprinted, saline targets are common across North America

An important revelation resulting from this project is the likely occurrence of evaporite karst. This has important implications for CCS characterization projects of Lower Ordovician strata throughout North America. Repetitive cycles recording strataform soft-sediment deformation and breccias are suggestive of evaporite karst and perhaps less so on subaerial exposure, which would tend to generate rounded clasts, as opposed to breccias. Fluid behavior within reservoirs impacted by evaporite karst processes would have significantly better conformance than those overprinted by deeply penetrative vadose karst processes. It is also important to note that karst morphologies identified using VC attributes at Bemis-Shutts Field

have not been observed at Wellington Field, Kansas. Determination of the drivers for this style of vadose paleokarst has important implications for CCS in Kansas. Constraining the age of exposure and the roll of accommodation is important for understanding and predicting the style of paleokarst and its impact on reservoir architecture.

Key accomplishments for this project include:

- Validated utility of seismic volumetric curvature for predicting fault architecture in paleokarst reservoirs.
- Methodology and results have broader implications as the Lower Ordovician section across the United Sates — which is frequently overprinted by paleokarst — is widespread and directly overlies basement and is therefore an attractive carbon storage target.
- This is a valuable public dataset, as this well is the only published account of a horizontal lateral being successfully drilled below the full extent of a paleokarst doline.

Lesson learned during this project include:

- Lost-in-hole insurance for logging tools can be excessive ($100,000 to $1,500,000) for tool-push operations in horizontal wells in contrast to the actual logging costs.
- Velocity model for sub-Arbuckle interval difficult to define due to lack of penetrations to basement. A vertical seismic profile (VSP) would help overcome uncertainties related to depth migration.
- Surprisingly, no mud losses were recorded while drilling through faults, fractures, and large touching vug pores. Log interpretation indicates that solution-enlarged fractures, faults, and touching vugs are occluded with clays introduced during prolonged sea-level lowstand.
- Simulations indicate that individual fault blocks may serve as multiple discrete containers for carbon storage thereby minimizing risk of associated with leakage. That is, the faults serves as non-to-low permeability "curtains" that restrict laterally movement of injected CO_2.

Data gaps identified during this project include:

- Most of the data gaps are related to risks associated with data-acquisition operations within horizontal wells.
- Whole core would provide a key data set for: 1) validating observations made from image logs; 2) constraining phi-K estimates made using wireline log data, and 3) for fault seal analysis.
- A cored pilot hole to basement would have permitted a complete logging suite to basement, including VSPs. Additional data and interpretations from core would have facilitated construction of a more robust facies and property model thereby benefitting simulation-based studies including forecasting.

BIBLIOGRAPHY

Alemu, B. L., P. Aagaard, I. Munz, and E. Skurtveit, 2011, Caprock interaction with CO_2: a laboratory study of reactivity of shale with supercritical CO_2 and brine: Applied Geochemistry, v. 26, pp. 1975–1989.

Al-Dossary, S., and K. J. Marfurt, 2006, 3D volumetric multispectral estimates of reflector curvature and rotation: Geophysics v. 71, p. 41–51.

Archie, G. E., 1950, Introduction to petrophysics of reservoir rocks: AAPG Bulletin, v. 34, p.943–961.

Bennion, B., and S. Bachu, 2007, Relative permeability characteristics for supercritical CO_2 displacing water in a variety of potential sequestration zones: Society of Petroleum Engineers, SPE-95547-MS.

Bennion, B., and S. Bachu, 2010, Drainage and Imbibition CO_2/Brine Relative Permeability Curves at Reservoir Conditions for High-Permeability Carbonate Rocks: Society of Petroleum Engineers, SPE 134028-MS.

Bergbauer, S., T. Mukerji, and P. Hennings, 2003, Improving curvature analyses of deformed horizons using scale-dependent filtering techniques: AAPG Bulletin, v. 87, p.1255–1272.

Blumentritt, C. H., K. J. Marfurt, and E. C. Sullivan, 2006, Volume-based curvature computations illuminate fracture orientations—Early to mid-Paleozoic, Central Basin Platform, west Texas: Geophysics, v. 71, p. 159–166.

Burnside, N. M., and M. Naylor, 2014, Review and implications of relative permeability of CO_2/brine systems and residual trapping of CO_2; Int. J. Greenh. Gas Control, 23, pp. 1–11

Cansler, J. R., and T. R. Carr, 2001, Paleogeomorphology of the sub-Pennsylvanian unconformity of the Arbuckle Group (Cambrian–Lower Ordovician): Kansas Geological Survey Open-File Report 2001-55, 3 plates: http://www. kgs. ku. edu/PRS/publication." OFR2001-55/(accessed September 18, 2013).

Chopra, S., and K. J. Marfurt, 2005, Seismic attributes—A historical perspective. Geophysics, v 70, p. 3SO–28SO.

Chopra, S., and K. J. Marfurt, 2007, Volumetric curvature attributes add value to 3D seismic data interpretation: The Leading Edge, v. 26, p. 856–867.

Cole, V. B., 1962, Configuration of the Precambrian basement rocks in Kansas: Kansas Geological Survey, Oil and Gas Investigations, Map 26, scale: 1:633,600, 1 sheet.

Cole, V. B., 1975, Subsurface Ordovician–Cambrian rocks in Kansas: Kansas Geological Survey, Subsurface Geology Series 2, 18 p.

Cooper, J. D. and M. Keller, 2001, Palaeokarst in the Ordovician of the southern Great Basin, USA: implications for sea-level history: Sedimentology, v. 48: p. 855–873.

Cooper, R.A. and P. M. Sadler, 2012, The Ordovician Period: in B. D. Webby, F. Paris, M. L. Drose, and I. G. Percival (eds.), The Geologic Time Scale 2012: Elsevier, p. 489−523.

Dix, G. R., G. W. Robinson, and D. C. McGregor, 1998, Paleokarst in the Lower Ordovician Beekmantown Group, Ottawa Embayment: structural control inboard of the Appalachian orogen: Geological Society of America Bulletin, v. 110, p. 1046–1059.

Franseen, E. K., and A. P. Byrnes, 2012, Arbuckle Group platform strata in Kansas: A synthesis, in J. Derby, R. Fritz, S. Longacre, W. Morgan, and C. Sternbach (eds.) The Great American Carbonate Bank: The Geology and Economic Resources of the Cambrian–Ordovician Sauk Megasequence of Laurentia: AAPG Memoir 98, p. 1031–1047.

Fritz, R. D., P. Medlock, M. J. Kuykendall, and J. L. Wilson, 2012, The Geology of the Arbuckle Group in the midcontinent: Sequence stratigraphy, reservoir development, and the potential for hydrocarbon exploration, p. 203−273.

Golonka, J., 2002, Plate-tectonic maps of the Phanerozoic: SEPM Special Publication 72, p. 21−75.

Ham, W. E., and J. L. Wilson, 1967, Paleozoic epeirogeny and orogeny in the central United States: American Journal of Science v. 265, p. 332–407.

Hammes, U., 1997, Electrical Imaging Catalog: Microresistivity Images and Core Photos from Fractured, Karsted and Brecciated Carbonate Rocks. Bureau of Economic Geology, University of Texas at Austin, Circular 97-2, 40 p.

Hardage, B. A., D. L. Carr, D. E. Lancaster, J. L. Simmons Jr, R. Y. Elphick, V. M. Pendleton, and R. A. Johns, 1996, 3-D seismic evidence of the effects of carbonate karst collapse on overlying clastic stratigraphy and reservoir compartmentalization. Geophysics, v. 61, 1336–1350.

Hart, B. S., 2002, Validating seismic attribute studies: beyond statistics: The Leading Edge v. 21, p. 1016–1021.

Herron, D.A., 2000, Pitfalls in seismic interpretation: Depth migration artifacts: The Leading Edge, v. 19, p.1016–1017.

Kerans, C., 1988, Karst-controlled reservoir heterogeneity in Ellenburger Group carbonates of west Texas: AAPG Bulletin, v. 72, p. 1160–1183.

Keroher, R. P., and J. J. Kirby, 1948, Upper Cambrian and Lower Ordovician rocks in Kansas: Kansas Geological Survey, Bulletin 72, 140 p.

Knight, I., N. P. James, and T. E. Lane, 1991, The Ordovician St. George Unconformity, northern Appalachians: the relationship of plate convergence at the St. Lawrence Promontory to the Sauk/Tippecanoe sequence boundary: Geological Society of America Bulletin, v. 103, p. 1200–1225.

Krevor, P., S. M. Benson, 2012, Capillary pressure and heterogeneity for the CO_2/water system in sandstone rocks at reservoir conditions, Advances in Water Resources, v. 38, p. 48–59.

Krevor, P., S. M. Benson, 2015, Accurate determination of characteristic relative permeability curves, Advances in Water Resources, v. 83, p. 376–388

Lomando, A. J., 1993. Casablanca field, Tarragona Basin, offshore Spain: a karsted carbonate reservoir.

Lindsay, R. F., and K. M. Koskelin, 1991, Arbuckle Group depositional parasequences, southern Oklahoma: Oklahoma Geological Survey Bulletin 91, p. 71–84.

Loucks, R. G., 1999, Paleocave carbonate reservoirs: origins, burial-depth modifications, spatial complexity, and reservoir implications: AAPG Bulletin v. 83, p. 1795–1834.

Loucks, R.G. and C. R. Handford, 1996, Origin and recognition of fractures, breccias and sediment fills in paleocave-reservoir networks: West geological Society Bulletin, p. 207–220.

Loucks, R. G., P. K. Mescher, and G. A. McMechan, 2004, Three-dimensional architecture of a coalesced, collapsed-paleocave system in the Lower Ordovician Ellenburger Group, central Texas: AAPG Bulletin, v. 88, p. 545–564.

Lucia, F. J., 1995, Lower Paleozoic cavern development, collapse, and dolomitization, Franklin Mountains, El Paso, Texas, *in* D. A. Budd, A. H. Saller, and P. M. Harris, (eds.), Unconformities and Porosity in Carbonate Strata: AAPG Memoir 63, p. 279–300.

Lucia, 1999, Carbonate Reservoir Characterization: Springer-Verlag, 226 p.

Merriam, D. F., 1963, The geologic history of Kansas: Kansas Geological Survey, Bulletin 162, 317 p.

Merriam, D. F., and W. R. Atkinson, 1956, Simpson filled sinkholes in eastern Kansas: Kansas Geological Survey, Bulletin 119, p. 61–80.

Murray Jr, G. H., 1968, Quantitative Fracture Study--Sanish Pool, Mckenzie County, North Dakota: AAPG Bulletin, v. 5, p.57–65.

Mussman, W. J., and J. F. Read, 1986, Sedimentology and development of a passive-to convergent-margin unconformity: Middle Ordovician Knox unconformity, Virginia Appalachians: Geological Society of America Bulletin, v. 97, p. 282–295.

Nissen, S. E., T. R. Carr, K. J. Marfurt, and E. C. Sullivan, 2009, Using 3-D seismic volumetric curvature attributes to identify fracture trends in a depleted Mississippian carbonate reservoir: Implications for assessing candidates for CO_2 sequestration, *in* M. Grobe, J. C. Pashin, and R. L. Dodge, (eds.), Carbon dioxide sequestration in geological media—State of the science: AAPG Studies in Geology 59, p. 297–319.

Overstreet, R. B., F. E. Oboh-Ikuenobe, and J. M. Gregg, 2003, Sequence stratigraphy and depositional facies of Lower Ordovician cyclic carbonate rocks, southern Missouri, U.S.A.: Journal of Sedimentary Research, v. 73, p. 421–433.

Palaz, I., and K. J. Marfurt, 1997, Carbonate seismology: an overview, *in* I. Palaz and K. J. Marfurts (eds.), Carbonate Seismology: Society of Exploration Geophysicists, Geophysical Development Series, v. 6, 1–8.

Palmer, A. N., 1995, Geochemical models for the origin of macroscopic solution porosity in carbonate rocks, *in* D. A. Budd, A. H. Saller, and P. M. Harris, Unconformities and porosity in carbonate strata: AAPG Memoir 63, p. 77–101.

Roberts, A., 2001. Curvature attributes and their application to 3 D interpreted horizons. First Break, v. 19, p.85–100.

Ross Jr, R. J., 1976, Ordovician sedimentation in the western United States, *in* The Ordovician System: Proceedings of a paleontological association symposium, Birmingham, p. 73–105.

Russel-Houston, J. and K. Gray, 2014, Paleokarst in the Grosmont Formation and reservoir implications, Saleski, Alberta, Canada: Interpretation, v. 2, p.SF29–SF50.

Scheffer, A., 2012, Geochemical and microbiological characterization of the Arbuckle saline aquifer, a potential CO_2 storage reservoir; implications for hydraulic separation and caprock integrity: University of Kansas unpublished thesis.

Sloss, L. L., 1963, Sequences in the cratonic interior of North America: Geological Society of America Bulletin, v. 74, p. 93–114.

Sullivan, E. C., K. J. Marfurt, A. Lacazette, and M. Ammerman, 2006, Application of new seismic attributes to collapse chimneys in the Fort Worth Basin: Geophysics, v. 71, p. B111–B119.

Stewart, S.A. and T. J. Wynn, 2000, Mapping spatial variation in rock properties in relationship to scale-dependent structure using spectral curvature: Geology, v. 28, p.691–694.

Thomas, W. A., 1977, Evolution of Appalachian-Ouachita salients and recesses from reentrants and promontories in the continental margin: American Journal of Science v. 277p. 1233–1278.

Walters, R. F., 1946, Buried pre-Cambrian hills in northeastern Barton County, central Kansas: AAPG Bulletin, v. 30, p. 660–710.

Walters, R. F., 1991, Gorham Oil Field, Russell County, Kansas: Kansas Geological Survey, Bulletin 228, 112 p.

Warusavitharana and Parcell, 2013, Sedimentary features, occurrence, and cyclicity of microbialite facies in the Roubidoux and Jefferson City Formations of Missouri and Kansas: AAPG Bulletin, 2013, v. 97, p. 1849–70.

Watfa, M., and Nurmi, R., 1987, Calculation of saturation, secondary porosity and producibility in complex Middle East carbonate reservoirs, paper CC, in 28th annual logging symposium transactions: Society of Professional Well Log Analysts, 24 p.

Williams, P. W., 1985, Subcutaneous hydrology and the development of doline and cockpit karst: Geomorphology, *v.* 29, 463-482.

Young, L. M., 1970, Early Ordovician sedimentary history of Marathon geosyncline, Trans-Pecos, Texas: AAPG Bulletin v. 54, p. 2303–2316.

Zeller, D. E., 1968, The stratigraphic succession in Kansas: Kansas Geological Survey, Bulletin 189, 81 p.

Zeng, H., R. Loucks, X. Janson, G. Wang, Y. Xia, B. Yuan, and L. Xu, 2011, Three-dimensional seismic geomorphology and analysis of the Ordovician paleokarst drainage system in the central Tabei Uplift, northern Tarim Basin, western China: AAPG Bulletin, v. 95, p. 2061–2083.

ACKNOWLEDGEMENTS

We extend our gratitude to our industry partners Vess Oil Corporation and Murfin Drilling Company.

APPENDIX 1

KIRCHHOFF MIGRATION

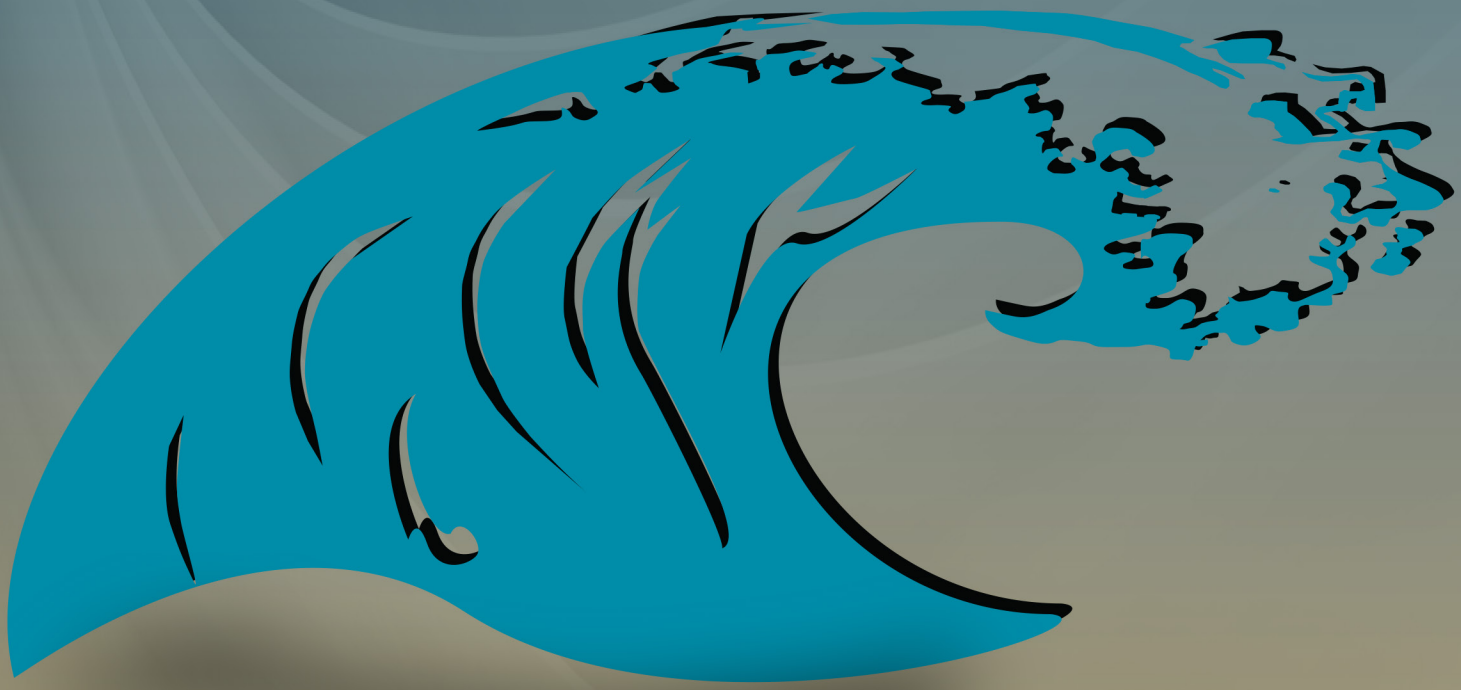

Tsunami Development

TSUNAMI'S UNIQUE APPROACH TO KIRCHHOFF

When acquiring data in rough terrain or with irregular acquisition geometry, the use of the Kirchhoff algorithm is preferred due to its lower sensitivity to non-uniform spatial sampling. The Kirchhoff method does not require a flat datum and therefore offers the advantage of handling variable topography.

Kirchhoff migration works in the offset domain and is based on diffraction summation, which sums the contribution of all data within the migration aperture. The algorithm uses the actual ray path from every source to every receiver. These ray paths are used to construct a diffraction surface and migration is achieved by collapsing each diffraction hyperbola to its origin or apex.

TSUNAMI'S PRE-STACK TIME MIGRATION

Tsunami's Pre-stack Time Migration (PSTM) is a Kirchhoff-based algorithm suited for land, marine, and OBC environments. Straight ray and curved ray travel time options are available. The curved ray option supports both 6th order moveout and Eikonal methods. PSTM offers AVO-compliant amplitude preservation techniques. Tsunami's PSTM supports VTI anistropy through input of an Eta model, HTI through input of Vfast and Vfast azimuth models or a fully orthorhombic migration through input of both HTI and VTI models.

TSUNAMI'S PRE-STACK DEPTH MIGRATION

Tsunami's Pre-stack Depth Migration (PSDM) is a Kirchhoff-based algorithm suited for land, marine, and OBC environments. For imaging beyond 90° it's turning wave capability is useful for imaging salt overhangs or in overthrust geology. PSDM uses advanced amplitude preservation techniques for AVO-compliant output gathers. It supports VTI anisotropy through input of an Eta model and Epsilon/Delta ratio file or Epsilon and Delta models. PSDM performs TTI anisotropy through the input of VTI models and dip and azimuth files.

The travel time computation is performed in the Ray Tracer (RAYS) and the PSDM reads and inputs those travel times.

A **Prepare Data for Input**

B **Build Trace Database**

C **Impulse Tests**

D **Quick Look Target Line(s)**

E **Fully Imaged Target Line(s)**

F **Final Migration**

QC input data and impulse response before expensive full migrations.

INPUT FILE TYPES

As acquisition volumes continue to grow, re-formatting becomes an issue. PSTM and PSDM accepts SEG-Y, GCI, and DSOUT volumes. Tsunami also accepts trace data, little endian, big endian, and IBM float.

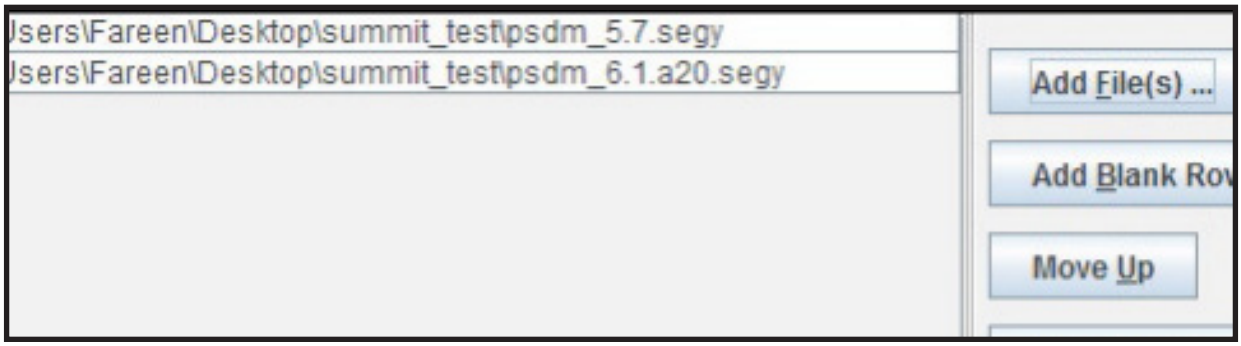

Figure 1: Input File Options

Users can input multiple Seg-Y files using an input file list.

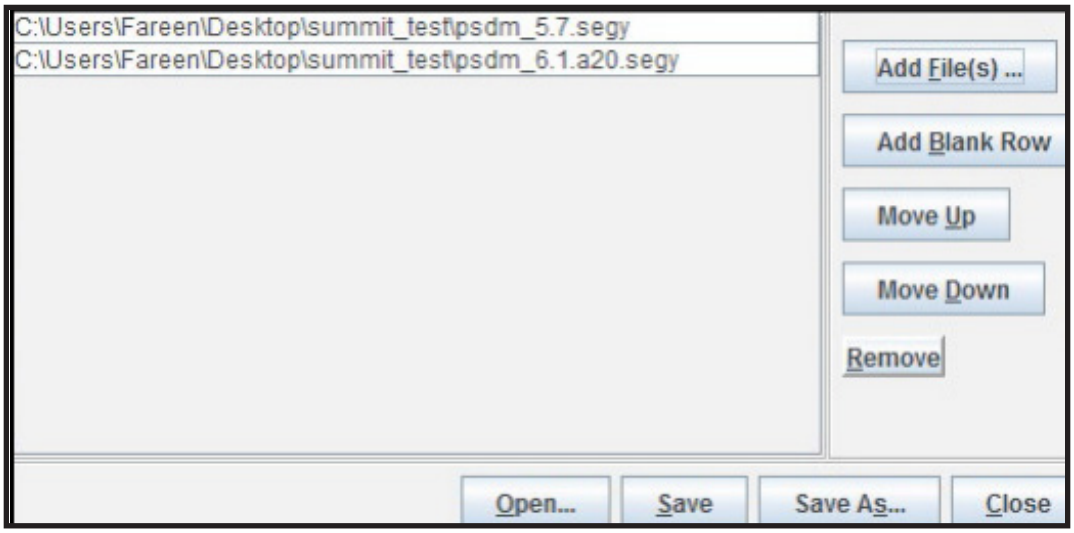

Figure 2: Input File List

Tsunami offers three header displays so users who are unsure of what the acquisiton crew has put in the headers can quickly QC their byte locations.

The only “database” file created by the software is the trace database file, trace.db. This file is an index, or pointer, into the seismic files and provides rapid access to the data stored in the trace headers. Once built, the trace.db can be used in all Tsunami migration modules for the entire time to depth workflow, including PSTM, PSDM, and RTM.

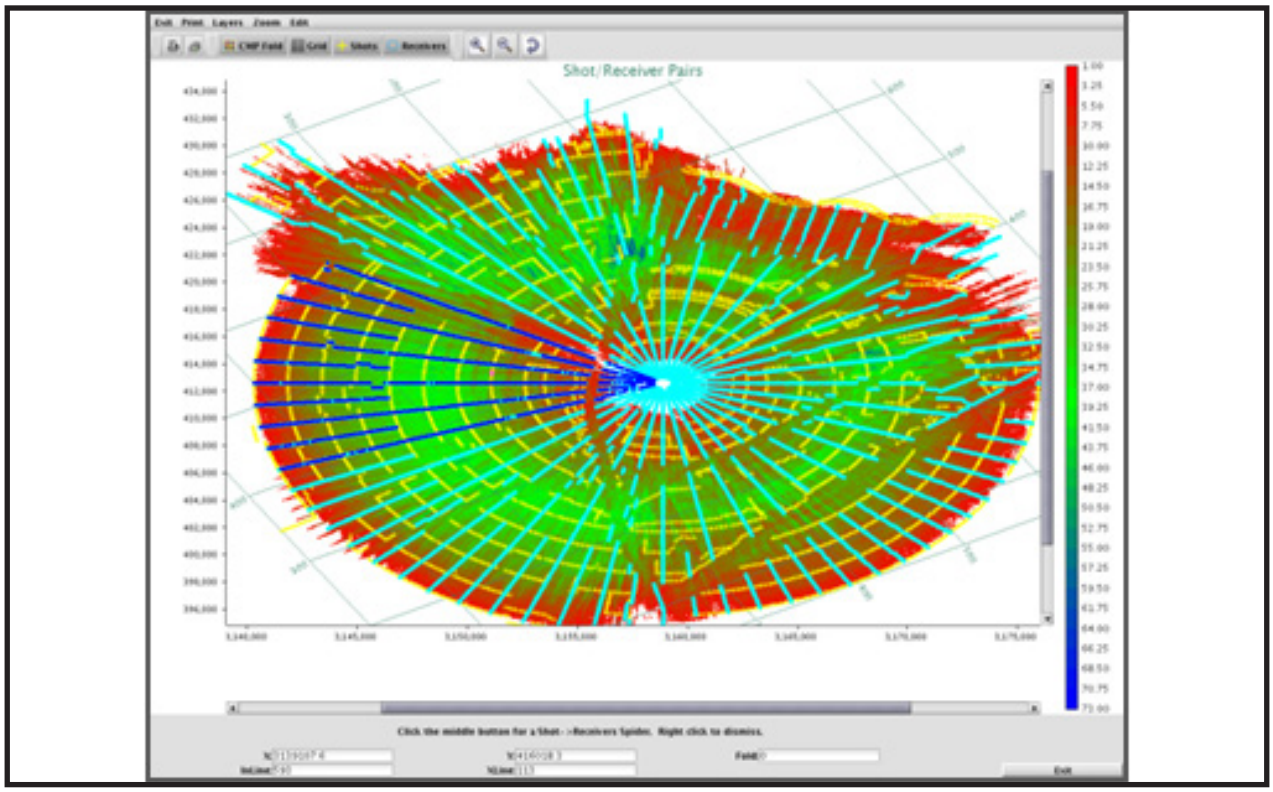

Figure 3: Fold Map with Source Receiver Arrays

The trace.db QC methods provides the user with the ability to answer many questions that may cause potential pitfalls in the migration workflow, including but not limited to:

- Are the inline and xline numbers correct?
- Does the offset calculated from coordinates match the offset header value?
- Do the cdp coordinates match the mid-point of the source and receiver coordinates?
- If using multiple input files, are all input traces included?
- If using merged surveys, are there areas of high folds that must be scaled?
- If imaging from floating datum, Is the static range correct?

All of these questions could be answered from the trace.db build log or the Geometry view options. Any concerns regarding geometry are quickly answered and eliminated.

Click to Enlarge

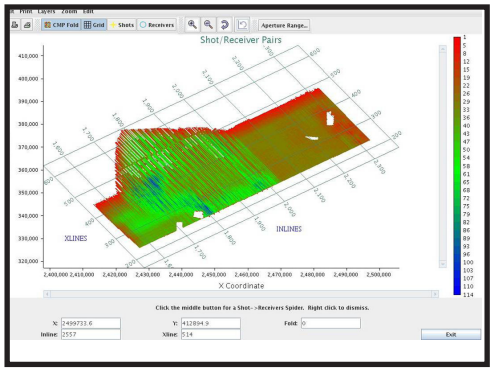

Figure 4: Fold Map in XY Coordinate Display

Click to Enlarge

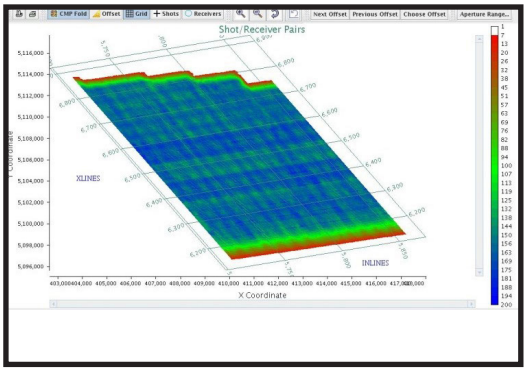

Figure 5: Folp Map in Inline/Xline Map

Click to Enlarge

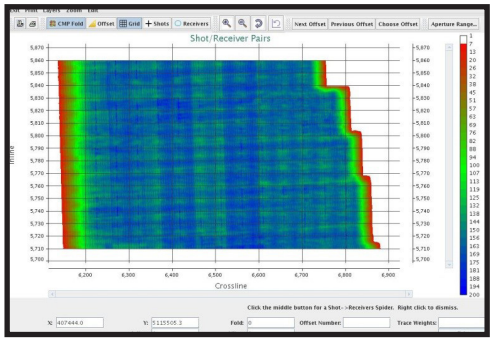

Figure 6: Azimuth Histograms

Click to Enlarge

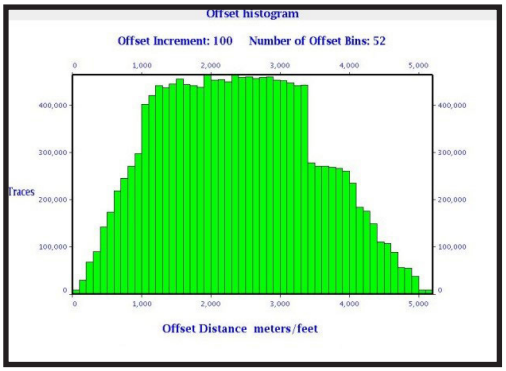

Figure 7: Static Shift Histograms

IMPULSE TEST

Impulse tests confirm, amongst other things, that the geometry and velocity information are correct and properly processed, and allow quick and accurate tests of migration parameters such as aperture and anti-aliasing. In Tsunami migration software, the impulse response is quick and intuitive to parameterize, and jobs running impulse responses are designed to run in a minute on one node.

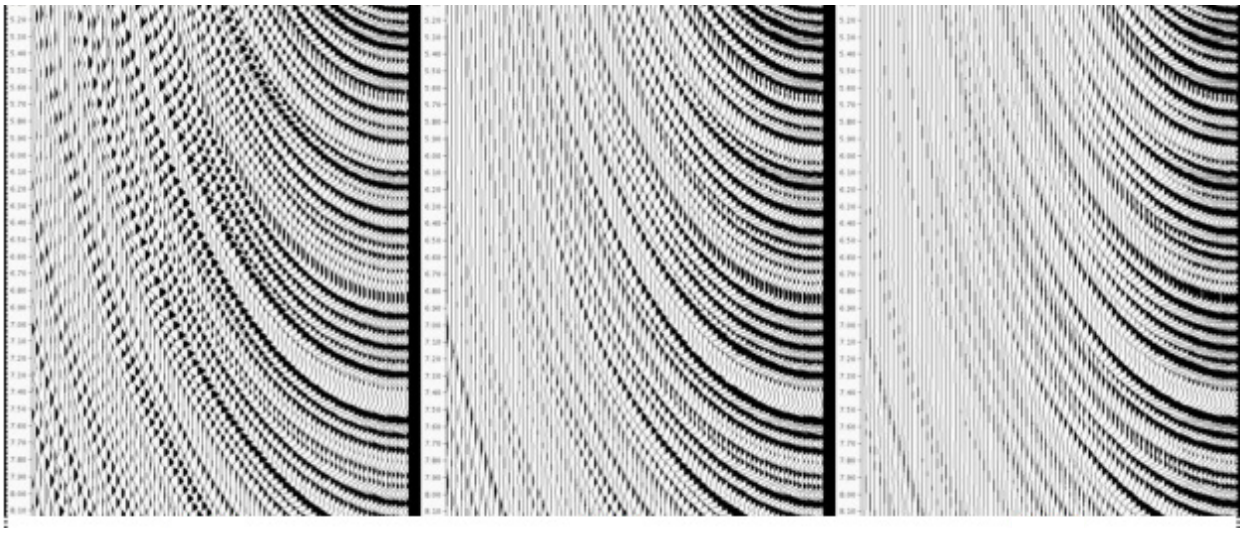

AA 0.2 *AA 0.6* *AA 1.0*

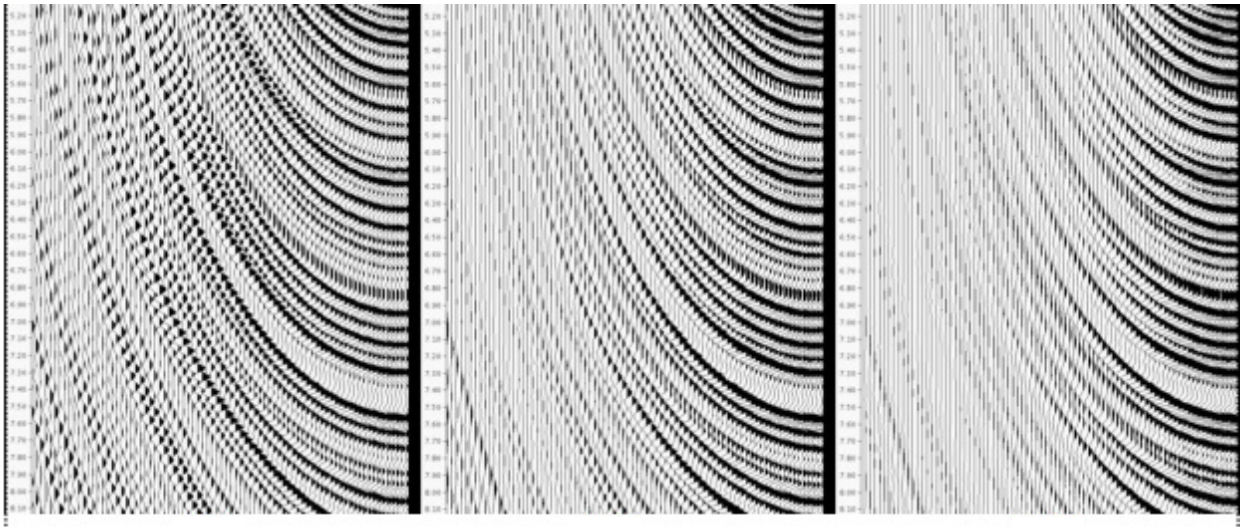

AA 1.0 *AA 1.4* *AA 1.8*

By varying the anti-aliasing p a r a m e t e r s , Tsunami ran 5 different jobs in under 5 minutes. Notice the trade-off between noise and signal from steep dipping events. Never be uncertain with what your final migration will look like with Tsunami PSTM.

Click to Enlarge

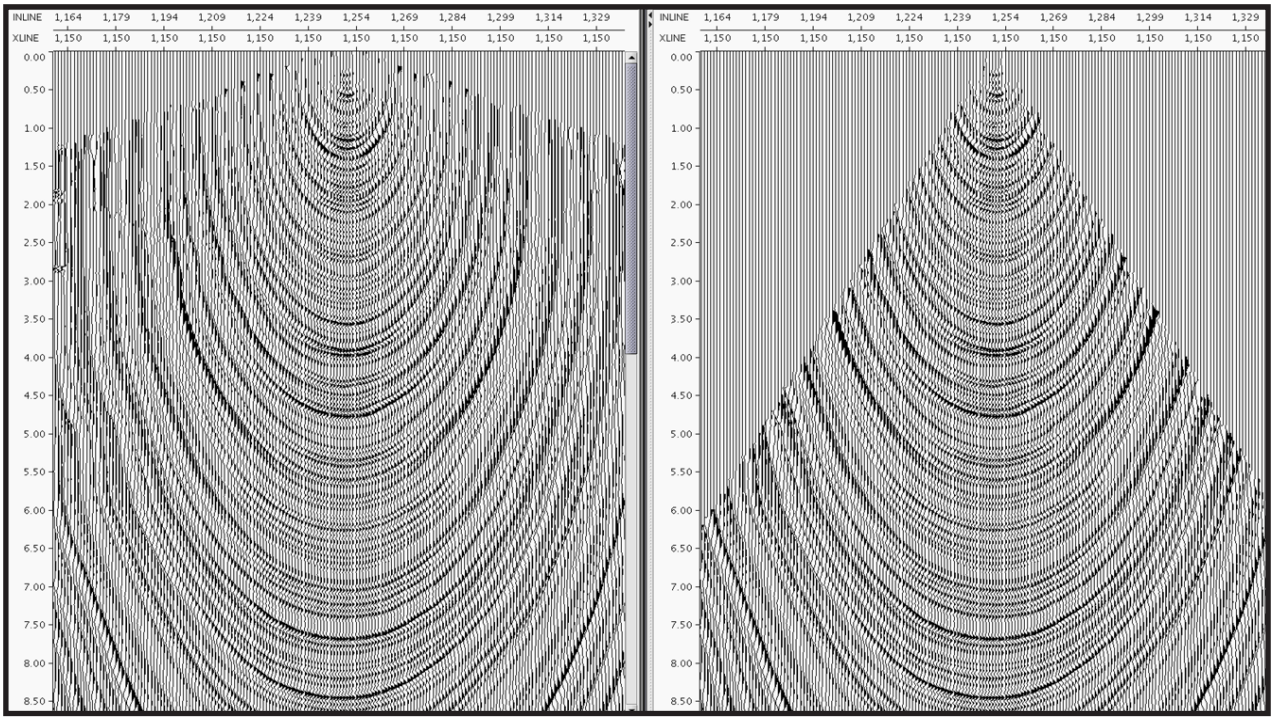

Figure 7: Another impulse response with aperture taper angle applied. Have an intuitive understanding of velocity contrasts with Tsunami PSTM.

FLOATING DATUM

When a survey is acquired over rough terrain or irregular topography it is common to process the data from a smoothed floating datum. At each CDP location the two way travel time between the floating datum and the final datum is stored in the trace database file.

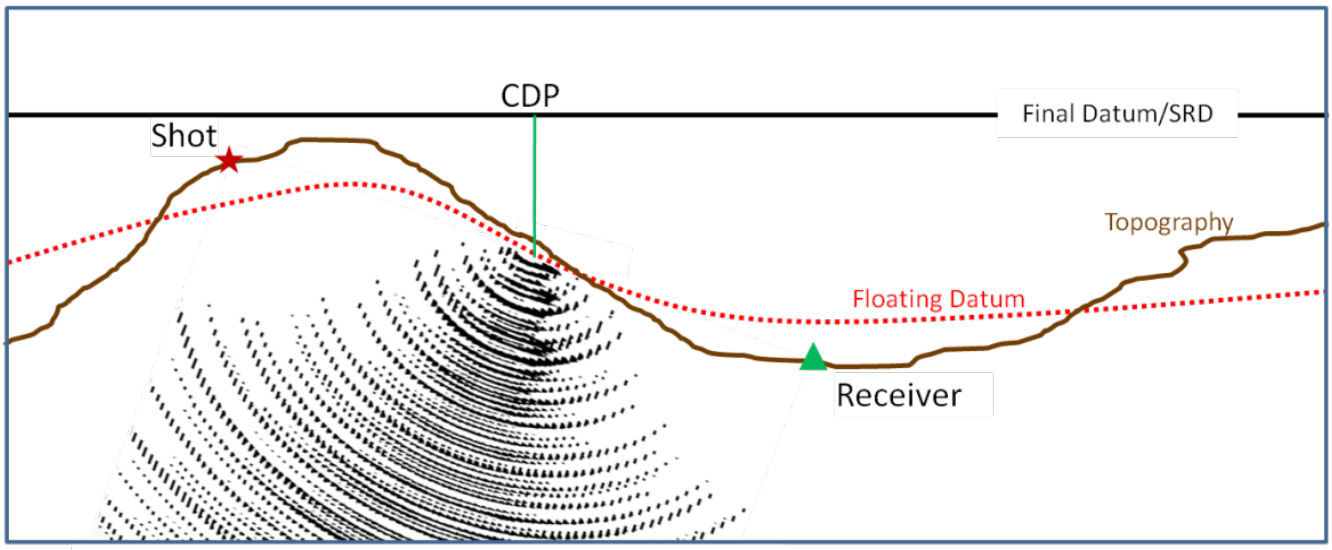

Figure 8: Smoothing Topography to Image with Floating Datuum

Tsunami uses this information to build a map of the floating datum service. When running jobs, this map is used to properly angle the migration operator or orthogonal to the surface, result in improved image quality. Tsunami handles two methods of floating datum:

- ***Two Way Travel Time***
- ***Elevation***

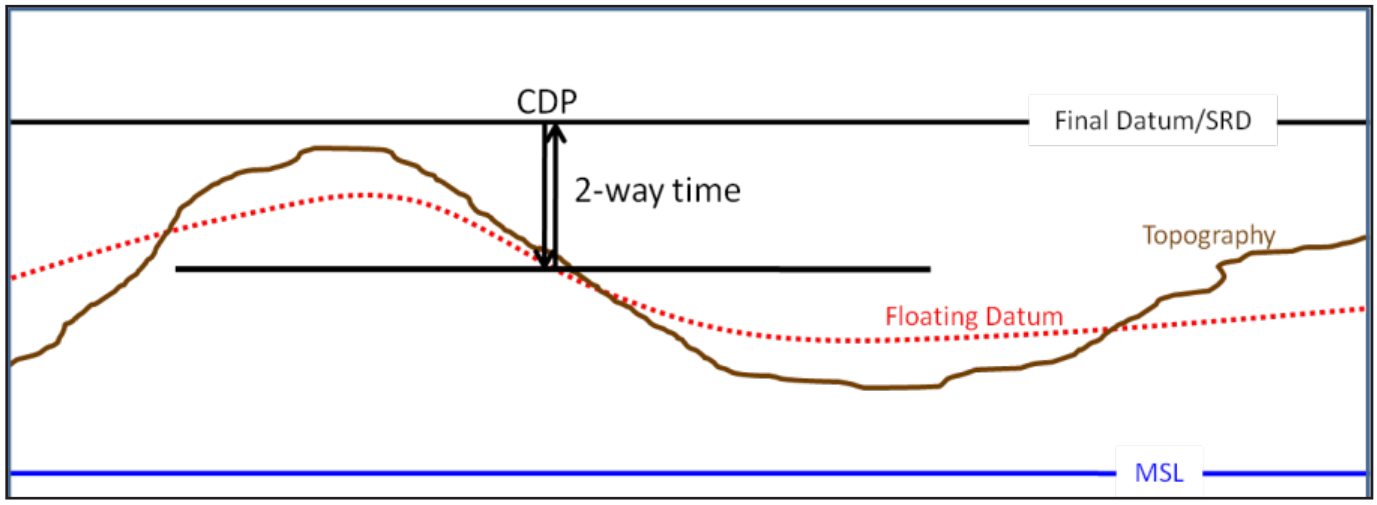

Figure 9: Two Way Travel Time

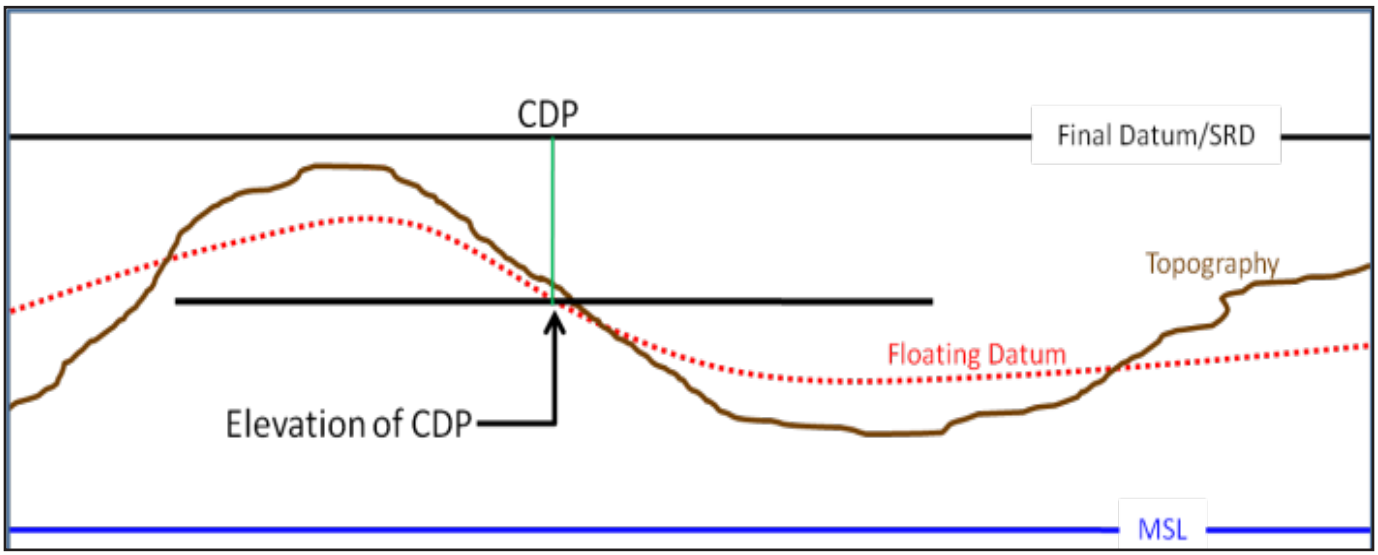

Figure 10: Elevation

RAY TRACER

The Tsunami Ray Tracer module (RAYS) generates travel times for the Tsunami Kirchhoff pre-stack depth migration module (PSDM). Individual rays are advanced using a 4th order Runge-Kutta solver. The program offers three methods of selecting which travel times are used in the event of multiple arrivals; minimum time, minimum distance and maximum energy. The program uses the wavefront reconstruction method to maintain accuracy as the rays move through the velocity model. The user has control over many parameters, and virtually any size velocity model can be used.

RAYS advances the individual rays as members of beams, or triangular sets of three adjacent rays. As the rays propagate through the model the individual ray times are extrapolated to a common point within the beam, and then compared to each other. If the times deviate by more than the allowed amount a new ray and associated beam are created. This ensures accuracy of the wavefront as the rays scatter.

The step size for advancing a given ray is determined automatically based on the local velocity gradient. As the velocity gradient increases the step size decreases. This mitigates the error in the Runge-Kutta equation associated with increasing angle as the velocity changes. All rays within a beam advance radially from the shot location to the next step. They are then evaluated to determine which velocity grids fall within the beam. Travel times are calculated for those grids that fall within each beam. In the event a grid falls within multiple beams its travel time is determined by the defined selection method of minimum time, minimum distance or maximum energy.

All travel time interpolation, both in the RAYS and PSDM modules, is done using slowness rather than seconds. This improves the accuracy of the interpolation, and allows the user to improve performance by selecting a larger increment in the input subsurface shot locations without a sacrifice in quality.

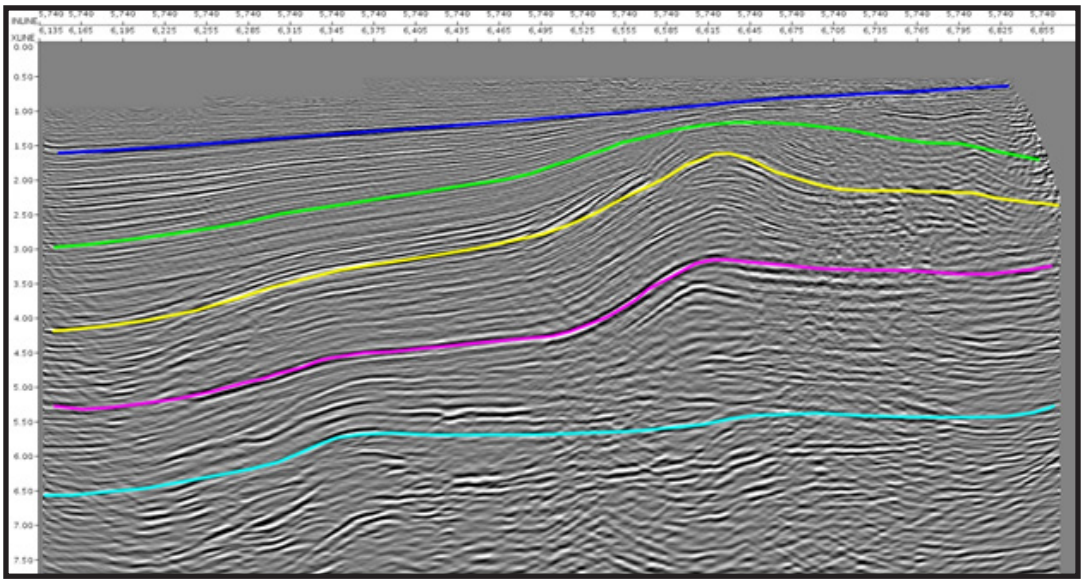

Figure 11: PSTM Section Converted to Depth with Horizons Picked

The RAYS travel time calculations will work with interval models created by other vendor's software. However, Tsunami also provides tools that allow you to quickly and reliably build the required interval model from the RMS velocity model used for time migration. Horizons are picked on the PSTM stack stretched to depth. These horizons are then used to constrain the Dix RMS to interval conversion.

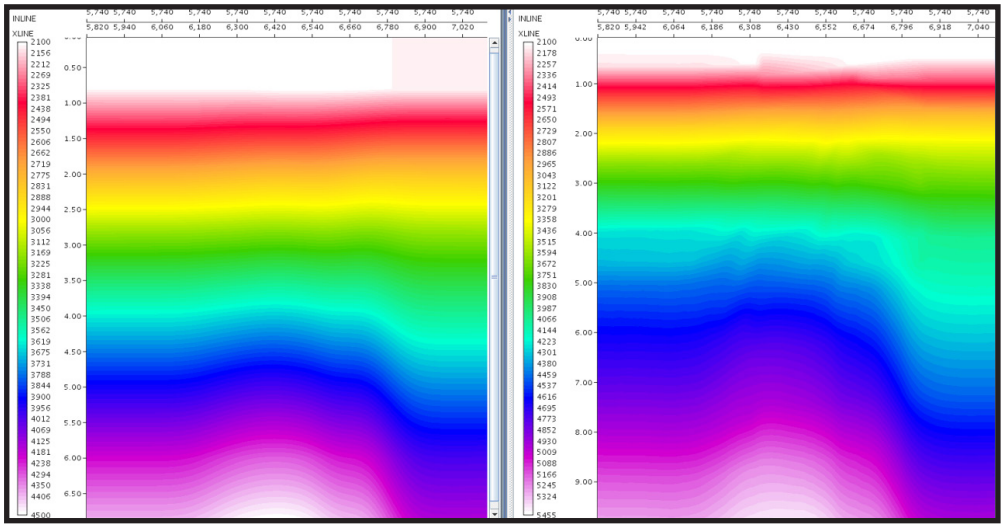

Figure 12: On the Left: RMS Velocity Model On the Right: RMS Velocity Model Converted to Depth Interval Velocities

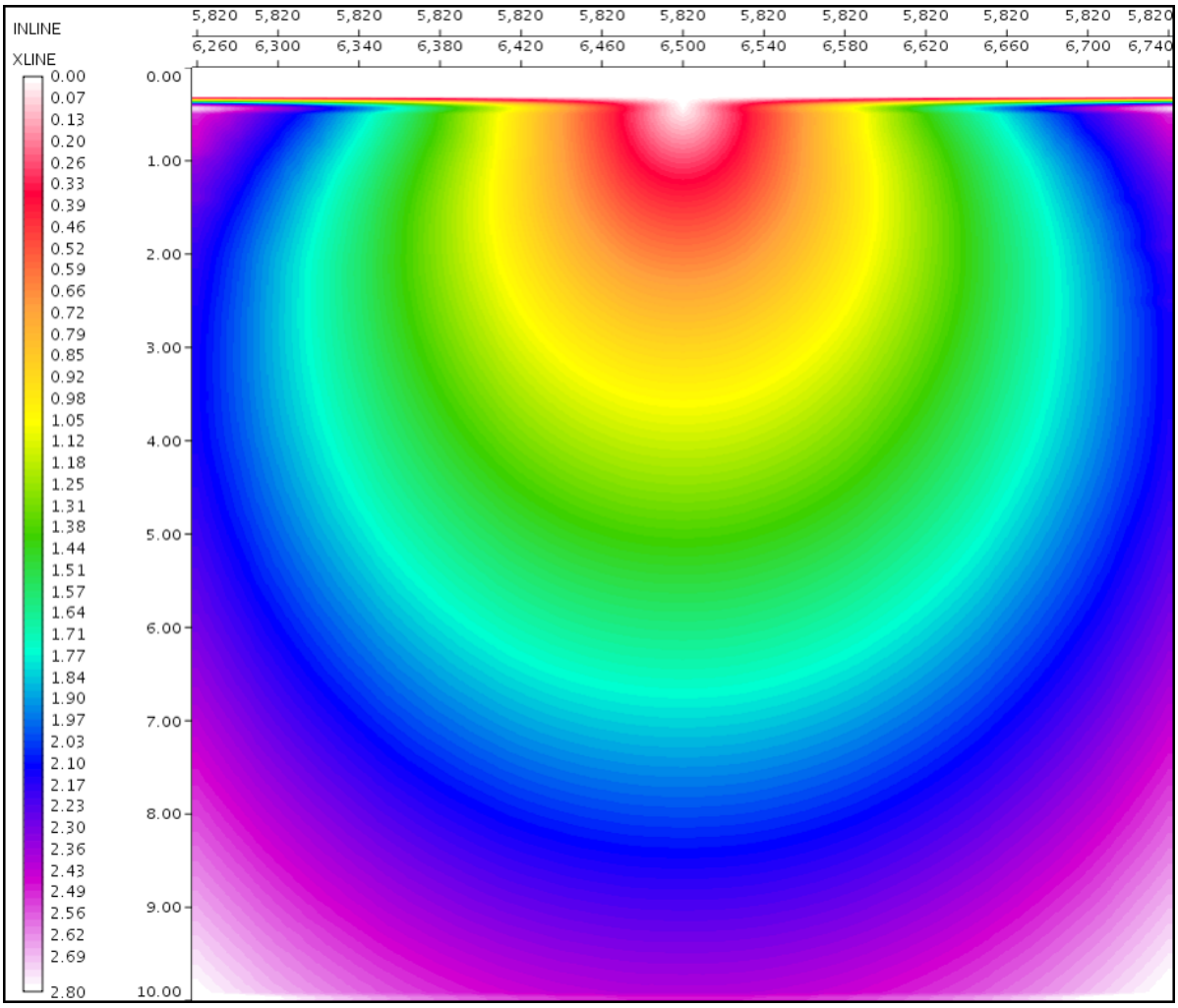

Figure 13: QC Raytracer Travel Times By Outputting a Seg-Y File

Tsunami allows you to QC the Raytracer travel time file before input into depth migration.

Tsunami Contact Information

North America
10111 Richmond Ave.
Suite 230
Houston, Texas 77042
713.532.5006

South America
Carrera 9 No. 71-70
Oficina 303
Bogota, DC
Colombia
+57 313.4599.294

Europe, Africa, Australia, Asia
Franz-Ulrich-Str 18A
34117
Kassel, Germany
+49 (0) 151.547.877.54

www.tsunamidevelopment.com

sales@tsunamidevelopment.com